Underground In-situ Acoustic Emission in Study of Rock Stability and Earthquake Physics

Katrin Plenkers, Gerd Manthei, and Grzegorz Kwiatek

Abstract In-situ acoustic emission (AE) monitoring is carried out in mines, tunnels and underground laboratories in the context of structural health monitoring, in decameter-scale research projects investigating the physics of earthquake nucleation and propagation and in research projects looking into the seismo-hydro-mechanical response of the rock mass in the context of hydraulic stimulations or nuclear waste storage. In addition surface applications e.g. monitoring rock faces of large construction sites, rock fall areas and rock slopes are documented in the literature. In geomechanical investigations in-situ AE monitoring provides information regarding the stability of underground cavities, the state of stress and the integrity of the rock mass. The analysis of AE events recorded in-situ allows to bridge the observational gap between the studies of faulting processes in laboratory and studies of larger natural and induced earthquakes. This chapter provides an overview of various projects involving in-situ AE monitoring underground with a focus on recent achievements in the field. In-situ AE monitoring networks are able to record AE activity from distances up to 200 m, but the monitoring limits depend strongly on the extension of the network, geological and tectonic conditions. Very small seismic events with source sizes on approximately decimeter to millimeter scale are detected. In conclusion in-situ AE monitoring is a useful tool to observe instabilities in rock long before any damage becomes directly visible and is indispensable in high-resolution observations of rock volume deformation in decameter in-situ rock experiments.

Keywords In-situ AE monitoring · Structural health monitoring · Rock stability · Underground in-situ experiments · Hydraulic stimulation · Earthquake physics · Scaling relations

K. Plenkers
ETH Zurich, Zurich, Switzerland

G. Manthei (✉)
THM University of Applied Sciences, Giessen, Germany
e-mail: gerd.manthei@me.thm.de

G. Kwiatek
GFZ German Research Centre for Geosciences, Potsdam, Germany

C. U. Grosse et al. (eds.), *Acoustic Emission Testing*, Springer Tracts in Civil Engineering, https://doi.org/10.1007/978-3-030-67936-1_16

1 Introduction

This chapter will review applications of in-situ acoustic emission (AE) monitoring in mines on the scale of some hundred meters down to several decimeters. In-situ AE monitoring refers to the passive measurement of seismic events with magnitudes ranging $-6 < M_W < -2$ (Fig. 1), which correspond to fracture sizes of centimeter to meter scale. These small seismic events are called, depending on the science community, acoustic emission [1] or nano- and picoseismicity [2]. They represent the formation of novel fractures or the activation of pre-existing fractures in the underground rock volume.

The principal mechanism of earthquakes is believed to be independent of the scale. A small portion of the overall accumulated elastic strain energy is released in form of elastic waves. This imposes that the fundamentals of earthquakes physics developed at larger (or smaller) scales can be implemented in the analysis of AE events. Recent studies [4–7] show that the self-similarity of earthquake source parameters and statistical properties of seismicity hold even for the magnitude range recorded in the in-situ AE monitoring. Figure 2 summarizes recent studies of scaling relations, showing that the frequency-magnitude Gutenberg-Richter distribution displays self-similar behavior between M –3.5 and 7.3. Likewise, the general scale invariance between the fault size and fault slip is visible, regardless of whether the seismicity is of tectonic or anthropogenic origin.

Seismic events of all sizes represent the sudden release of stored elastic strain energy resulting in slip over the rupture area. The mechanism was first described for large tectonic earthquakes at the San Andreas Fault in California [8]: Exact geodetic mapping of movement at the fault‘s surface trace allows to measure the

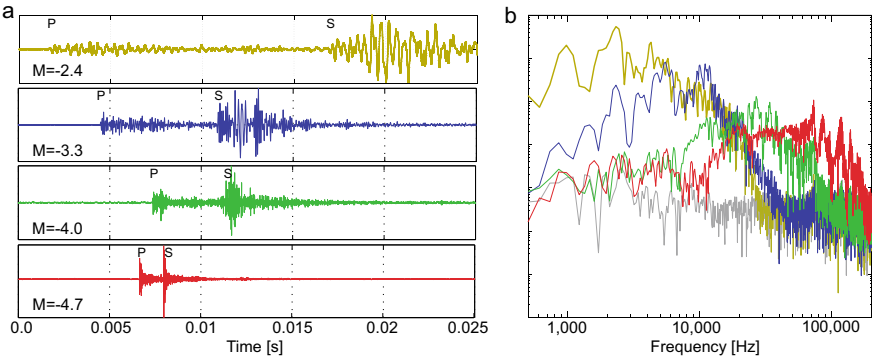

Fig. 1 Waveforms of small seismic events recorded with an in-situ AE monitoring network in an hard rock environment. In **a** raw waveforms as recorded by bottom-view, uni-directional in-situ AE sensors uncorrected for path or instrument effects of four seismic events with different magnitudes are shown. Both P- and S-waves are clearly visible. In **b** the corresponding raw amplitude spectras are shown, displaying the shift of frequency content of the smaller events towards higher frequencies. Figure modified from Plenkers et al. [3]

(a)

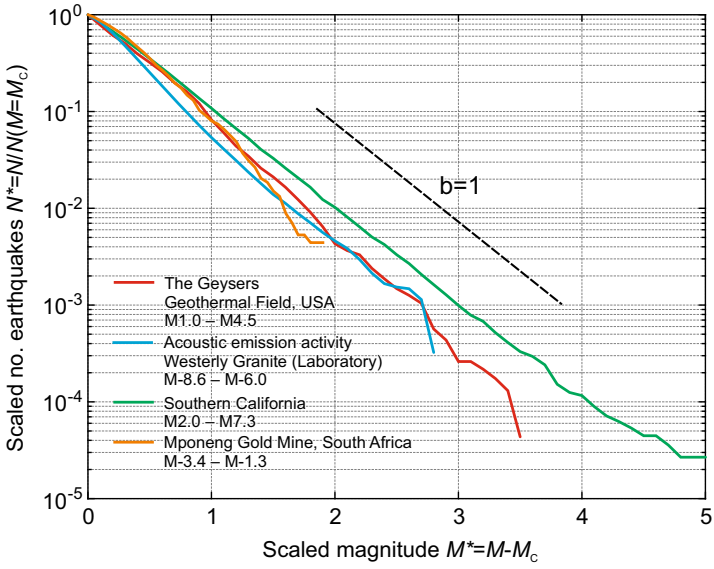
Scaled no. earthquakes $N^*=N/N(M=M_C)$
Scaled magnitude $M^*=M-M_C$
b=1
The Geysers
Geothermal Field, USA
M1.0 – M4.5
Acoustic emission activity
Westerly Granite (Laboratory)
M-8.6 – M-6.0
Southern California
M2.0 – M7.3
Mponeng Gold Mine, South Africa
M-3.4 – M-1.3

(b)

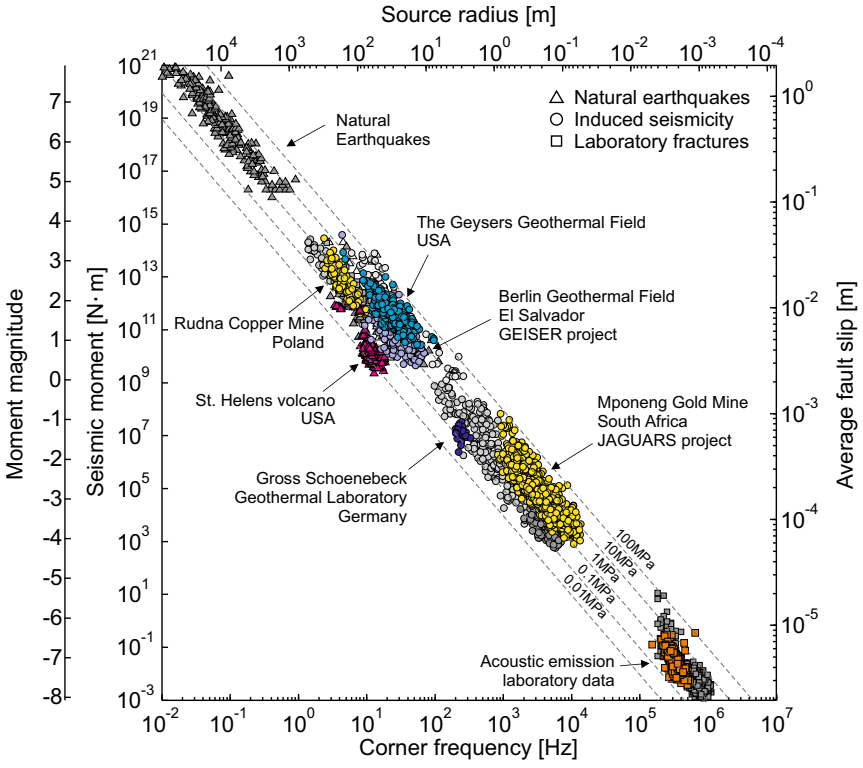
Source radius [m]
Moment magnitude
Seismic moment [N·m]
Average fault slip [m]
Corner frequency [Hz]
Natural earthquakes
Induced seismicity
Laboratory fractures
Natural Earthquakes
The Geysers Geothermal Field
USA
Berlin Geothermal Field
El Salvador
GEISER project
Rudna Copper Mine
Poland
St. Helens volcano
USA
Mponeng Gold Mine
South Africa
JAGUARS project
Gross Schoenebeck
Geothermal Laboratory
Germany
100MPa
10MPa
1MPa
0.1MPa
0.01MPa
Acoustic emission
laboratory data

◀**Fig. 2** **a** Similarity between frequency-magnitude Gutenberg-Richter distributions from various earthquakes datasets spanning from magnitude M –3.4 to M 7.3. For presentation purposes, the datasets are scaled to their corresponding magnitudes of completeness and total number of earthquakes in the dataset above the magnitude of completeness. The datasets show power law distribution indicating the scale invariance. Printed with permission after Bohnhoff et al. [2]. **b** Relation between seismic moment (moment magnitude, average fault slip) and corner frequency (source radius, source size) for various datasets of tectonic and anthropogenic seismicity. Datasets suggest the existence of scale invariance between fault size and fault slip expressed in the visible global trend. The ratio between seismic moment and cube of source radius is proportional to seismically derived static stress drop. Differences between individual datasets reach 5 orders of static stress drop are believed to reflect various physical and non-physical processes (see [13, 14] for extended discussion and intepretation). Reproduced with permission from Bohnhoff et al. [2]

relative movement at the shearing plate boundary and accordingly to estimate the strain build up. Strain builds up until the friction at one point is exceeded. When this occurs, one side of the fault suddenly slips with respect to the other side by a displacement vector up to some metres for very large earthquakes. This is associated with radiation of a small part (no more than a few percent) of the stored elastic energy in a form of elastic waves. The elastic waves are propagating through the medium with the speed of km/s and can be recorded with the use of seismic sensors. However, strain energy is also released in form of slow seismic or aseismic processes. Slow seismic processes include different observational phenomena such as tremors and (very-)long-frequency earthquakes [9–11]. These can be observed with seismic sensors sensitive to low-frequency motions, strainmeters or fiberoptics. Their frequency content is outside of the frequency bands of in-situ AE sensors [12].

Processes outside of the seismic recording band or seismic processes below the arbitraly defined rupture propagation or fault slip velocity are considered aseismic (we note here that the perception of what process is considered seismic may differ between communities). In this chapter we will focus on monitoring of seismic processes of very small seismic events that originate on faults with m-cm size. Following Fig. 2b, earthquakes of size produce low amplitudes and high-frequency ground motions. Figure 3 shows the dependencies between measured corner (dominant) frequency f_o of the seismic signal, the moment magnitude M_W, the seismic moment M_0, and the source radius r_0 for studies in earthquake seismology, microseismicity, in-situ AE monitoring, and AE studies in the laboratory (cf. Fig. 2). Seismic moments and corner frequencies were estimated from the spectral level of ground velocity or displacement spectra corrected for instrument response and wave propagation effects. The estimation of source radii, and the average fault slip are based on the model of Madariaga [15].

According to the relationships used in Fig. 3, Table 1 lists nominal seismic source parameters of natural earthquakes, microseismic events, and in-situ AE events with magnitude M8, M3, and M–4, respectively. Whereas global seismology typically exploits frequencies significantly below 1 Hz, local seismology focuses on the analysis of signals with dominant frequencies of 1–100 Hz.

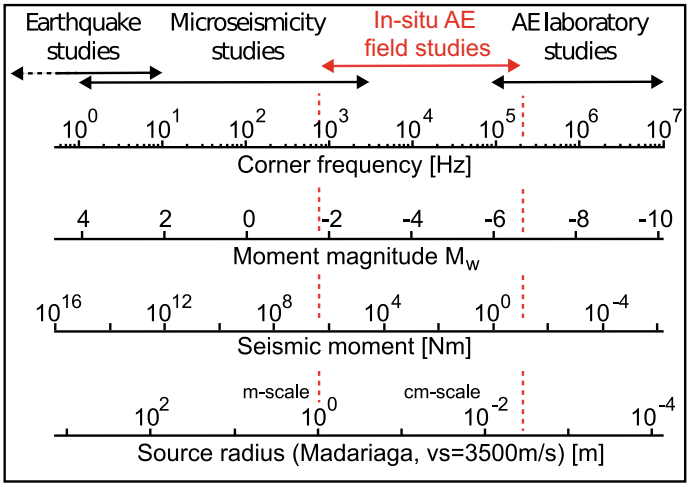

Fig. 3 Relations between measured corner frequency, moment magnitude, seismic moment and the source radius for studies in earthquake seismology, microseismicity, in-situ AE monitoring and AE in laboratory (modified from [16])

Table 1 Comparison of seismic source parameters for natural earthquakes, induced seismicity, and in-situ AE events in rock

Seismic source parameter	Earthquake magnitude M8	Microseismic event magnitude M3	In-situ AE event magnitude M–4
Corner frequency:	10^{-2} Hz	≈2 Hz	$\approx 2 \cdot 10^{4}$ Hz
Seismic energy:	$\approx 6.3 \cdot 10^{16}$ J	$\approx 2 \cdot 10^{9}$ J	$\approx 6.3 \cdot 10^{-2}$ J
Seismic moment:	10^{21} Nm	10^{13} Nm	10^{3} Nm
Source radius:	10^{5} m	400–500 m	≈1 – 10 cm
Average fault slip	1–2 m	$5 \cdot 10^{-2}$ m	$\approx 10^{-4}$ m

Recordings of microseismicity in dense local (e.g., borehole) networks or underground networks are limited to frequencies up to a few kilohertz because of the use of pendulum-based geophones or seismometers. The corner frequency in the field of microseismic measurements ranges between 1 Hz and some hundred Hertz with magnitudes from approximately 4.0 down to −2.0. Above these frequencies, the range of in-situ AE monitoring in rock (marked with red dashed vertical lines in Fig. 3) begins in the frequency range of about 1 kHz up to 200 kHz. For frequencies f > 25 kHz currently only piezoelectric AE sensors are available, which measure seismic waves without a spring-mass system, but are purely based on the piezoelectric effect. Due to strong damping of such high frequency waves, in-situ AE monitoring is most often applied in underground structures like mines or tunnels.

Studying AE in mines is a promising tool to understand the earthquake rupture process in more details because it allows novel research approaches: First, a huge

amount of seismic data is available compared to local seismicity, which allows for effective statistical and seismic source analysis of acquired catalogs. Second, short source-receiver distances allow recording the details of the rupture process in a well resolved scale. And third, the generation process of earthquakes in mines may be semi-controlled, i.e. the seismicity induced by human mining operations allows to set-up seismic network "on the spot" of seismic activity.

Many examples of applications of in-situ AE monitoring in mines as found in the literature are given in Table 2. This table is an updated version of Table 2 from Manthei and Plenkers [17]. It displays the test site of the project, the resulting publications, the type of AE networks with source–receiver distances, mode of recording, and the rock type with the number of recorded events. In Table 2 we consider peer-reviewed articles in English that describe in-situ AE monitoring in the underground in the frequency range 1–200 kHz. Additional studies presented in conference abstracts, proceedings or reports are given in Feng et al. [18]. We consider only studies using piezoelectric AE sensors, not studies using piezoelectric accelerometers or geophones, as those sensors are confined to the low kHz range (<25 kHz) and the limited bandwidth and sensitivity puts significant limitations to the analysis of AE signals. This chapter does not cover AE measurements in the same frequency range conducted at the Earth surface, but we like to point out the measurements were successfully conducted e.g. in the context of slope stability [19, 20], rock mass disturbance in open-pit excavations [21], and rock fall [22]. In the main part of this chapter we summarize the application of in-situ AE monitoring in hard rock, salt rock, during hydraulic fracturing, and in soft rock by discussing selected projects. Besides presenting some large early studies, we concentrate on recent studies that brought novel observations, novel analysis techniques or hardware/software developments to the field of in-situ AE monitoring. Owing to advances in IT technology, in-situ AE monitoring evolved in the last decade from simple event detection and trigger mode recording to continuous waveform recording and full waveform analysis giving the research community the possibility to gain more information on the seismo-mechanical processes in the rock mass.

2 Fundamentals of In-situ AE Monitoring

The International Society for Rock Mechanics has introduced in-situ AE monitoring as a standard method for the detection of fracturing processes as a result of excavations for tunnels and large caverns in the fields of civil, rock slopes, and mining engineering [18]. This chapter gives an overview about the most important aspects of the in-situ AE monitoring, also pointing out recent developments. A more technical description including guidelines for installation can be found in Feng et al. [18].

Table 2 Characteristics and applications of in-situ AE monitoring in mines

Test site/Project	Keyword	Publications, Year	Network/Source-receiver Distance R/Mode of recording	Rock type/No. of AE events
Underground tunnel, Japan	Hydraulic fracturing	Sasaki et al. [23], 1987 Ohtsu [24], 1991	17 AE sensors (up to 100 kHz), 17 accelerometers/R ≈ 1 m/trigger mode with waveforms	Siliceous sandstone 200 AEs during four hydraulic fracturing tests (including microseismic events)
Underground powerhouse, Japan	Progressive excavation	Ishida et al. [25], 2014	24 AE sensors (15–40 kHz)/R ≈ 40 m/trigger mode with waveforms	Porphyritic rock 8 AEs in a few days (fault plane solution)
Brunswick mine, Canada	Tunneling excavation	Butt et al. [26], 2000	2 AE sensors (20–150 kHz)/R ≈ 10 m/trigger mode with waveforms	20,000 recorded AEs in 10 days,
Jinping II hydropower station, China	Tunneling excavation	Cheng et al. [27], 2013	12 AE sensors (1–50 kHz))/R ≈ 8 m/trigger mode with waveforms	4,633 AEs in one month
Underground research laboratory (URL), Canada, TSX Project	Excavation/tunnel sealing	Falls and Young [28], 1998 Young and Collins [29], 1999 Young et al. [30], 2000 Collins and Young [31], 2000 Young and Collins [32], 2001 Collins and Pettitt [33], 2002 Young and Collins [34], 2004 Goodfellow and Young [35], 2014	16 AE sensors (40–400 kHz), 16 accelerometers/R ≈ 10 m/trigger mode with waveforms 15 Olympus V103 AE sensors (30 kHz to 1 MHz)/ R ≈ 0.5 m/trigger mode with waveforms	Granite 15,350 AEs in 5 months Approximately 400 m depth 42 AEs with clear pulse shaped P and S wave phases

(continued)

Table 2 (continued)

Test site/Project	Keyword	Publications, Year	Network/Source-receiver Distance R/Mode of recording	Rock type/No. of AE events
Underground research laboratory (URL) ONKALO, Finland, POSE Project	Spalling experiment/heating	Reyes-Montes et al. [36], 2014	24 AE sensors (≈35–100 kHz)/R ≈ 10 m/trigger mode with waveforms	Pegmatitic granite 609 AEs in approximately 6 months
Äspö Hard Rock Laboratory (HRL), Sweden	Excavation Pillar experiment	Pettitt et al. [37], 2002 Anderson and Martin [38], 2009	24 AE sensors (35–350 kHz)/R ≈ 10 m/trigger mode with waveforms	Dioritic granite 884 AEs in 24 h
	Hydraulic fracturing	Zang et al. [39], 2017 López et al. [40], 2017 Kwiatek et al. [41], 2018, Niemz et al. [42], 2020	11 AE sensors (1–100 kHz) and 4 accelerometers (50 Hz to 25 kHz)/R ≈ 10 m to 30 m/trigger mode with waveforms and continuous recording	Granodiorite/Diorite-gabbro/Granite 196 located AE events during six hydraulic fracturing tests, (more than 4000 AEs during one hydraulic fracturing fracturing test in continuous data) 400 m depth
Underground research laboratory (URL) Mizunami, Japan	Hydraulic fracturing experiment	Ishida et al. [43], 2019	16 AE sensors (70 kHz)/R ≈ 5 m/ continuous recording	Cretaceous Toki granite 2,624 during one hydraulic fracturing test
Salt mine Asse, Germany	Cavity stability/heating	Eisenblätter et al. [44], 1998 Dahm and Manthei, [45], 1998	29 AE sensors (100 kHz)/R ≈ 100 m/trigger mode with waveforms	Salt rock, 250,000 AEs in 11 months
Salt mine Bernburg, Germany	Hydraulic fracturing	Manthei et al. [46], 1998 Dahm et al. [47], 1999 Manthei et al. [48], 2001	8 AE sensors (up to 250 kHz)/R ≈ 10 m/trigger mode with waveforms	Salt rock 1500 AEs during eleven hydraulic fracturing tests

(continued)

Table 2 (continued)

Test site/Project	Keyword	Publications, Year	Network/Source-receiver Distance R/Mode of recording	Rock type/No. of AE events
		Manthei et al. [49], 1998 Manthei et al. [50], 2003	8 AE sensors (up to 250 kHz) and hydraulic fracturing tool/R ≈ 5 m/trigger mode with waveforms	Salt rock 15,000 AEs during four hydraulic fracturing tests
Salt mine Morsleben, Germany (southern part)	Backfilling Cavity stability	Spies et al. [51], 2004 Manthei et al. [52], 2007	24 AE sensors (up to 100 kHz)/R ≈ 100 m/trigger mode	Salt rock 50,000 AEs in one month Approximately 400 m depth
Salt mine Morsleben, Germany (central part)	Backfilling Cavity stability	Spies and Eisenblätter [53], 2001 Manthei et al. [54], 2001 Spies et al. [55], 2005 Manthei et al. [56], 2006 Köhler et al. [57], 2009 Becker et al. [58], 2010 Becker et al. [59], 2014	48 AE sensors (up to 100 kHz)/R ≈ 200 m/trigger mode	Salt rock 100,000 AEs in one month approximately 400 m depth

(continued)

Table 2 (continued)

Test site/Project	Keyword	Publications, Year	Network/Source-receiver Distance R/Mode of recording	Rock type/No. of AE events
Mponeng gold mine, Carletonville, South Africa JAGUARS project	Pillar stress loading	Nakatani et al. [60], 2008 Yabe et al. [61], 2009 Plenkers et al. [3], 2010 Kwiatek et al. [5], 2010 Plenkers et al. [62], 2011 Kwiatek et al. [63], 2011 Naoi et al. [64], 2011 Davidsen et al. [65], 2013 Kwiatek and Ben-Zion [66], 2013 Davidsen et al. [67], 2012 Ziegler et al. [68], 2015 Yabe et al. [69], 2015 Kozlowska et al. [70], 2015	8 AE sensors (1–200 kHz) and 1 triaxial accelerometer/R ≈ 10–200 m/trigger mode with waveforms	Quarzite/Gabbro more than 500,000 AEs in 2 years approximately 3200 m depth
Salt mine Merkers, Germany	Gas and brine loading	Doerner et al. [71], 2012 Manthei et al. [72], 2012 Popp et al. [73], 2015 Plenkers et al. [74], 2018	8 AE sensors (1–100 kHz) and 4 AE sensors (1–150 kHz) and 4 AE sensors (1–80 kHz)/R ≈ 5–30 m/trigger mode with waveforms and continuous recording	Salt rock more than 5,000,000 AEs in 2 years approximately 300 m depth
Mont Terri URL, St Ursanne, Switzerland	Excavation	Le Gonidec et al. [75], 2012	16 AE sensors (unknown) and 4 AE sensors (2–60 kHz)/R ≈ 0.3–6.5 m/trigger mode with waveforms	Opalinus clay more than 20,000 AEs in 2 weeks (2127 located), 300 m depth

(continued)

Table 2 (continued)

Test site/Project	Keyword	Publications, Year	Network/Source-receiver Distance R/Mode of recording	Rock type/No. of AE events
Cooke 4 gold mine, South Africa, SATREPS project	Mining stress	Naoi et al. [6], 2013 Naoi et al. [76], 2015 Naoi et al. [77], 2015 Naoi et al. [78], 2015 Moriya et al. [79], 2015 Yamaguchi et al. [80], 2018	24 AE sensors (1–50 kHz) and 6 triaxial accelerometers (50 Hz to 10 or 25 kHz)/R ≈ 0–180 m/trigger mode with waveforms	Quartzite 365,237 AEs in approximately 3 months 1000 m depth
Salt mine Asse, Germany	Cavity stability	Philipp et al. [81] 2015 Pisconti et al. [82], 2020	16 AE sensors (1–100 kHz)/R ≈ 0–180 m/trigger mode with waveforms	Salt rock more than 100,000 AEs in 10 month, 300 m depth
Grimsel Test Site (GTS), Switzerland	Hydraulic fracturing	Gischig et al. [83], 2018 Jalali et al. [84], 2018 Villiger et al. [85], 2020 Villiger et al. [86], 2021	28 AE sensors (1–100 kHz) and 4 accelerometers (50 Hz to 25 kHz)/R ≈ 9–30 m/trigger mode with waveforms and continuous recording	Granodiorite, 2,000 AEs during three hydraulic fracturing tests, 400 m to 500 m depth

2.1 Sensors

In-situ AE sensors detect seismic signals in the frequency range from 1 to 200 kHz. As for pendulum based seismometers (geophones, accelerometers, strong-motion sensors, long- and short period seismometers), different AE sensors are manufactured that come with differences in the frequency bandwidth, the sensitivity and the involved resonances. Sensors are chosen in in-situ AE monitoring according to the needs of the application e.g. choosing specific frequency bands or weighting sensitivity against the amount of resonances allowed. Very often AE sensors are installed in boreholes from 0.5 to 100 m length. In-situ AE sensors are manufactured according to the different installation techniques: Sensors are existing both for permanent installation e.g. in fully cemented boreholes, and for temporary installations, where the sensor can be retrieved. The latter is common not only for short term measurements e.g. in experiments, but also for long-term (years) monitoring applications, as the sensor can be dismantled for maintenance or replacement. Whereas cemented in-situ AE sensors often have a cylindrical shape (Fig. 4), AE sensors for temporary installation come in a shape that fits the installation surface, because very good coupling of the AE sensor to the rock is crucial. For installation at flat surfaces, e.g. at the flat and polished borehole foot of short boreholes (<2 m), or the tunnel wall, bottom-view AE sensors are used.

For installation at the borehole side wall side-view sensors are existing that allow the installation of several sensors within the same borehole. In the latter case it is important that the sensor shape fits the borehole diameter precisely. Sensors for temporary installation are pressed against the rock using an acoustically decoupled spring system or pneumatic pressure.

In contrast to seismic and micro-seismic sensors, AE sensors do not measure ground movement based on the principle of a spring-mass system, but rather detect stress changes due to the elastic wave passing through the sensor's piezoelectric element. In-situ AE sensors are therefore one component sensors that measure the stress change introduced into the crystal in three dimensions. For this reason, signals with movement opposite to the sensor orientation are detected, but to a smaller amount than signals with moment in normal direction to the sensor. AE sensors

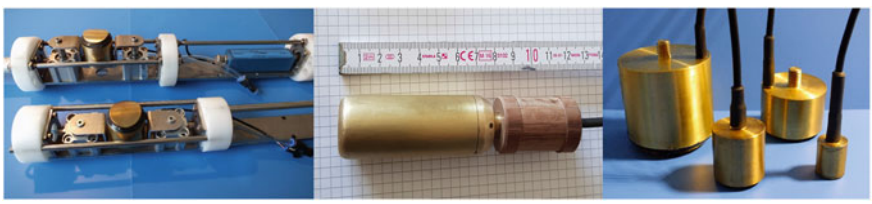

Fig. 4 Various in-situ AE sensors: side-view borehole sensor for temporary installation (left), omni-directional sensor for cemented boreholes (middle), bottom-view sensor for installation at the borehole foot or on rock walls (right). The size of the sensors vary according to the target frequency bandwidth and resonance frequency

are operated with pre-amplifiers. AE sensors are thus piezoelectric-based sensors, which are much more sensitive in the kHz frequency range than spring-mass based accelerometers or pendulum-based geophones/seismometers as shown in Plenkers et al. [3] and Zang et al. [39]. These piezoelectric sensors (not to be confused with piezoelectric accelerometers, which utilize piezoelectric ceramics to measure the movement of the mass), work mostly in resonant mode and in general do not have a flat sensor response. Existence of resonant frequencies improve sensor sensitivity in the targeted frequency range of operation, but at the same time they introduce complexity to the analysis of seismic signals recorded. Observed seismic signals are a convolution of the signal from the earthquake source, path/site effects and instrumental effects. In order to characterize the earthquake source (e.g. by earthquake magnitude), the observed waveforms need to be corrected for path/site and sensor-related effects. While the instrument response of pendulum-based seismometers is prescribed by manufacturers, the absolute calibration of in-situ AE sensors is missing, because the calibration for the in-situ frequency range remains challenging. Neither calibrations using shake tables as typically used for geophones/seismometers can be applied nor testing protocols using test bodys as common for laboratory AE sensors. Instead, manufactures of in-situ AE sensors typically provide information about some aspects of the sensor response e.g. the dominant resonance frequencies or the excitation response, but this alone does not allow to obtain the full information on absolute ground motions. This is an important issue in today's works using in-situ AE data, as more studies require information about absolute ground motion (e.g. to estimate moment magnitude, or other source parameters). Although AE sensors used in the laboratory experiments on rock samples have been successfully calibrated [87], the in-situ calibration of AE sensors remains difficult. Due to the wave length of seismic signals with < 100 kHz it is not possible to test in-situ AE sensors in the laboratory on test blocks. In addition AE sensors are very sensitive to the coupling quality, i.e. any such calibration must be performed directly at the monitoring site.

To address the in-situ calibration problem, two methods are used nowadays: the in-situ sensor characterization by signal deconvolution [6, 63, 84] and simplified calibration by regression analysis [5, 78]. The in-situ sensor calibration by signal deconvolution was first introduced by Plenkers [88]. The approach utilizes the fact that high-frequency accelerometers are fully calibrated. The amplitude response curve of the AE sensor is retrieved by dividing the amplitude spectra of transient seismic signals observed on AE and co-located accelerometer:

$$\begin{aligned} U_{ACC}(f) &= S(f) * R(f) * T_{ACC}(f), \\ U_{AE}(f) &= S(f) * R(f) * T_{AE}(f), \\ T_{AE}(f)/T_{ACC}(f) &= U_{AE}(f)/U_{ACC}(f) \end{aligned} \tag{1}$$

where $S(f)$ and $R(f)$ in Eq. 1 are source and path effects, common to the two co-located sensors, $U_{AE}(f)$ and $U_{ACC}(f)$ are observed non-calibrated and calibrated waveforms and $T_{AE}(f)$ and $T_{ACC}(f)$ are corresponding transfer function (which is known for $T_{ACC}(f)$). This simplified and general scheme may be further improved by relating transfer function shape to incidence angle (see e.g. [62, 63]). The benefit of the signal deconvolution technique is its application to in-situ installation. By incorporating sensor pairs of co-located AE sensors and high-frequency accelerometers to the monitoring network it is possible to take all aspects into account that influence the amplitude response, namely the sensors response, the influence of the installation (rod) system and the coupling effect. The technique is limited to the frequency range up to 25 kHz, the current hardware upper limit of accelerometer recording. Another challenge lies in the recording of picoseismic events in this frequency range on the accelerometer. Due to the significant smaller sensitivity of the accelerometer several projects that aimed for the recording with collocated sensor pair report that the recorded number of passive seismic events was not sufficient for applying the deconvolution method [39, 85]. Instead, active signals e.g. from hammer shots were used.

2.2 Data Acquisition in In-situ AE Monitoring

In-situ AE data acquisition systems combine analog-to-digital converters, power supply, analog filters, and a computer for signal processing. As the AE measurements focus on small seismic events with high dominant frequencies, the sampling frequencies of typical AE acquisition systems used underground range from 500 kHz to 1 MHz. Multi-channel transient recorders (often with 16 or 32 channel) with 16 bit resolution are used. Recently 20 bit systems able to handle this high sampling rates came on the market.

Traditionally, due to (past) data storage and computer processing performance limitations, the the recording is done in triggering mode to efficiently handle large amout of waveform data. This means that only selected limited time windows (e.g., 32 ms) are stored and immediately processed, i.e. when a prescribed amplitude threshold at some number of channels is exceeded (more sophisticated methods are used as well, for example minimum number of P- and S-wave triggers). The recording window length must be chosen according to the expected event-receiver distance as the time window must include all signal modes i.e. P wave, S wave, and Coda wave, as well as sufficient noise windows before and after the signal. The advantage of trigger mode recording is only reduced and useful data is stored, which makes especially long measurement periods more easy to handle. An important disadvantage due to hardware bufffer capacities is the dead time in between registered events that occurs when the system is busy with processing, which prevents the recording of events with very-small inter-event times and results ultimately in data gaps. Recording rates of 10–20 events per second in trigger mode recording are reported [74].

Due to improvements in digital data storage capacities and computer processing performance, it is now possible to store the complete waveform data even from a few weeks or month of AE monitoring. Assuming a 16 channel system and a sampling rate of 1 MHz the daily, uncompressed data output (16-bit integer sample) of such a continuous recording system, sums up to 2.76 TB/day or 83 TB/month. Thus, on-site processing of AE data and associated data reduction is not necessary, as it can be performed at later stages. This allows to apply computationally more extensive continuous-waveform processing methods such as template matching, finger printing methods or AI-based techniques to extract more physically useful information from available recordings [40]. In near future real-time continuous data recording for AE monitoring is expected, for example in the context of in-situ experiments performed in the Bedretto Underground laboratory [89].

In both trigger mode recording and continuous recording real-time processing (P- and S-wave onset picking, localization and relative magnitude estimation) of events is usually implemented. It is important to note that transient noise of anthropogenic or electronic origin is often localized in the automatic processing step and can pollute the seismic catalog, especially in active mines [3, 81].

2.3 Network Geometry and Detection Limits

The AE monitoring covers a limited volume of rock mass, typically framing the cube of length not exceeding a couple of hundreds of meters. In order to allow event localization a minimum of six sensors is installed, but AE networks with up to 128 sensors were successfully realized. The number of sensors depends on the rock volume to be monitored and on the damping. To suppress the influence of the excavation damage zone surrounding the engineering structures such as tunnels or exploitation fronts, AE sensors are installed most often in monitoring boreholes that either remain open or are cemented. One open borehole can host one bottom-view sensor or several side-view sensors. In the design of the network geometry the same rules apply as in seismological theory. The recording is best, if sensors are distributed around the source region in such a way that the spherical coverage is good and signals are recorded from different directions and angles. In cases where this is not possible, e.g. due to restrictions in accessibility, it is possible to install the sensors only on one side of the source region or even within an array. In this cases it is nonetheless important to vary the sensors horizontal and vertical distribution. Typical geometries are shown in Fig. 5.

Due to the high sensitivity of the AE sensors, the in situ AE method allows to monitor fractures down to cm size. Due to the high frequencies, the signals of AE events attenuate more than signals of microseismic events. Observations show that for hard rocks the in-situ AE monitoring is limited to distances from a few tens of meters [85] to a few hundreds of meters [3, 63]. For soft rocks (sedimentary rock, clay-rich rock), the monitoring could be limited to only a few meters [75, 90]. In salt rock, where the rock is very homogeneous and the attenuation of the seismic waves

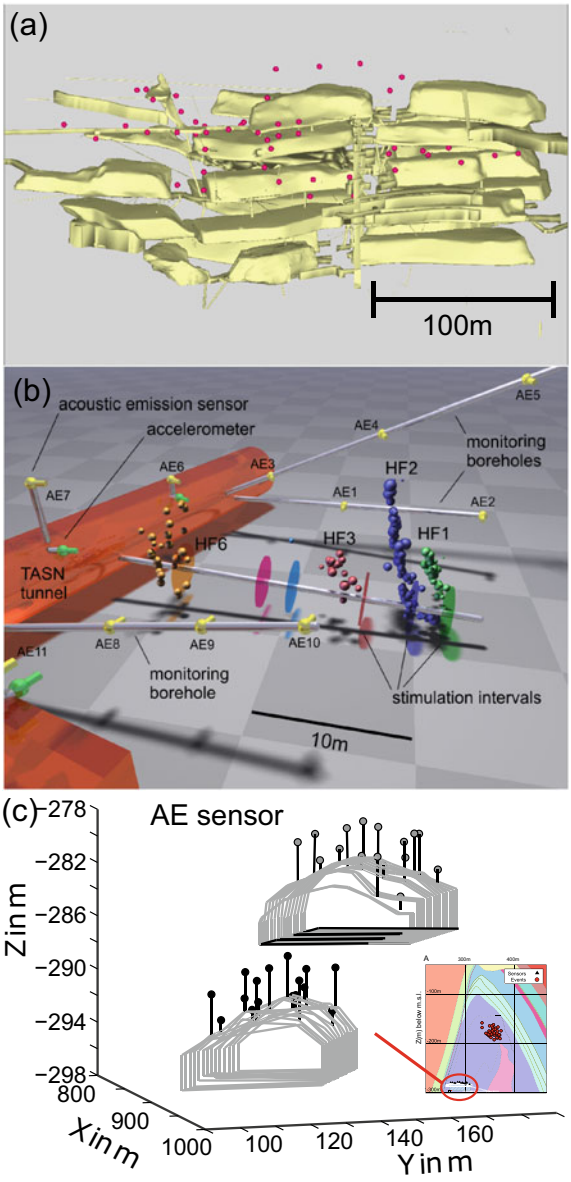

Fig. 5 Different network geometries shown in side-view: mine wide in-situ AE network (**a**, AE sensors shown by red circles, reproduced with permission from REF), site specific borehole network (**b**, AE sensors shown by yellow cones, reproduced with permission from [16, 162]), array network (**c**, AE sensors shown by grey circles, modified with permission from [81]). Mine-wide networks come often in the context of structural health monitoring, whereas site specific networks are typical for in-situ experiments on decameter scale. Limitations in accessible spaces underground lead to the installation of array networks. Shown is an array installed in two neighbouring chambers monitoring the seismic activity in the upper salt dome in approximately 150 m distance

is low, longest source-receiver distances are monitored [81]. The distances that can be achieved are correlated to intrinsic and scattering attenuation of the host rocks, which should be estimated before planning the network geometry.

Consequently, the frequency content of waveforms can vary strongly, reflecting rock attenuating properties. It is shown for the same site that e.g. earthquakes with

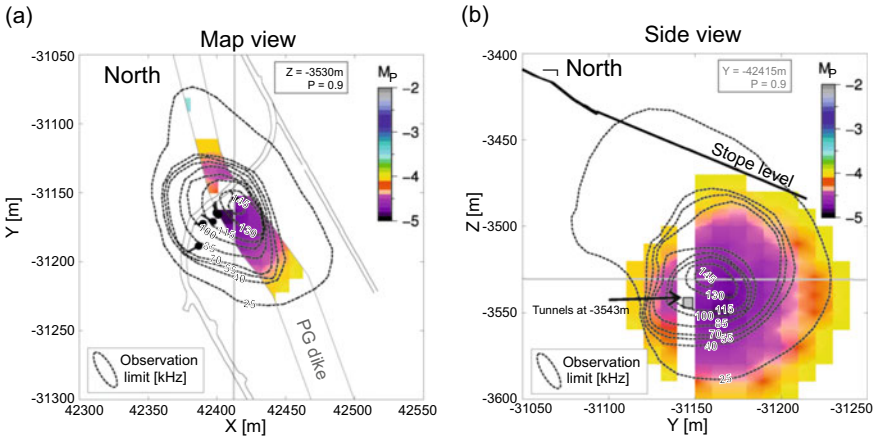

Fig. 6 The sensitivity of a small seismic array in a hard rock environment. Shown is the spatial variation in probabilistic magnitude of completeness as well as in detectability of high frequencies in mapview (**a**) and sideview (**b**). Figure modified after Plenkers et al. [62]

dominant signal frequencies around 145 kHz and moment magnitude down to magnitude −5.0 could be recorded from distances up to 10 m only. At 105 m, events with moment magnitudes down to −4 could be detected with dominant frequencies around 25 kHz [3, 5]. Moreover, engineering structures such as tunnels further reduce the high frequency content of waves due to scattering of waves passing the excavation damage zone. This results in enhanced coda waves and further reduction in detection capabilities as well as inevitable increase in the magnitude of completeness of the seismic catalog. This means in AE monitoring large and spatially-complex variations in magnitude of completeness in the seismic catalog are expected, as shown in Fig. 6. The intrinsic spatial (and sometimes even temporal) heterogeneity in magnitude of completeness must be taken into account carefully [62]. Especially harmful for spatio-temporal or statistical analysis of seismicity is the fact that missing AE activity can be erroneously interpreted as "no AE activity occurring", while in reality the absence of AE events is attributed to strong spatial variations in network sensitivity [5].

2.4 Magnitude and Other Source Parameters

The basic form of a seismic catalog originating from AE monitoring contains information on origin times and hypocenter locations. This can be extended to other seismic source characteristics present in standard seismological catalogs. The cardinal parameter is earthquake magnitude, the measure of earthquake size, which takes the most generic form [91]:

$$M = \log_{10}(A) + C(R) + D, \tag{2}$$

where A is the amplitude of ground motions, $C(R)$ is the function describing correction for source-receiver distance, and D is constant. The of $C(R)$ and D needs to be calibrated beforehand to adjust for the local conditions, presumably including representative attenuation and local site conditions. For example, the IASPEI standard "local magnitude", M_L takes the form:

$$M_L = \log_{10}(A) + 1.11 \cdot \log_{10} R + 0.00189 \cdot R - 2.09, \tag{3}$$

where A is defined in [91] as "*maximum trace amplitude in [nm] that is measured on output from horizontal component instrument that is filtered so that the response of the seismograph/filter system replicates that of a Wood-Anderson standard seismograph but with a static magnification of 1*" under constraint that "*earthquakes (occurs) in regions with attenuation properties similar to those of Southern California*". We brought this lengthy definition to highlight specific requirements (of largely historical nature) to calculate local magnitude in a "valid" way. Of course, many types of magnitudes exist exploiting generic formula presented in Eq. 2. In modern seismology, the amplitude-based magnitudes were superseded by seismic moment which has a universal definition [94, 95]. The seismic moment can be then related to e.g. local magnitude using moment magnitude scale [92].

It is clear that another major problem to calculate magnitude from AE data is the apparent lack of absolute in-situ calibration of AE sensors to the actual ground motions, as indicated in the previous section, which means the true amplitude A as shown in the equation above is unknown. For this reason, magnitudes calculated from AE data are presented as nominal magnitudes [93] or relative magnitudes [83], and therefore they are not tied to any established magnitude scale such as local or moment magnitudes nor do they represent true energy units. These AE-derived magnitudes are useful to gain insights into the relative event size in-between events forming the particular data set. However, it is important to emphasize that these AE magnitudes must not be compared directly to other seismic magnitudes such as local or moment magnitude. Moreover, due to the resonant characteristics of AE sensors and the limited operational band, care must be taken while investigating the statistical properties of seismic catalogs—e.g. the magnitude-frequency relation. Accordingly, it may be difficult to compare AE-derived magnitudes from different datasets, even if the same processing scheme is used. This is because estimation of AE magnitudes for each dataset is subjected to varying local conditions including different attenuation properties of the medium, installation and characteristics of AE sensors (e.g. resonances). The key element in making the relative AE magnitudes comparable in-between different studies is to account for path and transfer function of AE sensors. So far, few studies exist of in-situ AE events, where reliable seismic moments and moment magnitudes were estimated after careful in-situ sensor characterization and correction for the sensor response [6, 63, 84].

Having the AE sensors calibrated in-situ enables calculation of additional source characteristics that allows to describe in details physical processes of nano- and picoseismicity [63] and discuss their scale-invariance. These parameters include static and dynamic characteristics of earthquake [94] such as seismic moment (a measure of the strength of earthquake), radiated energy (a measure of damaging potential of an earthquake), and corner frequency (an approximation of the size of the fault). The derived parameters, such as static stress drop and apparent stress are detailed indicators of physical processes in earthquake source and damaging potential of earthquake.

The static stress drop is a measure of the shear stress release due to an earthquake averaged over the rupture surface area [95] which for the Eshelby type-crack takes the form:

$$\Delta\sigma = \frac{7}{16}\frac{M_0}{r_0^3}, \tag{4}$$

where r_0 is the source radius calculated from seismic data assuming (arbitrarily) the earthquake source model (e.g. [15]). Stress drop is a fundamental seismic source parameter from the perspective of earthquake physics and description of earthquake source scaling properties [14]. Stress drop is also important from the perspective of seismic hazard as it drives near-field ground velocities [96] and is used to characterize the seismic source contribution in ground motions prediction equations.

Self-similar models of earthquakes imply that small and large earthquakes are similar in terms of their rupture physics; and as a consequence, the stress drop should be constant across scales [97]. Many studies indicate that the stress drop is generally independent of the earthquake size (Fig. 2b, see also [14] and references therein) at larger scales, as well as in the laboratory [35, 98, 99] implying linear scaling between co-seismic slip and rupture length. Large variations in static stress drop between 0.1 and 100 MPa were attributed to physical effects including tectonic and stress settings, fluid pressure, variations in rupture velocity, and fault plane normal stress/fault roughness [97, 100–102]. However, they can also originate from modeling assumptions and observation band limitations [103].

The apparent stress is considered a direct measure of damaging potential of earthquakes, as it describes the amount of energy radiated E_0 as seismic waves per unit slip $\bar{u}$ and unit area A of the fault regardless of scale:

$$\sigma_a = \mu\frac{E_0}{M_0} = \frac{E_0}{\bar{u}\,A}, \tag{5}$$

where μ is the shear modulus. Here, typically observed values range from 0.01 to 10 MPa, with varying average values of apparent stress observed for different datasets [2, 104, 105]. Differences in apparent stress may result from variations in partitioning of strain energy that is released during the earthquake rupture process as heat, fracture growth and damage and the energy spent on radiation of elastic waves.

Constant apparent stress values are observed by many authors suggesting similar physical processes govern large and small earthquakes as the same amount of energy is radiated as seismic waves per unit slip and unit area of the fault regardless of scale [104, 106]. However, some authors find evidence that apparent stress increases with seismic moment [107]. This implies that small seismic events radiate a smaller fraction of the total energy as seismic waves than large events. If this is true, in smaller events more energy is spent either in heat or in fracturing of the fault plane.

The scale invariance of earthquakes can be also investigate using statistical features of seismicity. One of the major statistical features of seismicity arguing for self-similarity of earthquakes is evidenced by the empirical Gutenberg-Richter (GR) law. The law states that the frequency-magnitude distribution (FMD) of earthquakes decays as 10^{-bM} where M is earthquake magnitude and $b \cong 1$. Gutenberg-Richter relation forms a power law due to the magnitude being a logarithmic measure of radiated energy or equivalently seismic moment [67], and is a signature of scale invariance. Despite of various physical and non-physical factors influencing the b-value, the relative constancy of FMD exponent indicated that dynamic rupture processes of earthquakes are universal and comparable in broad magnitude range [108] down to at least magnitude –4.4 [4, 5]. It has been also found that GR power law holds in laboratory experiments for AE events recorded during rock friction and fracture experiments [102, 109–111], in AE signals recorded during polyurethane foams [112], and even in cracking of single crystals [113].

2.5 AE Versus MS Monitoring in Mines

While this chapter is focusing on in-situ AE monitoring in mines and Underground Rock Laboratories it must be noted that microseismic (MS) measurements are far more common underground as a tool used for seismic hazard assessment and structural health monitoring. Whereas in-situ AE monitoring is typically focused on limited rock volumes and very small magnitudes, MS monitoring is implemented throughout the whole mine, covering a magnitude range from about M_W approximately –2 to 4 and the frequency range from below 1 Hz to a few kHz. For the recording in these magnitude and frequency range geophones or accelerometers are used. Research on mining-induced seismicity has over a century history. A comprehensive overview is given by Gibowicz and Kijko [94]. More recent works include Milev and Spottiswoode [114], Gibowicz [115], Julia et al. [116], Bischoff et al. [117], Wuestefeld et al. [118], Kuehn et al. [119], Boettcher et al. [7], Kozlowska et al. [70] and references therein.

2.6 In-situ AE Monitoring Versus Laboratory AE Measurements

There are significant differences in boundary conditions between in-situ AE monitoring and monitoring of AE in laboratory experiments on rock samples. The main contrast to laboratory AE measurements are infinite or semi-infinite rock mass bodies which are involved in the in-situ studies, whereas AE measurements in the laboratory occur in a finite body like a specimen. AE waveform data detected during laboratory experiments exhibits the following characteristics: First, higher event rates due to higher sensitivity and thus lower magnitude of completeness is observed. Second, lower signal amplitudes (smaller event magnitudes down to M_W –9 [120] and references therein) corresponding to higher dominant signal frequencies (fractures of sub-millimeter sizes, e.g. [13]). Finally, recorded waveforms displayed enhanced complexity due to limited size of the specimen.

Laboratory measurements provide very good sensor coverage of the focal sphere which is necessary for a precise source location, AE-magnitude estimation and reliable source mechanism assessment. On the scale of laboratory experiments AE sensors are piezoelectric-ceramic crystals directly attached to the free accessible surface of the specimen using e.g. epoxy glue, or embedded in the sample, sensitive to the recording of frequencies $f > 200$ kHz. The number of sensors is typically limited by the available space, which is strongly related to experiment type. The sampling rate of acquisition systems typically do not exceed 10 MHz, but the resonance frequency of AE sensors is higher to improve the sensitivity of AE sensors at higher frequencies. It is therefore common to use AE sensors with resonant frequencies up to 2 MHz, which allows to record full waveforms of fractures on the grain scale of sub-milimiter size. Typically, the lower limit to the operational frequency band does not extend below 100 kHz. A detailed overview about laboratory measurements implementing AE measurements is given in this textbook in Chap. 17.

3 Examples of In-situ AE Monitoring Applications

3.1 In-situ Experiments in Hard Rocks

This section discusses analysis of AE data recorded in three different projects located in hard rocks focusing on their implications for basic earthquake physics, self-similarity of earthquakes and monitoring of slow and violent fracturing processes. Studies of earthquake faulting processes and scaling relations involve the analysis of a variety of statistical and physical parameters of the recorded seismicity. These parameters and their interpretation in the context of physical processes and earthquake scaling will be presented in following sections.

Underground Research Laboratory, Canada. The Underground Research Laboratory (URL) is operated by Atomic Energy of Canada Ltd. located in Manitoba,

Canada. A number of experiments had been conducted since 1990s to investigate design criteria associated with constructions of an underground repository [121] for the nuclear waste storage. The experiments are considered ground-breaking for in-situ AE monitoring. The laboratory is located in the Canadian shield Lac du Bonneth granite batholith at the depth of 420 m.

The Mine-by experiment was designed to advance understanding of the response of rock mass around an underground opening in a high-stress environment and to assess long-term stability of underground openings. A 46-m-long tunnel (3.5 m diameter) excavated parallel to the intermediate principal stress has been excavated progressively in 50 rounds (each round progressed by 1 m) using drilling and mechanical breaking of the rock stub (Fig. 7). A network of accelerometers has been installed surrounding the excavated tunnel, providing good spatial coverage of expected seismicity allowing the recordings of events between 50 Hz and 10 kHz at a sampling rate of 50 kHz [121]. After completion of excavation round 17 at 22 m length of the tunnel, four boreholes of 76 mm diameter were drilled into the tunnel wall surrounding a small rectangular (0.7 m × 0.7 m × 1.1 m) prism of rock [122]. Each borehole was equipped with a string containing 5 Olympus V103 1 MHz AE sensors operating at 10 MHz sampling rate. During excavation of the Mine-by tunnel 25,000 events were recorded and ~3,500 were located (right-hand side of Fig. 8).

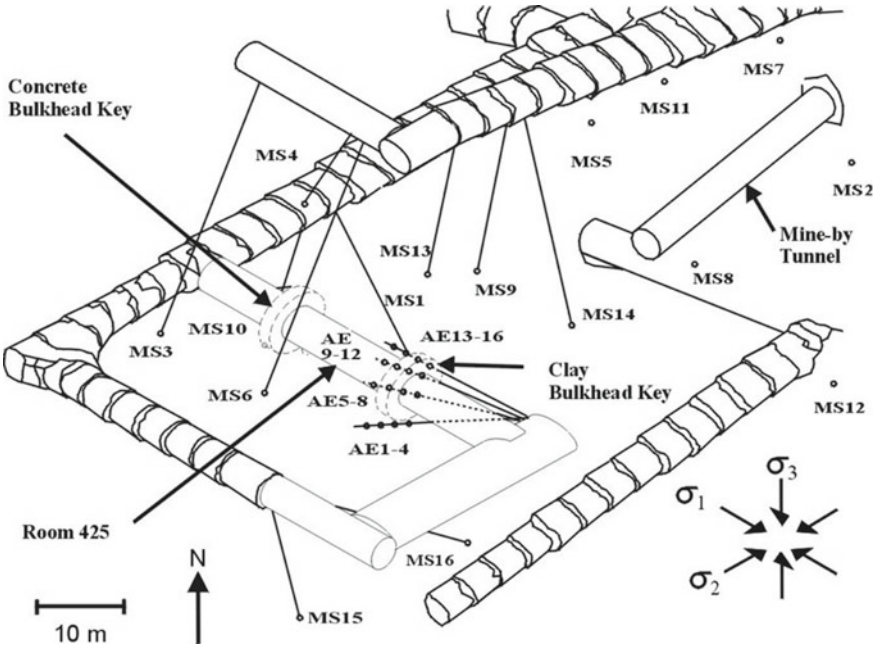

Fig. 7 3D view of the tunnel sealing experiment with mine-by tunnel. The AE sensors and accelerometers are shown with small empty circles, as during the tunnel sealing experiment. Figure from Collins et al. [33]

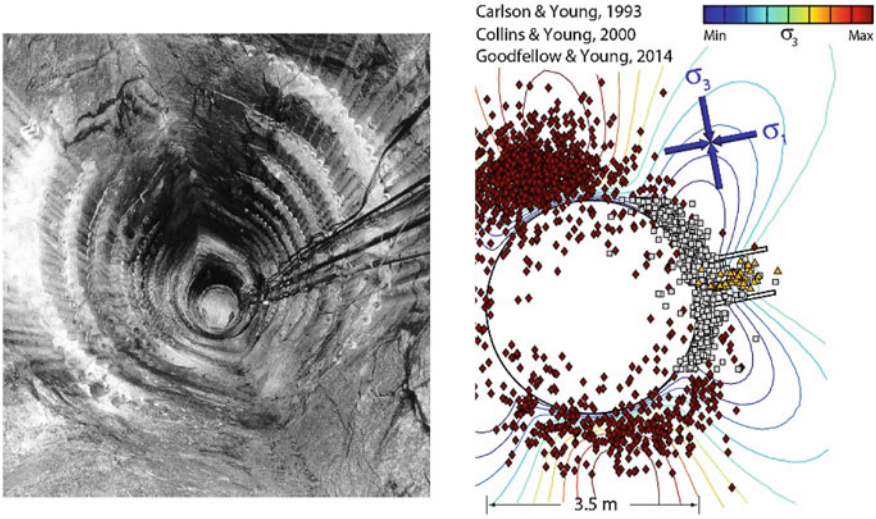

Fig. 8 Photograph of the excavated mine-by tunnel with breakout notches in the roof and floor (left-hand side). AE locations (gray squares and red diamonds) projected on the $\sigma_1 - \sigma_3$ plane recorded during excavation round 17–22 of Mine-by experiment [31, 122], including AE events (orange triangles) located inside the volume surrounded by 4 boreholes where AE sensors were located (right-hand side). The calculated stress field is indicated by blue and green lines (modified after Goodfellow and Young [35])

These occurred mostly in the roof and floor of the tunnel in areas of the maximum tangential stresses [123]. The zones of maximal AE event density corresponded with breakout notches which formed in the roof and in the floor of the tunnel after excavation began and which deepened by spalling during ongoing excavation activities. The notch formed orthogonal to the direction of maximum principal stress (left-hand side of Fig. 8). The spalling planes were parallel to σ_1 and σ_2 and normal to the direction of the smallest principal stress σ_3. Seismic moment tensor solutions calculated for the 37 strong events that were recorded with accelerometers, were located at the roof indicated significant non-shear components [124].

Passive AE data were recorded for more than 3 weeks during following 3 excavation rounds 18–20. Over 1,300 AE events were located, all concentrated near the sidewall free surface in a small volume of rock [122] with low location uncertainty not exceeding 6 cm. Focal mechanisms could be determined for over 100 events with 4 AE events displaying compaction, whereas 75% and 25% of remaining events presented shear and tensile motions, respectively. Goodfellow and Young [35] provided enhanced analysis of AE data recorded near the side wall of the tunnel by calibrating AE sensors to actual ground motions following procedure originally presented in McLaskey and Glaser [87]. Source characteristics of 42 AE events could be then calculated using the classical spectral fitting method. Goodfellow and Young [35] found events with $-7.5 < M_W < -6.8$ and corner frequencies ranging 250–490 kHz. The authors observed relatively low static stress drop values ranging

from 0.01 to 0.1 MPa, lower than that typically observed for natural and induced seismicity [2, 63] (see also Fig. 2b for comparison). This could be explained by low ambient stress conditions in comparison to other studies, i.e. the reduced normal stress imposed on the fault surfaces [101].

In June 1997 the Tunnel Sealing eXperiment (TSX) was conducted in the vicinity of the previous Mine-by project (Fig. 7). TSX aimed to demonstrate full scale tunnel sealing technologies and engineer barriers that will prevent any fluid flow from passing through the excavation damage zone [33], a topic very important in nuclear waste storage. Two bulkhead seals had been keyed into the rock mass in the 13.5 m tunnel, and the interval between seals was pressurized to 4 MPa. The seismicity was monitored by two 16-channels acquisition systems: the first one accommodating triaxial accelerometers and the second composed of AE sensors operating in 0.5–10 kHz and 40–400 kHz frequency ranges, respectively [29].

Hypocenters were determined using a velocity model derived from hammer calibration shots, leading to hypocenter accuracy of 60 cm and 5 cm for events recorded with microseismic and AE network, respectively. Focal mechanisms were determined using seismic moment tensor inversion in time domain. It was identified that AE sensors require additional corrections for coupling quality and incidence angle with the help of active ultrasonic transmission measurements [125, 126]. Source parameters were calculated from both AE and MS events using P and S waves following Urbancic et al. [127]. Fracturing processes were observed both on MS and AE scale, with 12,000 microseismic events and 21,900 AE events recorded [29]. Collins et al. [33] found single or doublets of microseismic events to be spatially associated with clusters of AE activity containing 19–86 AE events. The sequences of AE events were all found to delineate failure regions of corresponding (larger) microseismic event(s) located in the same area. The temporal behavior of AE activity preceding occurrence of larger event(s) varied in different clusters. Considerable foreshock sequences were recorded preceding the larger seismic event(s) in some clusters with accelerating seismic moment release observed up to the time of the larger event, allowing to forecast reasonably well its occurrence using the time-to-failure model [128]. In other clusters, very few foreshocks were recorded possibly indicating a more homogeneous failure plane in terms of strength and stress distribution [129]. Regardless of foreshock behaviours, a significant number of aftershocks has been recorded, a signature of stress relaxation after the mainshock. Interestingly, Collins et al. [33] found aftershocks moving in the same direction as the slip direction of the associated large event. This suggest it may be possible to predict the region of aftershocks from the mechanism of the larger earthquake. Remarkable similarities in the AE focal mechanisms were observed within identified clusters, but the location precision did not allow to interpret the details of fracturing processes.

Experiments performed in URL confirmed that high-frequency close-by AE monitoring is a valuable tool providing detailed picture of fracturing processes down to cm-scale that was previously not possible by using the classical MS monitoring. The observed physical characteristics of individual AE events, as evidenced from their source parameters, were comparable to that observed at large scales for natural and induced earthquakes. At the same time, the AE monitoring clearly highlighted to

existence of complexity and heterogeneity of seismic response even at this small scale [130].

Mponeng Deep Gold Mine, South Africa. The Japanese-German Underground Acoustic Emission Research in South Africa (JAGUARS) project investigated nano- and picoseismic activity (with frequencies ranging from 50 Hz to 200 kHz, moment magnitudes M_W –6 to M_W 0 and source sizes down to a couple of centimeters) at seismogenic depths. The project aimed to study in details the physics of earthquakes from earthquake nucleation, to propagation, and finally post-seismic stress release.

The JAGUARS in-situ monitoring network was installed in 2007 at the depth of 3,540 m below pithead in Mponeng Deep Gold Mine, Republic of South Africa (Fig. 9), an active gold mine run by Anglo Gold Ashanti. The network was located along the transportation access tunnel system, 90 m below the exploitation level, where intensive mining was performed from the Witwatersrand formation. The gold-carrying sedimentary layer (Ventersdorp Contact Reef, VCF) is embedded in a thick series of quartzite, dipping with 26.5° toward the southeast, and reaches a thickness of 0.5–1 m. The network was located also in a direct proximity of the dioritic Pink Green Dyke (PGD), which is a major local geologic feature with 30 m thickness that is embedded in the quartzite rocks. The PGD dips nearly vertically, cutting through the VCF and transportation level, serving at the same time as a support pillar for the

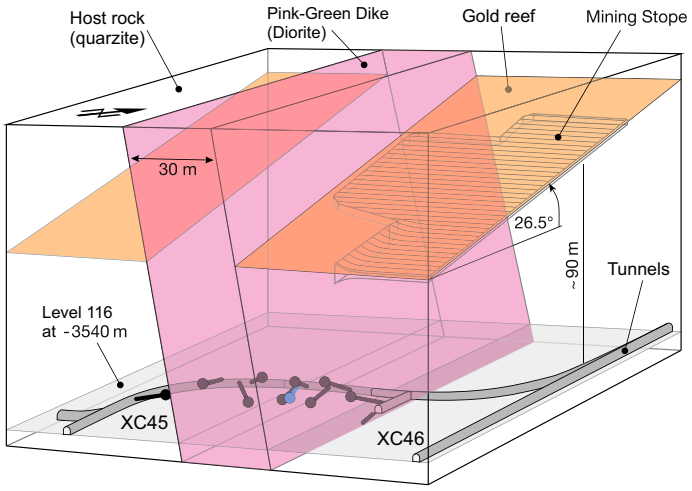

Fig. 9 The schematic view of JAGUARS network in Mponeng Gold Mine and its surrounding geologic/tectonic/anthropogenic features. The network is located at 3540 m depth below pithead. The AE sensors (black circles) and 3-component accelerometer (blue circle) were located in boreholes of variable lengths drilled from access tunnel 116L XC45. The Pink-Green Dyke is shown as a steeply inclined semi-transparent pink block crossing access tunnel and the Ventersdorp Contact Reef (dark yellow, semi-transparent layer) located 90 m above the AE network. The mining stope of approx. 1 m thickness was exploited during the course of the project approaching the Pink-Green Dyke. Figure modified from Plenkers [62]

exploitation (Fig. 9). The core of JAGUARS network consisted of 8 AE sensors manufactured by the Gesellschaft fur Materialprufung und Geophysik mbH (GMuG) from Germany. These sensors were installed in short boreholes of 6–15 m length using a specially developed spring-push system to couple the AE sensor either to the bottom of the hole polished with the diamond drill bit, or coupled to the borehole wall. It was found the AE sensors could record seismic frequencies up to 130 kHz from close-by events [3]. The AE network was completed with high-frequency accelerometers installed in the surrounding area, and one triaxial accelerometer grouted in the direct proximity of one AE sensor (Fig. 9). The data were recorded in triggering mode at sampling rate of 500 kHz. The total combined recording frequency ranged between 50 Hz and 200 kHz. The AE network was capable to detect seismic events with source sizes from a few meters down to centimeters, with the smallest confirmed moment magnitude M_W–4.1 estimated from AE events calibrated with the help of accelerometer recordings [63]. In fact, much smaller events have been observed at short source-receiver distances with dominant frequencies reaching 130 kHz [3, 62] and local magnitudes down to at least M_L –5.5 [5], but the moment magnitudes of these small events could not be estimated due to the limitations in the sensor calibration for higher frequencies. The largest seismic events could be analyzed with the help of the single 3-component accelerometer installed close by AE sensors, as well as the industrial microseismic monitoring network composed of short period geophones spanning the whole mine. Between June 2007 and June 2008 the acquisition system was active for 2002 h (22% of the total time) and recorded 432,904 events [3] in the small area of approx. 300 m $\times$ 300 m $\times$ 300 m covered by the JAGUARS network. Within a two year time period more than two million events were recorded.

In preparation for passive seismic monitoring, Naoi et al. [131] estimated seismic velocities of the two major rock types in the vicinity of the JAGUARS network using ultrasonic transmission measurements performed in the borehole located less than 20 m from AE sensors (cf. Fig. 9). For the quartzite host rock, estimated seismic velocities was $V_P = 6.2$ km/s for P waves and $V_S = 3.8$ km/s for S waves. The velocities within the PGD were found to be slightly higher, with $V_P = 6.9$ km/s and $V_S = 3.9$ km/s. The obtained values were later confirmed by Stanchits et al. [132] in a series of active ultrasonic transmission measurements performed in the laboratory on rock samples performed at a constant hydrostatic pressure of 75 MPa, reproducing the expected stress state at 3.5 km depth.

Mining in the vicinity of the network (see yellow area in Fig. 9) started in early 2007 and proceeded in the direction of PGD. This was associated with an increase in seismic activity around the exploitation level (Fig. 10a). The network sensitivity focused on the dyke-host rock contact close to the mining front, where larger events with magnitudes up to M_W 3.0 were expected due to (a) stress concentration induced by progression of mining at the exploitation level, and (b) generally stronger geomechanical properties of the PGD with respect to the surrounding host rocks [132]. In addition to seismic events the recorded AE activity was identified to be composed of low-frequency drilling signals and other working noises such as shoveling of rocks through boxholes to the transportation level 116L [3].

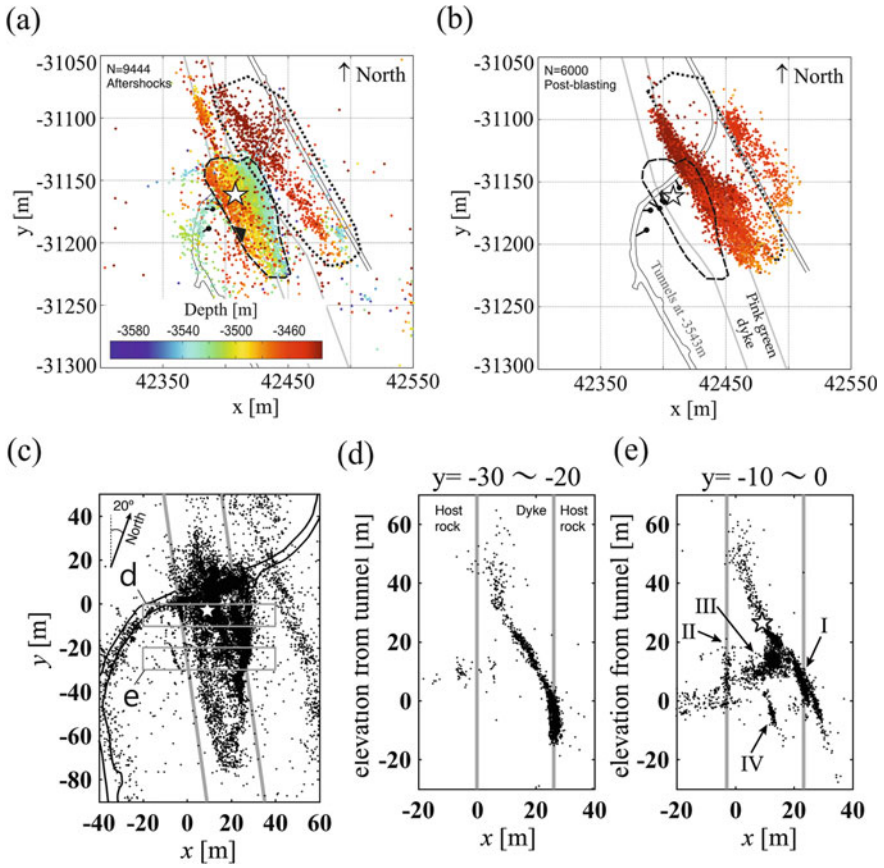

Fig. 10 **a** Map view of the aftershock sequence of M_W 1.9 earthquake. Earthquake hypocenter is shown with star and the aftershocks framing the approximate fault plane area (dashed line) are color-encoded with depth. Note the M_W 1.9 earthquake also triggered seismic activity at the exploitation level (dotted polygon). **b** Seismic activity following blasting sequences at the exploitation level. **c** Zoomed-in map view of aftershock sequence of M_W 1.9 earthquake. Gray rectangles denote parts of seismicity presented in cross-sections (**c**), (**d**). Aftershocks spatial distribution highlights complexity of the fault plane including its bending on the boundary between Ping Green Dyke and host rocks (gray solid lines in all figures). Figure **a** and **b** modified after Kwiatek et al. [5], Figure **c**–**d** reproduced with permission from Naoi et al. [64]

Seismic signals were related especially to the post-blasting activity performed at the exploitation level. These events signified relaxation of stresses in the exploitation area, with AE activity decaying in time following blasting episodes and still identifiable after 12 h the blasting episode took place.

During 2007 Christmas vacation period on December 27th, 2007, when the mine was closed for ten days, an earthquake with relatively large seismic moment magnitude M_W 1.9 struck the area slightly above the tunnel system in the center of the JAGUARS monitoring volume [3, 5, 60, 63, 64]. Naoi et al. [64] manually picked P-

and S-wave arrival times to locate more than 25,000 AE events that occurred within 150 h following the main shock (Fig. 10a). The location uncertainty for AE events within a radius of about 40 m of the center of the AE network was less than 1 m. Most of the AE events from this period occurred within 50–100 m of the network, where the spatial coverage of the network is best [62]. The recorded events contained high-quality signals containing broad range of high frequencies, which allowed to analyze earthquake nucleation processes and post-seismic stress relaxation in extreme details. The outcome of studies is presented in the following paragraphs, as they represent the most complete analysis of an earthquake using in-situ AE monitoring today.

Earthquake preparatory processes and post-earthquake stress relaxation. Hypocenters of AE activity during last 6 months preceding the M_W 1.9 earthquakes signify delineation of the future rupture plane in advance of the main shock [69]. The temporal evolution of AE activity was found to be correlated with the stressing of the area by mining exploitation performed at the stope level. However, the fore-shock activity as a whole did not show any signatures of acceleration ahead of the main shock, contrary to what is typically observed in laboratory experiments on rock samples at smaller scales. The precursory activity tended to accumulate in four spatio-temporal clusters, with three of them being still active until the main shock. Clusters did not change their spatial location in time, however they displayed changes in rates of seismic activity. The rupture initiation was interpreted as breakdown of interacting asperities leading to large slip over the pre-existing plane. The latter was deducted from analysis of borehole cores drilled through the M_W 1.9 fault and evidencing hydrothermal activity localized in the vicinity of the rupture plane [69].

Ziegler et al. [68] investigated the hypothesis that static stress transfer related to the exploitation of the VCR triggered the occurrence of the M_W 1.9 event. The designed detailed finite element 3D geomechanical model of volume presented in Fig. 9 including information on lithology, tectonic and structural features. The performed modeling, including time-mass removal from the exploitation level confirmed the large earthquake was caused by changes in stress state due to progressive exploitation (Fig. 11).

Yabe et al. [61] showed, that the AE events forming aftershock sequence clearly delineated a plane in the PGD with a strike of N22W and a dip of 68° toward N68E (see Fig. 16 in Yabe et al. [69]). Because waveforms of the main shock recorded by the AE network were saturated in AE recordings, the main shock was analyzed using waveform data of the Mponeng mine geophone network. Naoi et al. [64] was able to resolve the fine details of the rupture plane extending 100 m × 80 m within the PGD, which underwent branching and bending according to geological heterogeneities present. They applied the master-event location technique to locate the hypocenter of the main shock relative to the aftershock AE events. The mainshock nucleation point was about 30 m above the AE network and within the cloud of following aftershock activity. The fault plane solution of the mainshock was resolved from waveform data of the geophone seismic network operated by the mine in two independent studies [64, 70] indicating one nodal plane being in agreement with the orientation of aftershock hypocenters.

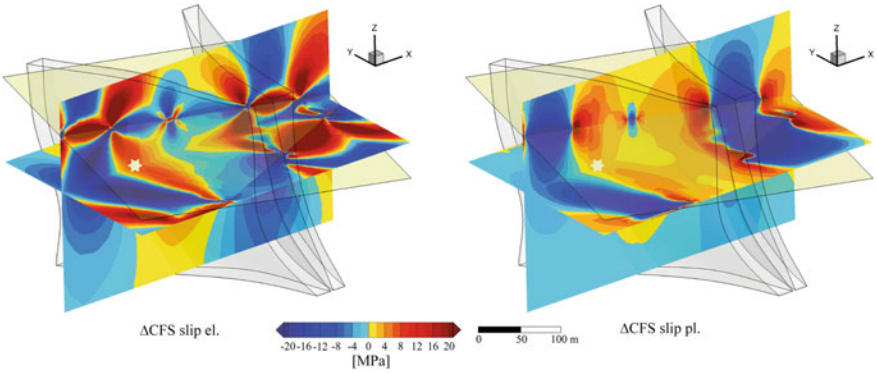

Fig. 11 State of the Coulomb stress just before and in the slip direction of the M_W 1.9 event (white star). Left and right figure show Coulomb stress derived from the full stress tensor, and the vertical component of the stress tensor assuming full dissipation of horizontal stresses (pseudo-plasticity). Stress state is affected by pending exploitation, geological and geometrical features in the modeled volume, with the latter including existence of voids due to exploitation of the stope and tunnels. Reproduced from Ziegler et al. [68]

The aftershock sequence following the M_W 1.9 earthquake was found to follow the Omori's law [3], similarly to that observed at larger scales as well as in the laboratory experiments on rock samples, signifying the relaxation of static stress changes in the vicinity of rupture plane. Static stress changes following larger earthquakes are known to affect the rate and distribution of aftershocks. Kozłowska et al. [70] utilized the catalog framing the M_W 1.9 earthquake to investigate if rate- and state-based modelling [133] is valid for shallow, mining induced seismicity. Their results suggest, that mining-induced earthquakes may be followed by a stress relaxation expressed through aftershocks located on the rupture plane and in regions of positive Coulomb stress change. Furthermore, they demonstrate that the main features of the temporal and spatial distributions of nano- and picoseismicity can be successfully determined using rate- and state-based stress modeling.

The microkinematics of AE events forming the aftershock sequence following M_W 1.9 earthquake was studied by Kwiatek and Ben-Zion [66]. They analyzed radiated energy of nanoseismic and picoseismic activity in order to characterize the potential for tensile event occurrence. For 539 high quality AE events with local magnitudes $-5.2 \leq M_L \leq -2.4$ that occurred close to the JAGUARS network, the S-to-P radiated seismic energy (E_S/E_P) has been calculated. In the following, a shear-tensile model was used to simulate the radiation pattern of P and S phases from a family of rupture models ranging from pure shear to pure tensile failure, accounting for known stress state and expected faulting geometry. The calculations include correction factors for energy estimates associated with given source-receiver geometries and expected focal mechanism with possible tensile component. Synthetic calculations were used to assess the effects of limited observed frequency band and attenuation on the estimated E_S/E_P ratios. Ultimately, the obtained E_S/E_P values were relatively low

(median <5) for the full range of model parameters tested, suggesting that over 50% of earthquakes from the events forming the aftershock sequence display a significant tensile component. The dominance of non-shear kinematics of tiny earthquakes observed in JAGUARS project is comparable to that observed in AE events recorded during stick–slip experiments at higher confining pressures [110].

Statistical signatures of self-similarity of earthquake rupture processes. Several studies, based on the theory of *minimum earthquakes size*, argued that the seminal Gutenberg-Richter frequency-magnitude distribution (FMD) has a lower cut-off [134, 135]. Kwiatek et al. [5] investigated the self-similarity of the earthquake rupture process of post-blasting activity (6,000 events) and aftershocks sequence of the M_W 1.9 earthquake (9,444 events, cf. Fig. 10a, b). They found higher *b*-value ($b = 1.3$) for the seismic activity on the fault plane following M_W 1.9 event, as expected for the aftershocks. Lower b-values has been observed ($b = 1.1 - 1.2$) in induced stress relaxation phases on the stope level following post-blasting activities. This near-source observation suggested that with regard to statistical parameter such as *b*-value, there is no evidence for a physical limit for the nucleation zone nor for a minimum magnitudes down to at least M_W –4.4 in the aftershock activity (Fig. 2a). Also, no difference in FMD between post-blasting datasets and aftershock sequence were found. Therefore, this study concluded that the statistical properties of aftershocks and post-blasting activities are no different than that observed for the larger earthquakes and that observed in laboratory experiments on the rock samples [2].

Davidsen et al. [67] used the aftershock catalog of 9,444 AE events following M_W 1.9 earthquake to study the statistics of magnitude difference between consecutive events forming the catalog that are above a given magnitude threshold. Whether the magnitudes of earthquakes are independent of one another and can be considered as randomly drawn from the Gutenberg-Richter frequency-magnitude distribution is an essential property of Epidemic-Type Aftershock Sequence (ETAS) models [136]. It is also an important feature supporting the idea of self-similarity of earthquake rupture process, forming the basis of many approaches for forecasting seismicity rates and seismic hazard assessment. It was suggested that statistical correlations could exist between magnitudes of consecutive earthquakes [137], implying that one could predict the magnitude of a future earthquake based on the magnitude of previously observed earthquakes. However, the catalog incompleteness can lead to a spurious detection of magnitude correlations. Davidsen et al. [67] found that there is no statistically significant evidence for the presence of magnitude correlations in the JAGUARS dataset. Moreover, no systematic dependence on the magnitude threshold is visible supporting the high level of completeness of the considered catalog. This all implies that the assumption of independent earthquakes magnitudes often used for forecasting seismicity rates and hazard assessment is justified.

The distribution of time intervals between successive earthquakes forming a complete seismic catalog was a subject of the study of Davidsen and Kwiatek [65]. The probability density function of time intervals can be described by a unique scaling function if time is rescaled with the mean rate of seismic occurrence [138, 139]. It was shown this scaling function holds down to small earthquake with $M > 2$ scales occurring in various tectonic environments, even in cases of existing non-stationarities such

as aftershock sequences [138]. Davidsen and Kwiatek [65] analyzed three carefully selected subsets of JAGUARS AE activity associated with silent periods containing background seismicity that is not influenced by the man-made noises nor affected by post-blasting activity. These catalogs were compared to microseismicity observed in KTB project in Germany [140, 141] involving natural seismicity and seismicity associated with fluid injection. They found the resulting distribution of interevent times are form-invariant between the analyzed catalogs, regardless of magnitude, origin of seismicity, and whether the non-stationarities were present.

An important aspect of statistical studies of induced seismicity is the recording completeness of seismic networks and resulting seismic catalogs. High-frequency waves of recorded nano- and picoseismicity observed in JAGUARS project was significantly influenced by local heterogeneities. Plenkers et al. [62] developed a detection completeness analysis that took into account the complex and heterogeneous observational space. The work extended the probability-based magnitude of completeness method [142] to three dimensions by taking into account the direction of observation. This is because the detection capability of each AE sensor was found to change dramatically with the direction of observation due to existence of engineering structures (e.g. tunnels, stope, shafts etc.) and localized geological and tectonic features (e.g. dykes, faults). The performed analysis allowed to identify how different local anthropogenic, lithological and tectonic heterogeneities affect the detectability of event with specific magnitude in particular source-receiver configuration. Plenkers et al. [62] demonstrated that the fracture zone around a tunnel cavity as well as the highly fractured rock near the stope face have a crucial influence on the detection probability. Furthermore, the developed methodology allowed to identify the sensors with poor performance (due to e.g. coupling quality). Ultimately, the study gave an estimate of the magnitude of completeness in three dimension and this knowledge allowed to optimize the selection of catalogs in a number of studies performed in the frame of JAGUARS project.

Source properties and self-similarity. Kwiatek et al. [63] investigated spectral characteristics of AE activity following the occurrence of M_W 1.9 event as well as post-blasting activity. The ensemble of parameters included seismic moment, source size, stress drop and apparent stress. These parameters have been calculated from full waveform data of AE events by applying spectral fitting and spectral ratio methods, identical to that used in analysis of seismic data of natural and induced seismicity at lower frequencies and using the standard seismic networks [143]. Application of standard seismological techniques required that AE sensors are calibrated to the actual ground motions. This has been achieved by cross-calibration of AE waveform data to that recorded by the 3-component accelerometer [88]. Using the waveform data from seismic activity recorded on 3-component accelerometer and co-located AE sensor (cf. Fig. 9) it was possible isolate and extract the transfer function of AE sensor in frequency range 50 Hz–17 kHz, i.e. the flat part of the transfer function of the accelerometer. Using the developed transfer function, any AE recording could be then represented in a form of ground acceleration for frequencies up to 17 kHz. The details of the procedure are described in the supplementary materials of Kwiatek et al. [88].

This study support evidence for the self-similarity of earthquake rupture process from M_W –0.8 down to M_W –4.1. Within this magnitude range no upper limit to the radiated energy of seismic events has been found, with apparent stress value corresponding to that observed in other studies of natural and induced seismicity (see Fig. 10 in [63]). This would mean nano- and picoseismic events forming the JAGUARS catalog radiates a comparable amount of elastic energy per unit slip and per unit fault size as the larger natural and induced earthquakes. Similarly, it was found that the average static stress drop of analyzed events is constant in the considered magnitude range (Fig. 2b), with values similar to that previously reported in South African gold mines [144–146], as well as to that observed in natural and induced seismicity. The results suggest that rupture processes of nano- and picoseismicity observed in JAGUARS are comparable to that observed at larger scales.

Interestingly, spatial variations in static stress drop and apparent stress values were observed. Events with larger stress drops and apparent stresses were found to occur in the dyke, whereas low stress drops characterized AE events occurring in the exploitation level. Such behavior in stress drop and apparent stress response is understandable while considering that brittle and stronger rocks forming the dyke are expected to radiate more energy in form of seismic waves as less accumulate elastic strain energy is spent on fracture propagation [108].

Cook 4 shaft, South Africa. The AE investigations within Cook 4 shaft was a part of Science and Technology Research Partnership for Sustainable Development (SATREPS) [79]. The project was situated at the depth of 1 km in Cooke 4 shaft, previously known as Ezulvini gold mine, in the Republic of South Africa. The project aimed to track at high resolution the propagation of rock damage induced by the advancing mining front exploiting the upper Elsburg reef using a network combining 24 AE sensors and 6 triaxial accelerometers (Fig. 12). The project is an example for applied in-situ AE monitoring research that is of direct interest for the mining industry. Sensors were installed in development tunnels approximately 20–50 m below the exploitation level, leading to a seismic network dimension of 95 m × 50 m × 30 m and a monitoring volume of approx. 100 m × 180 m × 50 m. The instrumentation included 3 Wilcoxon 728 3-component accelerometers with flat frequency response up to 10 kHz in addition to another 3 Wilcoxon 736 3-component sensors (flat part of transfer function up to 25 kHz). The network was completed with 24 AE sensors with useful frequency range up to 50 kHz. All SATREPS AE sensors were grouted. The recorded signals, sampled at 500 kHz sampling rate, were high-pass filters at 50 Hz and 1 kHz for accelerometers and AE sensors, respectively. In addition, 8 geophones operated by Cooke 4 shaft provided coverage for lower frequencies ranging between 200 and 2,000 Hz [147].

Over 1.52 millions of triggered events were recorded between August and October 2011 (50 days). Waveforms of these triggered events were automatically processed to determine P- and S-wave arrivals. Phase information was used to locate 365,237 events using a homogeneous velocity model with $V_P = 5{,}700$ m/s and $V_S = 3{,}600$ m/s determined by independent ultrasonic transmission measurements (Fig. 12). The moment magnitude and seismic moment was estimated using spectral analysis for 98% of located events. The AE sensors were cross-calibrated to ground displacement

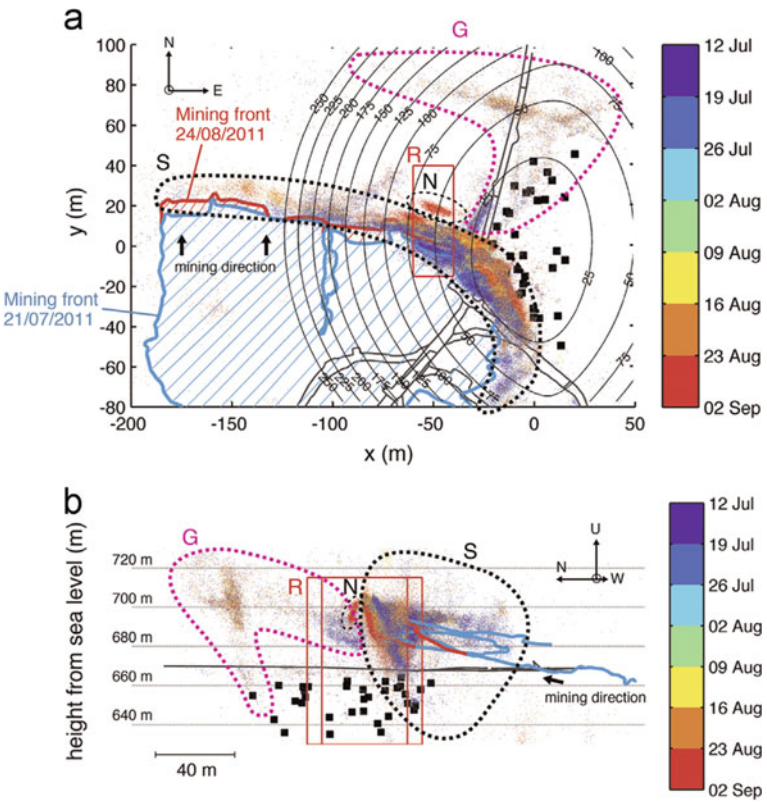

Fig. 12 Locations of AE events recorded during SATREPS project. **a** Map view, **b** NNE-SSW cross section. Black squares denote location of AE sensors. Thick cyan and red lines represent position of mining face on 21 July and 24 August 2011, respectively. The origin time of AE events is color-coded. Closed dotted curves denoted S, N and G identify different populations of seismicity of different origin. Reproduced from Moriya [79]

using available accelerometers following the similar procedure as that developed in JAGUARS project [63]. The recorded moment magnitude ranged from M_W –5.3 to 1.3 [79].

About 90% of AE activity located along the exploitation front and remaining 10% formed a number of subplanar structures extending further away along pre-existing larger fault plane structures located in the area (Fig. 12). Naoi et al. [6] analyzed the frequency-magnitude distributions (FMDs) of seismic activity occurring near an active mining front. They stacked post-blasting activities and investigated how mining blasts affect the size distribution of recorded earthquakes. They found the calculated FMDs from various post-blastic datasets follow the Gutenberg-Richter power law and display comparable *b*-values ranging $b = 1.1$–1.3. No systematic evolution in time of *b*-values have been detected, suggesting that fracture and frictional processes in rocks follows the same frequency-magnitude statistics.

High resolution mapping of fractures and faults. Moriya et al. [79] applied the Joint Hypocenter Determination (JHD) method followed by the double-difference relocation technique [148] to improve the relative precision of earthquake hypocenters forming the AE activity occurring near the mining front. It was found that the activity front migrated with the progress of the mining front AE activity correlated in general to the expected stress field pattern in the vicinity of the mining front rather than the specific geological structures (i.e. above or below the exploited are). The JHD method allowed to identify steeply dipping planar clusters within the previously homogeneous cloud of seismic events occupying the rock volume ahead of exploitation front. Most of these clusters were striking in the direction of the exploitation front, lighting up zones of macroscopic shear fractures forming ahead of exploitation front (Fig. 13) and called Ortlepp shears [149].

The moment magnitudes of AE activity highlighting future Ortlepp shears ranged –4.3 to –0.4 corresponding to 8 cm–7 m size assuming 3 MPa static stress drop. One planar cluster with different orientation was correlated to an existing minor fault. Interestingly, limited AE activity was observed directly at the exploitation horizon, where tensile fractures were expected to occur. It is feasible that tensile fractures that were supposed to dominate at the exploitation horizon display reduced radiation of elastic waves due to low tensile fracture toughness of rocks in comparison to considerable frictional resistance that has to be overcome to cause shear fractures [79]. Naoi et al. [77] investigated the spatio-temporal and statistical properties of AE activity associated with known fault structures in the vicinity of the project, excluding the activity ahead of exploitation front discussed in Moriya et al. [79]. The relocated data provided detailed picture of spatial features of fault zones lighted up by the AE activity. Six planar clusters of AE activity exhibited very sharp event distribution with a total thickness of a few decimeters only that was comparable with location precision after double-difference relocation. This suggested AE activity was strictly associated with the corresponding fault core. The AEs location precision allowed

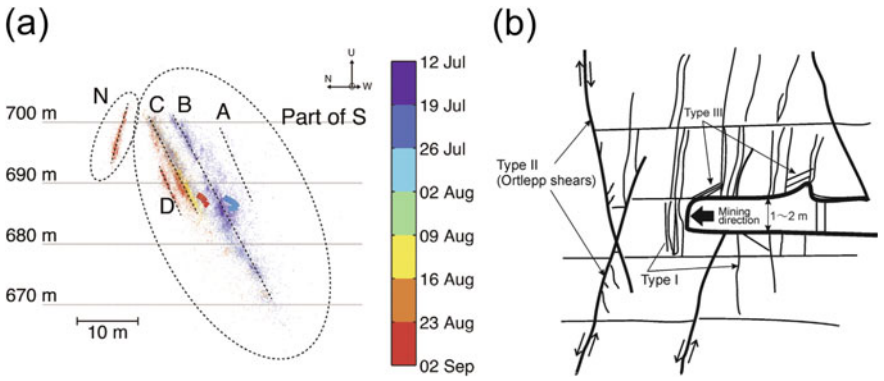

Fig. 13 **a** Depth distribution of seismicity with temporal evolution color-coded in time. **b** Schematic sketch of fracture network developing ahead of active mining front (after Adams et al. [150]). Modified after Moriya et al. [79]

to delineate some higher-order features such as branches and step-overs. Composite focal mechanisms estimated from first P-wave polarities of AE signals indicated kinematics in agreement with orientation of macroscopic fault planes. Rates of AE events were found to be approximately constant on all six faults, suggesting that the studied geological discontinuities are subjected to a constant loading. In five cases the Gutenberg-Richter values were found to be relatively high ($b = 1.3$–1.6) and stationary. One planar cluster [76] displayed very high b-values of 2.6 that evolved in time (see next section for more detailed AE activity associated with this fault). It was suggested that recorded on-fault activity reflect its topography (asperities).

Tracking aseismic slip in high resolution. It is known that aseismic slip sometimes occur on faults preceding an earthquake [129, 134, 151]. Aseismic phenomena are valuable source of information to understand earthquake preparatory processes. At large scales, the detection of aseismic slip relies on availability of close-by geodetic signals that are typically scarce, whereas at small laboratory scales the aseismic slip can be directly monitoring using strain gages. Alternatively, spatially migrating swarm-like-clusters of tiny earthquakes has been observed in studies of natural seismicity and laboratory experiments [152–154]. The spatial evolution of clusters, interpreted as progressive destruction of asperities forming the fault plane have been interpreted as a signature of aseismic slip occurring in the surrounding area of the fault plane. Moreover, the rate of repeating microearthquakes occuring at the same location of the large fault zone were thought be proportional to the aseismic slip rate of the fault [153] and used to assess the amount of aseismic slip rate [155–157]. The high-resolution seismic network installed in Cook 4 shaft allow to monitor very small seismic activity and repeating event clusters associated with aseismic slip of the two faults in unprecedented details [76–78]. Naoi et al. [76] investigated double-difference relocated catalog of AE activity composed of 7,557 events ($-3.9 \leq M_W \leq -1.8$) and source radii 6 – 70 cm that occurred on a steeply dipping pre-existing fault located N from the active exploitation front. The resolved hypocenters of AE activity sharply delineated two narrow planar zones striking in direction similar to the stope front that were lately, when the mining front passed through the area, identified in-situ as a fault with foliated gouge zone up to several centimeters thickness. The AE activity formed ahead of the mining excavations in response to increased stresses due to the approaching mining front. It was found that the seismic activity was progressively expanding in time both along strike and dip of the fault throughout the whole monitoring period. At the beginning, only small events with $M_W < -3$ were occurring in the area. The progressive increase in the number of larger AE events reaching M_W –1.8 was observed towards the end of the 3-month lasting monitoring, depicted by the drop-down in Gutenberg Richter b-value from $b = 2.6$ to $b = 1.37$, signifying increased stress in the area [158, 159] and/or progressive coalescence of cracks over the macroscopic fault plane. Source dimensions of AE events were estimated using spectral analysis using corner frequencies and seismic moments of AE sensors cross-calibrated with accelerometers [6]. Source sizes were found to be much smaller than the spatial extent of clusters, which together with temporal evolution of seismicity suggested that expansion of clusters in space and time was quasi-static. Interestingly, over 25% of the largest events with $-2.5 \leq M_W \leq -1.8$ that occurred in

one cluster were found to be repeating events, with many AEs repeatedly re-rupturing in discrete tiny spots over the much larger macroscopic fault plane.

Observations of Naoi et al. [76] provides evidence for progressive aseismic slip along the pre-existing geological fault. They propose AE activity represents unstable violent failures of the locked parts of the fault (asperities), loaded by the stress changes due to stable sliding of the surrounding parts of the fault [153]. The visible upper constrain to the size of AEs suggested the upper limit to the size of asperities existing over the fault surface. Time-dependent expansion of AE activity over the fault surface would indicate the growth of a slow-slip patch, which is in striking similarity to processes observed at plate boundary [151] and laboratory scales. As during the monitoring period no large events spanning the whole fault surface was detected, this suggested the fault remained in preparatory phase displaying only the quasi-static growth of the slip patch.

Naoi et al. [78] investigated a subset of 851 very small earthquakes with magnitudes ranging $-5.1 < M_W < -3.6$ occurring on the Zebra fault, the major tectonic feature in the monitored rock volume, which was the original monitoring target of the AE-accelerometer network installed in the Cook 4 shaft. Using relocated catalog and waveform cross-correlation analysis, over 45% of AE events occurring on this fault during 2 month lasting monitoring period were identified as repeaters. A total of 111 repeater groups with 2–16 AE events were detected. Repeaters were occurring steadily at discrete locations and were characterized by similar magnitudes, which is similar to what is observed for repeating earthquakes observed at plate boundaries [153]. Such behavior has been suggested to signify the repeated ruptures of asperities on the fault that is loaded by the surrounding aseismic slip, with the latter being caused by the progression of mining front.

3.2 In-situ AE Monitoring in Salt Mines

This section discusses analysis of AE data recorded in three different projects located in salt mines focusing on long term structural health monitoring, the reaction of salt rock to (thermal) loading, the role of stress memory and novel analyzing techniques of secondary wave arrivals. Due to the homogeneity and the low intrinsic damping, in-situ AE monitoring in salt rock provides data of high quality and allows especially sensitive monitoring. Most research projects in salt rock are conducted in the context of nuclear waste storage investigations.

Salt Mine Morsleben, Germany. The Morsleben repository is located in Saxony-Anhalt near the border to Lower Saxony. Around 37,000 m^3 of low and intermediate-level waste with negligible heat generation were permanently stored here between 1971 and 1991 and from 1994 to 1998. The Bundesgesellschaft für Endlagerung mbH (BGE) is operating the repository. Long-term in-situ AE monitoring in Morsleben has been carried out both in the central (since 1994) and southern sections (since 1997), and is still ongoing. The exceptional long term observation is an outstanding example of long-term structural health monitoring using in-situ AE monitoring. The

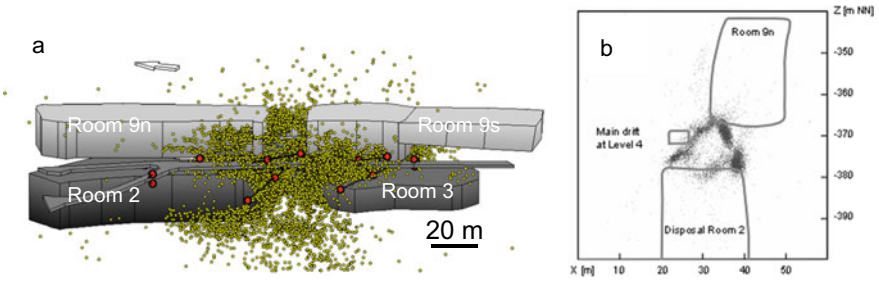

Fig. 14 **a** Perspective view of cavities and the main drift at two levels (Rooms 9n and 9s and Disposal Rooms 2 and 3) in the southern part of the Morsleben salt mine. The red dots indicate the AE sensors in boreholes, the yellow dots represent the locations of 41,521 high-quality AE events recorded over the course of 5 years [51, 52]. **b** Located AE events in vertical cross section through the upper Rooms 9n and 9 s and the lower Room 2 and 3. AE activity is clearly clustered in bands representing zones of high shear stress. Reproduced with permission from Spies et al. [51]

results of the in-situ AE measurements are interpreted in conjunction with results of other geo-mechanical investigation methods such as model calculations, laboratory tests, and in-situ measurements of deformations and stresses (see www.bgr.bund.de).

Morsleben, Southern section. The in-situ AE monitoring system in the southern part of the mine is focused on the area between two upper and two lower chambers. Low level nuclear waste is stored in the two lower champers named Room 2 and 3. A drift is located at the level between the upper and lower rooms. The average depth level of the cavities is about 500 m below surface. In-situ AE monitoring serves for structural health monitoring. The network geometry is given in Fig. 14a. In total 24 AE sensors are installed in boreholes of up to 30 m length which were drilled from the main drift because the rooms are not accessible anymore (red dots). Figure 14a shows 41,521 located events (yellow dots) which were located in a time period of approximately 5 years; only the strongest events which were precisely located using at least 30 P- and S-wave arrival times are plotted. These AE events were generated by microcracking due to deformation in rock salt above the so-called dilatancy boundary. It can be seen, that most of the events accumulate in the pillar between Rooms 9n and 9 s and in the areas between the upper Rooms 9n, 9s and the lower Rooms 2 and 3.

The events in further distance from the galleries are caused by microfracturing at discrete anhydrite layers included in the rock salt formation. These AE events are caused by redistribution of stresses around the cavities which includes the nearby anhydrite layers, leading to stress concentrations.

For a more detailed representation of all data including the smaller events, AE locations in the vertical cross section through the cavities are given in Fig. 14b. Data from a time interval of one month—about 10,000 events—from a spatial interval of 20 m thickness were projected into the cross section. The AE locations in Fig. 14b show a dense accumulation of events between the corners of the higher and lower rooms. The reason for the high microcrack activity are “bandlike” structures of high shear stress leading to creep deformation of the rock salt accompanied by

dilatancy [51]. Finite element calculations using a viscoplastic material law show good correlation between the calculated stresses and the located AE events [51]. Zones of high shear stresses and deformations between the excavations (shear bands) coincide well with the zones of dense accumulations of AE events. A detailed moment tensor analysis of the strongest events in the shear bands pointed out, that these events display shear and tensile mechanisms [48].

Morsleben, Central section: With the same purpose as described above for the southern section in-situ AE monitoring has been carried out in the central section of the Morsleben repository. Mining in these areas continued until the 1960s. Here, borehole sensors are distributed at three excavation levels and installed in 3–20 m deep boreholes. Originally, a network of 24 AE sensors monitored this section and covered an area of 150 m × 100 m × 120 m. This network was enlarged to 48 channels and covers a rock volume of about 250 m × 200 m × 120 m [51, 53, 55] as shown in Fig. 5a. The average depth below surface of the monitored volume is 400 m. This in-situ AE monitoring provides a dataset of currently approximately 15 million located AE events per year [160]. For most events no waveforms are stored, but only the results of real-time processing. To maintain the integrity of the barrier to the top of the salt deposit and the stability of the rooms for a long time, the rooms in the central part were backfilled with salt concrete from September 2003 to January 2011.

During and after backfilling, the rock in the vicinity of these rooms were additionally loaded due to thermally induced stresses by released heat during hydration of the salted concrete for a period of several months to several years. In this period a strong increase of the microcracking activity was measured up to approximately 1,200 events per hour with beginning of the backfilling starting from September 2003 [85, 161]. Using a 2D finite element thermoelastic stress model, Becker et al. 2010 are able to show that the spatio temporal AE event distribtution is in agreement with calculated stresses. Analyzing different backfilling cycles they find that the rock salt exhibits a pronounced Kaiser effect for the first few thermal loading cycles throughout the whole study region, i.e. a pronounced stress memory effect is observed with almost no AE activity in times where stresses are below the former maximum stress and a steep increase in activity when stresses become larger (Fig. 15). The deviation from the Kaiser effect during later loading cycles is coinciding with the initiation of a planar macroscopic crack.

Figure 16 shows the AE activity in an subsection of the network over the ridges of backfilled excavation chambers. The view is downwards in diagonal direction (see https://www.bgr.bund.de). The located AE events and the AE borehole sensors are marked by black and red and blue dots, respectively. This figure shows an example of the localized AE events [162]. High microcrack activity takes place above the mining chambers and in their joints even several years after completion of the backfillings. Almost a year after backfilling of the cavities in 2003, AE events are distributed with distinctive stripe shapes above cavities at different depth levels. The physical forces driving the creation of these stripes are still unknown. One possible explanation might be that these spatial patterns of the AE activity originated from the extensional stress developing in the cavities roofs. This strip-shaped pattern runs transversely to

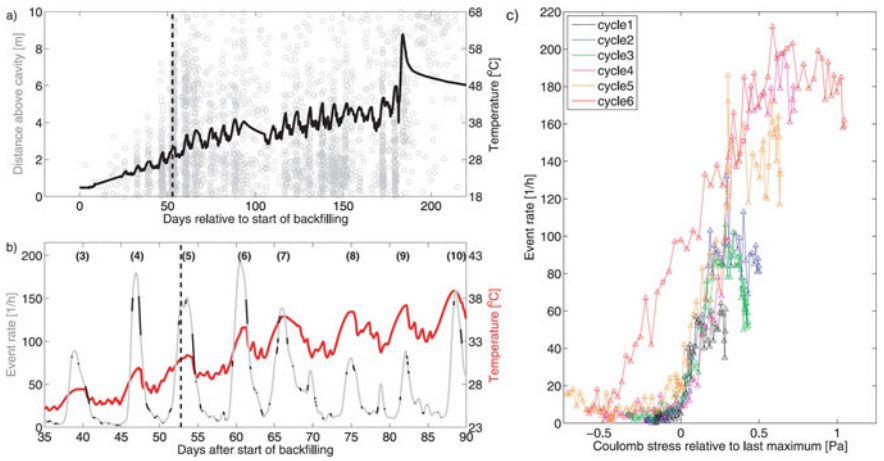

Fig. 15 Correlation of AE activity to temperature and stress memory effect. In **a** the location of AE activity (grey circles) and temperature is shown over time. In **b** the temporal correlation between increased activity and temperature is shown. Based on stress modeling results in **c** the event rate is shown over the coulomb stress relative to last maximum stress, presenting a strong stress memory effect (Kaiser effect). The different cycles refer to different cementation phases. Figure Reproduced with permission from Becker et al. [58]

the longitudinal axis of the excavation in the ridge area of the room [161]. But, the stripe-shaped clusters indicate the formation of macrocracks due to stress changes [163].

In-situ AE monitoring in the salt mine Morsleben provide a very large and unique dataset of approximately 100 million located AE events and it offers a wide range of options for evaluating fracture processes in a salt mine. Unfortunately the analysis is limited by the restriction that for most events no waveforms are stored. In conclusion, the AE activity in salt rock is detected around open cavities and at the boundaries between different rock types. Creep processes cause high AE activity due to high deviatoric stresses at the walls of the cavities in the EDZ. This kind of AE activity is interpreted as ongoing deformation (convergence) in the vicinity of the open cavities and it is always present until convergence has been stopped, e.g., by backfilling of the open cavities. Apart from seasonal fluctuations due to the variation of humidity, the AE activity does not vary with time.

The Asse II salt mine in Germany. The former salt extraction mine and nowadays a research facility and test repository for low and medium radioactive waste is located in Lower Saxony, Germany. The main hazard in the mine is associated to the risk of permanent brine inflows due to failure processes in pillars and tunnels in the southern flank and in the adjacent overburden [164, 165]. We present the study of Philipp et al. [81] as it represents the possibilities of an array network for structural health monitoring in the context of failure processes and the study of Pisconti et al. [82], because it presents novel applications using the full waveform by applying array methods to the coda wave of AE signals to gain insights into the travel path.

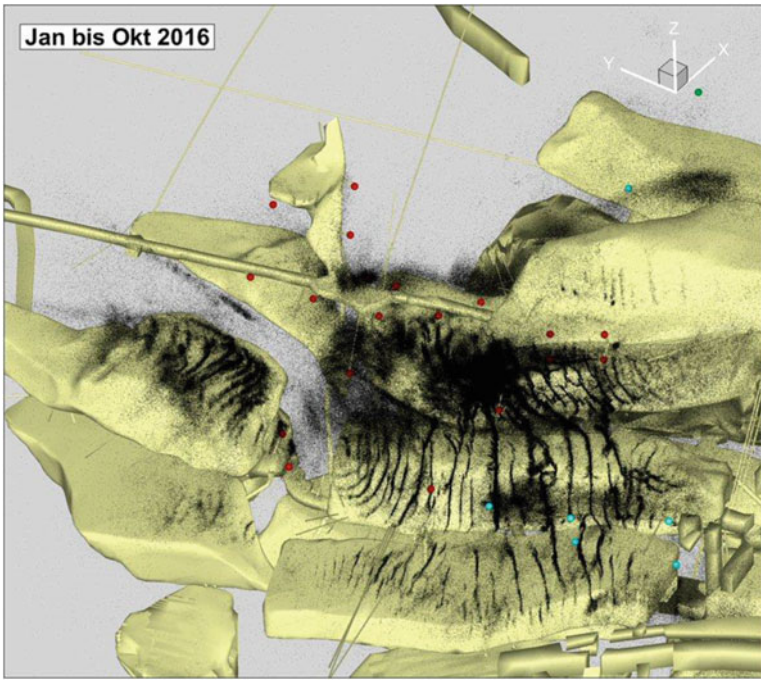

Fig. 16 AE activity (black) in the area of ridges and impacts of mining chambers (yellow) in the central part of the Morsleben repository. Spatial representation with view direction diagonally downwards, AE sensors in red and blue. Patterns of approximately parallel stripes of AE activity over the ridges of backfilled excavation chambers. The view is downwards in diagonal direction (see https://www.bgr.bund.de) [162]. Reproduced with permission

Philipp et al. [81] report on structural health monitoring using AE sensors installed in cavity roofs to monitor failure processes in the upper part of the salt dome. It is expected, that AE events outline weakening in rock, structural damage due to dilatation and other dynamic processes long before significant damage is visible in the chamber's roof and in areas that are not accessible.

The monitoring system consists of two networks with 16 AE sensors each, which are installed in short borehole of 1–3 m length in the chamber's roof (see Fig. 5c). Data is recorded in trigger-mode (1 MHz sampling rate) and automatically processed i.e., that events recorded are localized in near-real time. For this P- and S-wave onset picking is performed using a picking algorithm based on the Hilbert transform. The network geometry of both networks (network dimension 37 m $\times$ 31 m $\times$ 5 m and 46 m $\times$ 39 m $\times$ 4.5 m) differs owing to the actual usage of the two chambers that define the accessibility of the roof for sensor installation e.g., the roof could not be accessed above three large brine ponds. The monitoring project has been ongoing for several years, but the study considers data of a 10-month period, namely the time period 4 February to 31 November 2013. In this time period more than 100,000 AE events were recorded that populate a rock volume of approximately 250 m $\times$ 250 m

× 160 m outlining dynamic processes not only in the chambers roof, but also in the salt dome flank and in the upper salt dome.

AE activity recorded clusters strongly in space (Fig. 17) in four regions: the cavity roof, the salt dome's southern flank, where most of the brine inflow occurs, the salt dome top and the northern flank. More than 70% of the located AE events occur along the southern flank, due to the low wave attenuation of salt rock, the AE networks is able to record events with source–receiver distances greater than 150 m are possible.

The observed AE activity within each cluster is not distributed homogenously, but outlines clearly planes of activity. In the chamber's roof most events outline planes oriented east–west and dipping to the south according to the salt's layering. The events extend up to 15 m from the roof into the salt rock, but at greater depth no activity is recorded, which demonstrates that currently no active damage process is occurring. In the roof of the chambers, all events occur in a homogenous part of the younger salt rock (Leine formation) and most likely correspond to damage processes owing to stress re-distribution. A geomechanical survey confirmed an increased permeability in the area of AE clusters, but did not show macroscopic damage. In the area close to the southern flank the events outline a plane of activity that is oriented roughly

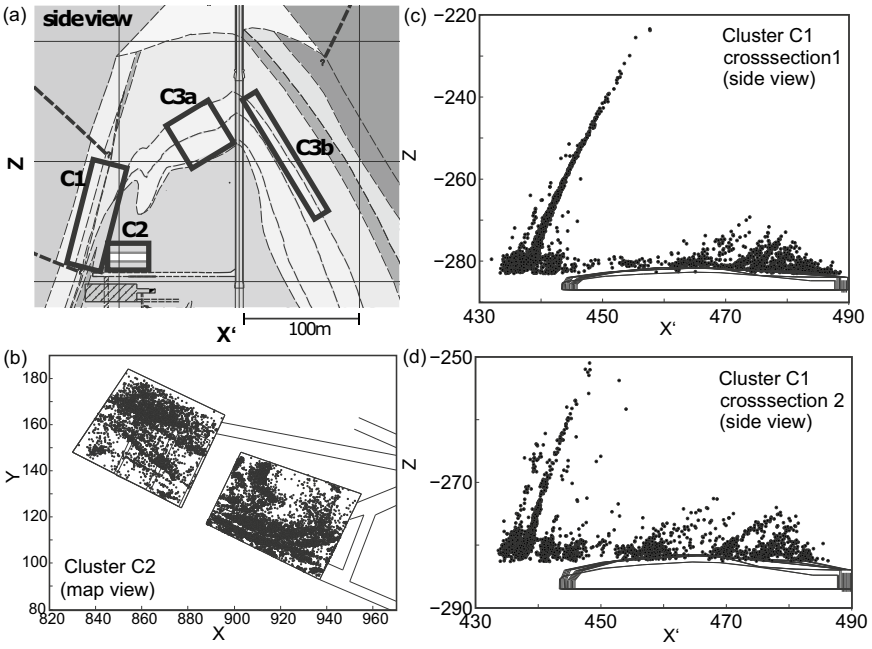

Fig. 17 AE activity recorded in the ASSE II salt mine. **a** Geologic cross section (sketch) of the Asse salt mine with the four AE clusters C1, C2, C3a, and C3b. **b** Map view showing the locations of AE events (black dots) in cluster C2 in the chamber roof. **c**, **d** show cross sections through cluster C1 and C2 above the chamber and along the anhydrite-host rock boundary at the southern flank. All dimensions are given in meter. Reproduced with permission from Philipp et al. [81]

east–west and dipping to the south. The AE events seem to follow the rock salt-anhydrite-sandstone rock boundary, which is subject to significant geomechanical processes including the loss of integrity owing to a barrier thickness of only 15 m in the upper mine. Events are observed as far as 70 m above the network. Within this plane, AE events cluster on vertical structures. It is concluded that although a singular AE event is too small to have a damage potential, the AE events are clearly able to outline areas and, even more precisely, the exact position, extension, and orientation of potential damage zones.

The cluster in the upper salt dome and near the northern flank is analyzed in more detail by Pisconti et al. [82]. The aim of the investigation is to get knowledge about the position of lithological boundaries in the upper part of the salt mine Asse II and to test whether damage e.g. large fractures in the seismically not active zones above the chambers can be excluded. For the analysis Pisconti et al. [82] apply array seismology methods normally used to survey the Earth mantle.

By applying slowness-backazimuth analysis on the filtered envelope beams of the events the authors are able to look into the direction of the incoming energy for both direct P-wave arrival as well as secondary arrivals of scattered waves. The latter waves are hardly visible in the raw waveform alone, but become pronounced by utilizing the array in the beamforming calculation. For the 52 analyzed events, the average discrepancy between observed and theoretical slowness values for the direct P wave is of the order of only 2° of difference in incidence angle and 3° average residual in backazimuth which confirms that the first arrival corresponds to a direct ray pathes. This indicates that no damage like fracture zones or larger open fractures that would cause ray path bending are existing in the rock volume above the chambers.

The slowness-backazimuth analysis of the secondary, reflected waves allows to estimate the location of the reflection points, which correspond to interfaces with a significant impedance constrast. In the dataset analyzed the vast majority of reflection points identified correspond to a cluster of back-projected reflection points delineating a southwest dipping steep (≈70° from horizontal) reflector located at a distance of about 70 m southeast of the network above Chamber A3 (yellow ellipses in Fig. 18c).

It has a depth extension of about 80 m and is about 60 m long, with a strike direction about WNW/ESE. There are also four scatter locations which are further away from the cluster (green ellipses in Fig. 18c). The authors conclude that the majority of reflection points outline the known lithological boundary of the southern flank, but no other additional dominant structures are discovered. The authors conclude that the application of array methods developed to study the Earth mantle was successful. This novel approach for in-situ AE monitoring allows to extract additional information from AE event waveforms, by studying formerly unused parts of the coda wave in order to gain information on the rock volume passed through. This is especially useful in applications where areas, structures or lithological boundaries are inaccessible, but an estimation of their position is needed.

Salt Mine Merkers, Germany. A borehole-loading experiment, where a large-diameter borehole is pressurized first by gas injection and in a follow-up project

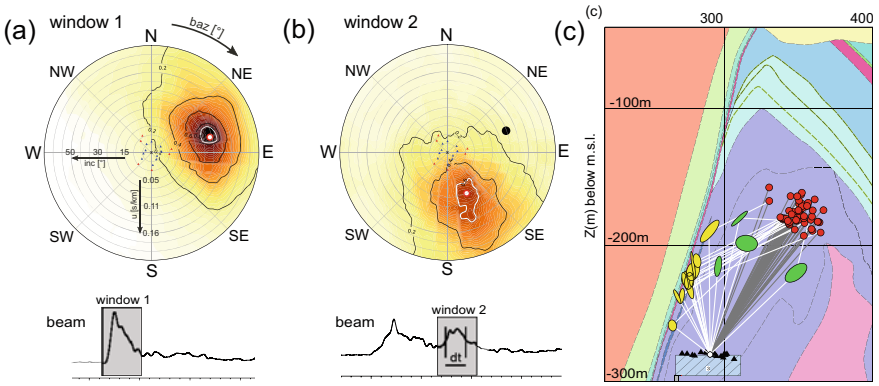

Fig. 18 Locating lithological boundaries using array techniques on the Asse Salt mine AE data. Polar plots of slowness backazimuth contours for the beam power of the direct P wave arrival (**a**) and the secondary wave (**b**) are shown, presenting the incoming direction of the energy as function of backazimuth (baz) and slowness (u) at the A3 network (displayed as reference at the centre of each polar plot). The beam power is normalized to the power of the direct P-wave energy. The white contour line in the polar plots of time windows 1 and 2 indicates the 0.9 isoline of the maximum for each arrival in the normalized beam power, from which we computed the uncertainties in slowness and backazimuth. Results in (**a**) show a strong direct P-wave arrival with slowness and backazimuth in the direction of the source, whereas (**b**) shows a dominant out of plane secondary arrival with energy maximum coming from the southeast and travelling with a difference of 80° to the direct P wave (shown by the solid black circle). In both (**a**) and (**b**) the envelopes of the stacked signals of the array are shown at the bottom. Note that the secondary wave arrival not clearly visible in the original waveforms becomes clearly visible by array stacking. In (**c**) the calculated scatter points corresponding to the angles observed for the secondary wave are shown as yellow and green ellipses. Here AE sensors are shown as black triangles and events are shown as red circles. The results demonstrate that secondary reflected waves of AE activity are able to locate and visualize lithological boundaries and array techniques can be applied to the high-frequency domain. Reproduced with permission from Piconti et al. [82].

by brine injection is reported by Manthei et al. [72], Popp et al. [73], and Plenkers et al. [74]. The project aims at studying the so-called gas-frac scenario discussed in nuclear waste storage research. The project looks into the effects of time-dependent pressure build-up on rock integrity for cases in waste depositories where significant gas quantities may be generated in the long-term (e.g. due to anaerobic corrosion, if humidity is present). The experiments highlights the presence of rapid (e.g. the formation of the EDZ) and slow processes (percolation) being monitored with in-situ AE monitoring, i.e. the experiment shows that quite different processes that influence the strength and the permeability of rock are successfully monitored using in situ AE monitoring technique. In the initial experiment that took place from January 2010 to the end of 2011 the rock response of four different stages were monitored using in-situ AE monitoring: (1) pre-excavation; (2) drilling of wide-diameter (1.3 m diameter, 60 m extension) borehole; (3) partial backfill with MgO concrete to create gas tight seal; and (4) borehole loading with compressed air. In the follow-up experiment, that

took place in the same wide-diameter borehole in October 2017 to late 2020, the rock response to brine loading was monitored [74].

The monitoring system of the first experiment consisted of 12 side-view AE sensors installed in four monitoring boreholes in 12–15 m distance to the large injection borehole. The sensors were equally spaced along the borehole and monitor the whole borehole with a similar recording sensitivity. The AE events are recorded in trigger mode. The dimension of the network is 28 m × 25 m × 27 m monitoring a rock volume of approximately 120 m × 120 m × 100 m, as visible in Fig. 6 in Plenkers et al. [74].

In total, more than six million AE events were recorded and located. Highest event rates are found during excavation and cementation (Fig. 19a, b) when more than 170,000 events are recorded and located per day (Fig. 19c). It is shown that the activity starts in formerly inactive homogenous salt rock as soon as excavation is starting, outlining the formation of the excavation damage zone. During cementation an outward migrating front of AE activity is observed, outlining the heat and humidity transport into the rock. Both during excavation and cementation the AE activity is restricted to less than 2 m distance to the borehole and a steep drop in activity rate nearly to the level of background seismicity rates (approximately 100–300 events per day) is observed as soon as the operations finished.

Starting from June 2011 the wide-diameter borehole was loaded stepwise with compressed air. The pressurization took place in several steps. Each time, when pressure was increased, the daily activity rate increased by a few hundred events. From 19 to 24 January 2012 at a pressure of 60 bar a total number of 251 AE events were observed that migrated as far as 20.2 m from the wide-diameter borehole, distances

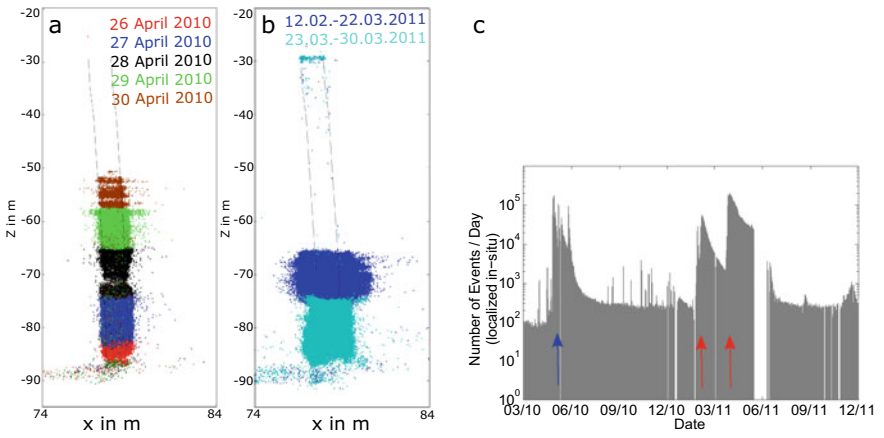

Fig. 19 Temporal and spatial distribution of AE events in the Merkers pressurization experiment. The location of AE events during excavation (**a**) and cementation (**b**) are given in side view projection. The number of events per day of the whole monitoring period from March 2010 to December 2011 is shown in **c**. The blue and red vertical arrows indicate the start of excavation and cementation, respectively. Figure Reproduced with permission from Plenkers et al. [74]

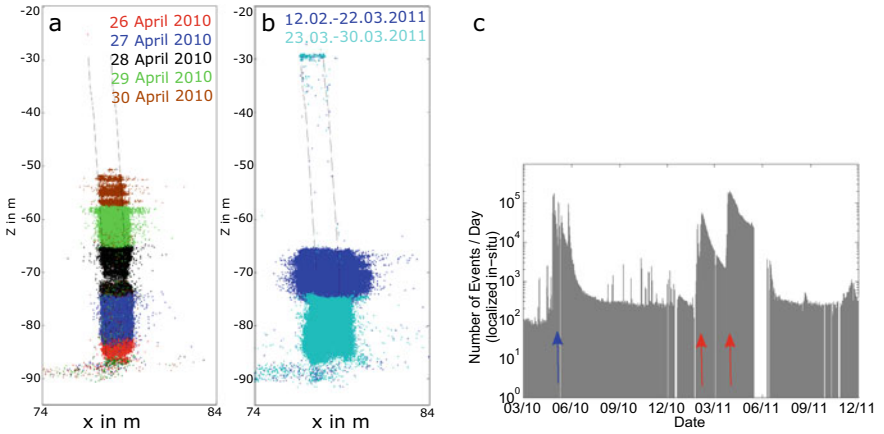

Fig. 20 AE swarm activity during gas-brine break-through in map view (**a**) and side view (**b**). For orientation, the neighboring pillars are shown in dark grey in **a**. Here colored dots show the location and temporal distribution of AE events recorded. Color-coded lines mark the most outward extension of AE seismicity with time, which shows a migration of 0.6–3.4 m per day. In **b** the cemented plug is shown in grey and the positions of AE sensors are shown by red triangles [74]

observed for the first time in the experiment. The events located on a horizontal plane with 2 m vertical expansion (Fig. 20). The events migrate slowly with a progression speed of 0.6–3.4 m/day away from the large diameter borehole revealing a horse-shoe shaped migration front. On 24 January 2012 a gas and brine breakthrough was observed at two monitoring boreholes in combination with a pressure drop from 68 bars down to 56 bars. If follows that the AE activity outlined the migration of the gas and a small amount of brine (from the cementation) from the wide-diameter borehole plug into the salt rock. Because no macrofracture could be identified by camera inspection, no larger seismic event was recorded and because the salt rock regained tightness only weeks after the breakthrough as confirmed by a second pressurization test, the author conclude that the AE events represent the break down of individual grain boundaries in the salt rock (source radius of a few centimeters) during percolation of the gas and brine mixture, i.e. the slow aseismic opening of a pathway for gas-brine transport by percolation is accompanied by AE events.

3.3 AE Monitoring in Hydraulic Stimulation

In hydraulic stimulation (HS) engineered fractures are generated underground by packer probes in boreholes that are pressurized with water until the rocks fracture breakdown pressure is reached. HS is used in industry in a broad variety of contexts, many of which require detailed knowledge on the damage process actively initiated. HS is a common tool for underground stress determination and provides important

input for designing the stope layout and for risk assessment [166–168]. Moreover, HS has become a widely used engineering tool in reservoir enhancement of geothermal systems, shale gas, or conventional oil and gas extraction as it effectively increases the permeability [169–173]. In addition, HS is successful in increasing the productivity in ore production e.g., HS is used in fragmenting ore bodies [174].

Several research projects have addressed HS using in-situ AE monitoring to increase the understanding of the rock response to HS, to study the evolution of fracture generating and predict the stimulation of existing fractures [68, 175, 176]. Recently the research in this field was significantly advanced, because on the one hand side there is a world-wide interest to exploit geothermal energy in order to replace nuclear or fossil energy resources, but on the other hand deep geothermal projects worldwide experienced severe challenges in controlling the induced seismicity and in engineering sufficient connectivity in between injection and production boreholes (Fig. 21). The experiments have not only recorded very interesting and rich data, but have pushed the limits in underground AE monitoring, multi-sensor deployments and advanced signal processing.

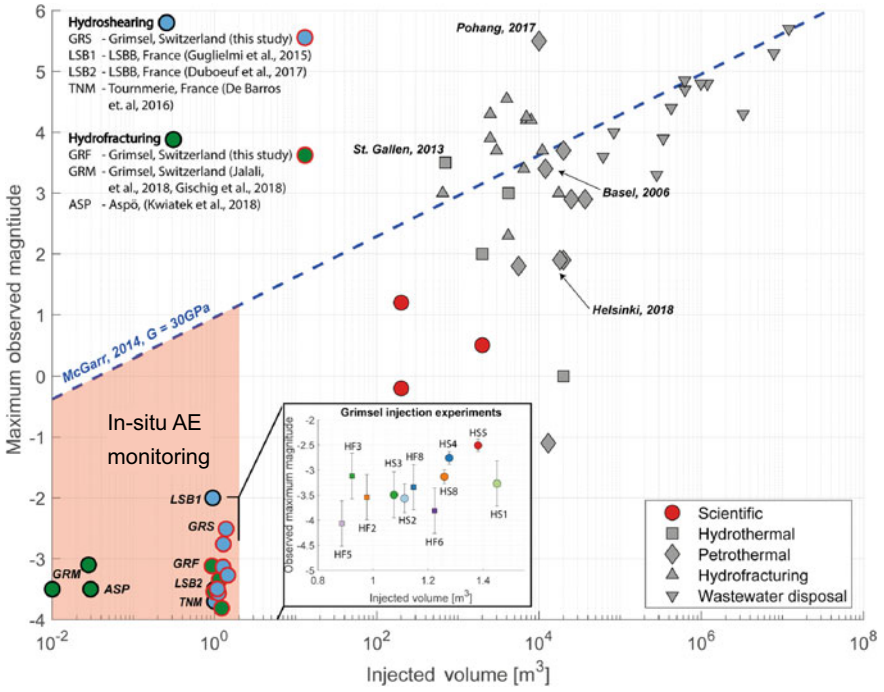

Fig. 21 Induced Seismicity in Hydraulic Stimulation on different scales (Figure taken with permission from Villiger et al. [85]). Injected fluid volume versus maximum observed magnitude of seismicity induced is shown with data taken from Evans et al. [177], McGarr 2014 [178], Atkinson et al. [179], Obermann et al. [180], Häring et al. [181], Grigoli et al. [182], Kwiatek et al. [183]

In this subchapter we discuss recent, large-scale in-situ experiments focusing on HS and point out especially novel analysis techniques, applications and insights in rock fracturing processes, as these developments advance in-situ AE monitoring as a whole. Other HS experiments are summarized in Table 2 together with the references relevant for in-situ AE monitoring.

Bernburg Salt Mine, Germany. This hydraulic fracturing experiment located in the salt mine Bernburg, Germany, took place from Dezember 1994 to February 1995 at the 420-m level in the Leine rock salt [48]. The test site is located in the barrier pillar between gallery XVIII and the western sidewall of a huge chamber of 120 m length, 25 m width, and 30 m height approximately 20 m away (Fig. 22a). Due to the high degree of excavation the barrier pillar is under high compressional and differential stresses with maximal and minimal principal stresses of approximately 25 and 10 MPa, respectively. Six hydraulic fracturing tests and additional refracturing tests with an injected oil volume of 100 and 300 cm^3, respectively, and injection time intervals of 15 min have been carried out in an horizontal injection well (diameter 42 mm, length approximately 12 m). Eight AE borehole sensors (Fig. 22b) were placed in four observation boreholes (10 m length, 100 mm diameter) around the

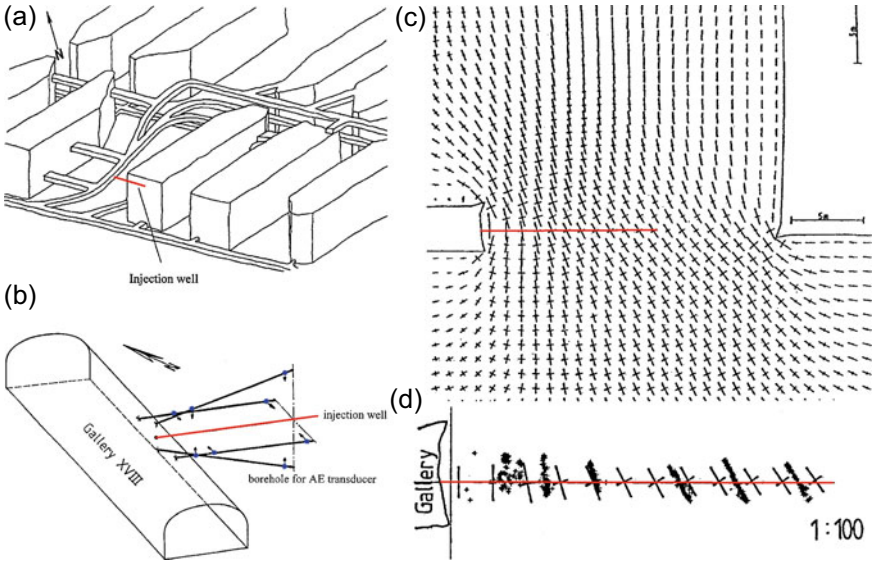

Fig. 22 Hydraulic fracturing experiment in Bernburg Salt mine. **a** Test site of the hydraulic fracturing test series at the 420-m level in the vicinity of huge chambers. **b** Monitoring boreholes with AE sensors shown with blue dots. **c** Calculated stress field around the test site together with the contours of the access drift (left-hand side) and the chamber (right-hand side). **d** Comparison of calculated stress field with fracture plane orientation as outlined by AE activity (black+). It can be seen that HF at borehole depths below 2 m yield to macroscopic fracture planes parallel to the gallery wall and perpendicular to the horizontal injection well, whereas the fractures in greater depths are oriented normal to the minimum principal stress [48]. The injection borehole is shown in red in all subfigures

central injection well (red line). During six fracturing and refracturing tests, 735 AE events could be precisely localized delineating planar structures with a residual error below 10 cm.

The orientations of the macroscopic fracture planes as indicated by the AE measurement were compared with independent stress calculations using Finite Element Method (FEM). These calculations were based on long-term surface subsidence measurement and measurement of underground convergence. Figure 22d shows the result of FEM in a vertical cross-section through the test site. The orientation of the fracture planes as measured by AE agrees remarkably well with the orientation of the calculated principal stresses. It can be seen that the direction of the fracture planes appears to coincide with the maximum principal stress (Fig. 22d). Whereas at borehole depths below 2 m the macroscopic fracture planes are parallel to the gallery wall and perpendicular to the horizontal injection well, the fractures in greater depths are striking in y-direction at approximately 63° normal to the minimum principal stress [48].

Manthei et al. [48] applied the absolute and relative moment tensor analysis on 263 well-located clustered events, which occurred during fracturing and refracturing tests in 1–9 m borehole depths. It was found that the events show similar radiation patterns with a major double-couple component, and that the orientations of the microscopic crack planes found by MT do not coincide with the macroscopic fracture planes indicated by source locations. Dahm et al. [47] assumed that shear failure occurred on horizontal, preexisting planes of weakness indicated by horizontal layers, which are observed within the salt rock at the test site.

Äspö Hard Rock Laboratory, Sweden. The main goal of the project was to test strategies of geothermal heat exchange in crystalline rocks using different hydraulic fracturing methods and minimize the occurrence of associated seismicity [39]. For this purpose, extensive network covering practically the full seismic frequency band was installed in Äspö hard rock laboratory, Sweden, at the depth of 410 m. The network consisted of broadband seismometers, short-period geophones deployed in tunnels and boreholes, high-frequency accelerometers and AE sensors (Fig. 23). The last two types of sensors were installed in the direct proximity (<15 m) from the stimulation borehole (Fig. 23b). The seismic systems, synchronized in time, covered elastic wave frequencies from 0.01 Hz up to the 100 kHz, however at variable, distance-dependent sensitivity. The seismic monitoring was completed with various types of electromagnetic measurements. Signal recorded by accelerometers and AE sensors were recorded concurrently using two acquisition systems working at 1 MHz sampling rate—one in triggering and a second in continuous mode recording. The triggering mode allowed for immediate assessment of seismicity response due to injection operation and provided therefore feedback to the ongoing process, and allowed e.g. the optimization of the localization procedure. The continuous mode allowed to record the full waveform field from all stimulations that could be used for a more detailed offline analysis of gathered data [40]. Ultrasonic transmission measurements were performed before the stimulation campaign to assess the P- and S-wave velocity.

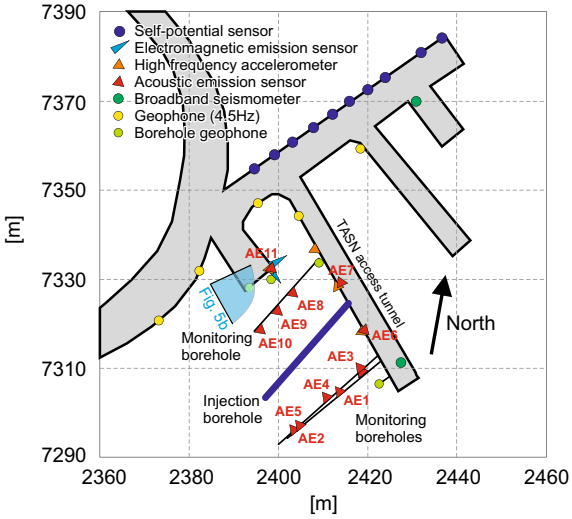

Fig. 23 Installation of seismic and electromagnetic monitoring networks in the proximity of the injection borehole (more sensors have been installed in surrounding tunnels, see detailed overview in Zang et al. [39]). The high-frequency accelerometers and AE sensors (orange and red triangles, respectively) are located in dedicated boreholes drilled close by the stimulated area. The bluish semi-transparent fan shows the camera location and viewing angle presented in Fig. 5b

Six hydraulic fracturing campaigns were performed in the stimulation borehole of 30 m length with up to 30 l of fresh water injected in each campaign. Four injections were performed at constant injection rate (HF1–2, HF4 and HF6 in Fig. 5b). The remaining two tested progressive (HF3) and pulse-type variants (HF5) stimulation types [183]. Each stimulation was composed of the fracking stage and up to 5 refracs. Stimulations were performed in different lithological units including granodiorite, diorite-gabbro and granite rocks, adding to the complexity while comparing different stimulation techniques with resulting seismic activity. For details on theoretical background with respect to different fracking scenarios, experimental setup and stimulation campaign and associated monitoring, we refer to Zang et al. [39, 183]. Here, we focus only on the seismic activity recorded and analyzed.

Over 69,000 triggers were recorded using AE sensors during monitoring, most of which were attributed to transient noise of anthropogenic, electrical or hydrological origin due to the very sensitive trigger conditions. The first catalog consisted of 196 confirmed AEs (see Fig. 23b for their spatial distribution) with relative location precision better then 1 dm recorded during stimulations HF1–HF4 and HF6 (no seismicity has been recorded during HF5). This dataset was extensively reprocessed and interpreted in Kwiatek et al. [41]. Much more AE events with supposedly smaller magnitudes were identified by Lopez-Comino et al. [40], who performed a detailed analysis using continuous AE recordings from HF2, where the largest amount of seismic events was observed. No usable waveforms of earthquakes have been recorded by other sensors including high-frequency accelerometers, geophones, short-period and broadband sensors. This became no surprise once the moment magnitudes were later estimated to be $M_W \leq -3.5$ [41].

Kwiatek et al. [41] investigated 196 earthquakes with $M_W \leq -3.5$ forming the original seismic catalog from all hydraulic stimulations performed during the project.

These events were first manually reprocessed to refine the accuracy of P- and S-wave picks and subsequent earthquake hypocentral locations.

The catalog was then relocated using the double-difference technique [148] resulting in relative precision of hypocenters not exceeding 0.1 m. HybridMT seismic moment tensor inversion and refinement package [184] was used to derive double-couple focal mechanisms of selected 17 high-quality events. Hammer hits performed along tunnel walls were used to cross-calibrate the AE sensors to actual ground motions observed on accelerometer sensors, resulting in estimated moment magnitudes ranging $-4.2 \leq M_W \leq -3.5$. Clear migration of seismicity upwards from injection intervals was observed over quasi-planar structures for injection intervals with sufficient number of earthquakes. Moreover, the spatial expansion was observed to slow down or even ceased after shut-in. For continuous stimulations with sufficient number of events it was observed that each subsequent refrac stage reached larger distance from the stimulation interval. The calculated focal mechanisms displayed heterogeneous orientation of fault surfaces in disagreement with the macroscopic orientation of the fracture propagation resolved from the hypocenter distribution. However, by comparing estimated fault planes with the local stress field Kwiatek et al. [41] identified that events on resolved fracture orientations are critically stressed (Fig. 24). The observed heterogeneity likely reflects structural heterogeneity of the rock mass and presence of faults at all scales [130].

Spatio-temporal and focal mechanism observations suggest progressive evolution of a fracture network in consecutive injection stages. The observed AE event

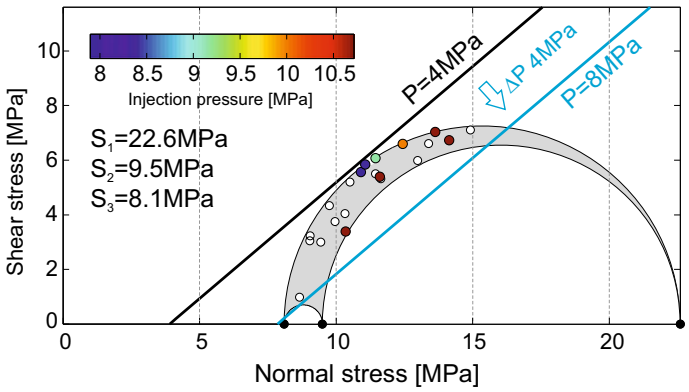

Fig. 24 Mohr circle representation of the state of stress in the vicinity of project. The thick black line denotes failure envelope assuming 4 MPa pore fluid pressure and friction coefficient 0.85. Colored dots represent projections of fault planes of 21 AE events on the Mohr circle for which focal mechanisms has been calculated [41]. One nodal plane projected on the Mohr circle that was closer to the failure envelope was used from each focal mechanism [187]. The circle color reflects the injection pressure at the time of AE event occurrence (with white color denoting no information available for injection pressure due to lack of hydraulic data in stimulation HF6). An increase of 4 MPa in pore pressure (blue failure envelope, cf. Fig. 25) can explain reactivation of all fractures for which fault plane solutions were calculated

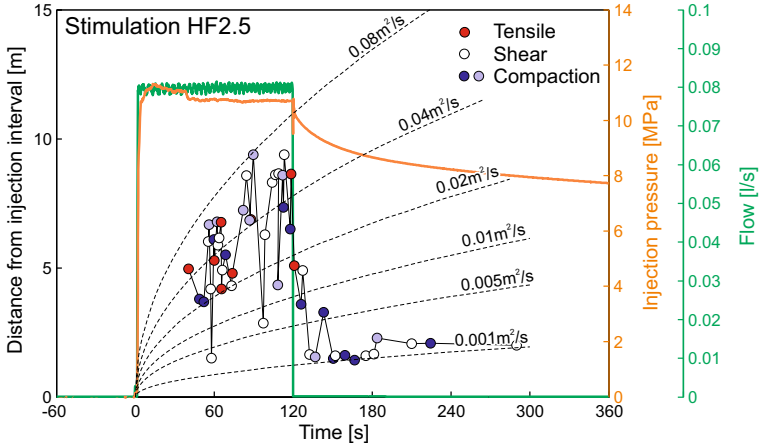

Fig. 25 Spatio-temporal evolution of seismic events with time since the beginning of continuous stimulation HF2 and distances from injection interval for the 5th refrac stage of stimulation HF2 (cf. blue spheres in Fig. 23). The AE events are color-coded with their mechanism calculated using polarity method [185] and show indications for some fracture opening during injection and fracture closure or shearing during shut-in phase. The dashed black curves represent modeled space–time evolution of a fluid pressure perturbation front triggering seismicity assuming to be controlled be only by scalar fluid pressure diffusion in a homogeneous isotropic medium [186]. The dashed curves are parameterized using different values of apparent hydraulic diffusivities. Modified after Kwiatek et al. [41]

migration signifies progressive reactivation of a fracture network with increasing hydraulic energy (rate) (Fig. 25). For successive stimulation stages, the AE activity occupies increasing rock volumes. The discrepancy between large seismically activated volume of rocks inferred from the seismic cloud (up to 8 m from the injection point) and small source radii of individual events suggests that during the injection stages a complex fracture network was activated rather than a single coherent fracture and presumably partial aseismic fracture opening.

The calculated source characteristics included radiated seismic energy providing insights into the energy budget of hydraulic fracturing and seismic hazard. It was found that the ratio of total radiated seismic energy to the hydraulic energy, the latter being the time integral of injection rate and average pressure, is ~10^{-5}. This is much lower than the seismic injection efficiency (the ratio of total radiated to total elastic strain energy available in the system), which is of order ~10^{-2}, and significantly higher than that typically observed for hydraulic fracturing [188]. Such discrepancy between tectonic and hydraulic-fracturing induced seismicity is explained by the fact that large amount of energy is spent in the creation of fracture network involving aseismic and slow seismic deformation processes.

López-Comino et al. [40] created and then interpreted an extended seismic catalog using continuous seismic recordings performed during stimulation. Using extensive waveform coherence analysis for automated full-waveform detection and location, they found for HF2 approximately 4,100 very small AE events, ~40 times more

than in the initial catalog. This increase in event detections allowed to discuss the spatio-temporal evolution of seismicity during HF2 in more details. The authors found the maximum magnitude increase within subsequent stimulation stage, with the smallest magnitude observed in the initial frac, and the largest magnitude visible during propagation of the fracture in the last, 5th stage. The maximum magnitude was found to correlate with the injected volume [178], however, as indicated in Kwiatek et al. [41] at very low level of seismic injection efficiency. The Gutenberg-Richter b-values were found to decrease from $b = 3.5$ to $b = 2.1$, with an average value of $b = 2.4$ when using the whole catalog of 4,100 events. The observed values were much higher than then observed in natural and induced earthquakes [2, 159, 189]. This could be interpreted as reactivation of fracture network with limited size distribution [41] or relatively low level of driving stresses stresses [111, 159].

Niemz et al. [42] extended continuos waveform analysis of López-Comino et al. [76] to all stimulations HF1-HF6, resulting in further expansion of seismic catalog to 19,600 located AEs. To exclude non-seismic signals that were polluting the continuous recordings, the Hidden Markov model classifier has been used (cf. [160]). This vast catalog allowed to investigate statistical (b-value) and spatio-temporal properties of seismicity associated with different hydraulic stimulation variants (continuous, progressive, and pulse-type). Niemz et al. [42] found the conventional (continuous) stimulations resulted in relatively simple and elongated fracture planes with stable orientations of fractures during refracturing stages. However, progressive injection scheme resulted in more complex pattern with variably oriented fracture planes. These outcomes were supported by b-value variations. These were found to be largery independent from hydraulic parameter (such as injection rate or injection pressure) unlike in other hydraulic fracturing experiments at larger scales. Instead, they could be correlated to different injection schemes with lower and higher b-values observed for continuos and progressive injection schemes, respectively.

Grimsel Test Site, Switzerland. The In-Situ Stimulation and Circulation (ISC) Experiment took place in the context of the Competence Center for Energy Research—Supply of Energy initiative in Switzerland that established a Swiss national roadmap for advancing deep geothermal energy production to achieve the goals specified in the Swiss Energy Strategy 2050, where the energy production of about 4.4 TWh per year are required from geothermal energy. The ISC project [176] was conducted between 2015 and 2018 in the crystalline rocks at the Grimsel Test Site, Switzerland located at 1,733 m above sea level and ~480 m below surface. In the first project phase the target rock volume on decameter scale was intensively characterized before the experiment, with a special focus on detailed stress analysis [84]. In a second project phase a series of 12 hydraulic stimulation experiments (both hydraulic fracturing (HF) and hydraulic shearing (HSH)). in a 20 m $\times$ 20 m $\times$ 20 m foliated, crystalline rock volume intersected by two distinct fault sets were performed [190].

Different to the Äspö project the same injection protocol was used for all experiments in the second experiment phase within each stimulation series in order to investigate the influence of local rock heterogeneities on the seismo-hydro-mechanical

response rather than differences due to the injection protocols. The ISC Experiment combined both during the characterization phase and during HS manifold measurements, including geophysical borehole logging [191], fracture mapping [190], seismic tomography, direct hydraulic and mechanical observations (fibre optic strain and pore pressure measurements [190]) and hydraulic testing (injections tests and cross-hole injections, with and without tracer [192, 193] to a diverse research program. In this summary we concentrate on the in-situ AE monitoring study of Gischig et al. [83], which used AE events to improve stress measurements and on the study of Villiger et al. [85], that demonstrated the spatio-temporal variability of the seismic response due to local geology.

Gischig et al. [83] summarized the intensive stress field characterization in the rock volume characterization phase at the ISC test side, which was based on hydraulic fracturing with a maximum injected volume of 11.3 l and overcoring. During stress field characterization 20 in-situ AE sensors (type GMuG MA-Bls-7-70) and four Wilcoxon accelerometers (type 736 T) were installed on the tunnel side wall and eight AE sensors (type GMuG MA-Blw-7-70) in a water-filled vertical borehole (Fig. 26). In total 1.161, 482 and 274 AE events were detected during HF1, HF2, and HF3, respectively. The difference in the number of detected events is most likely explained by the proximity of the sources to the borehole sensor array (9 m, 14 m, and 19 m respectively). The events outlined, similar to the Äspö experiment, clearly the fracture plane that extended up to 5 m from the injection point into the rock volume (see Fig. 26).

Events occurred mostly during the refracturing cycles once a critical injection volume of 0.5–1 L was exceeded and less during the initial fracturing cycle. A comparison of the fracture plane outlined by AE events (Fig. 27a) and the fracture visible on an imprint packer, showed the complexity of the fracture process. The imprint packer revealed that fractures initiated at the borehole wall within the foliation plane, but during fracture growth the fracture rotated, as outlined by AE events, in such way that it extends normal to the minimum principal stress. Interestingly the results of the overcoring deviated (Fig. 27). The deviation of the overcoring stress measurement result to the actual fracture plane observed could be explained by using a transversely isotropic elasticity model. The authors postulate that fracture nucleation occurred on flaws within the foliation plane, and extended within this weakness plane before rotating to lie normal to the minimum principal stress. The rotation occurred after at most several decimeters. They show that focal mechanisms come as a mixture of normal faulting and thrust faulting mechanisms, whereas a strike-slip mechanism, or possibly thrust, is expected from the stress field orientation, which they attribute to stress perturbation and pressure leak-off around the propagating fracture (Fig. 27b).

The authors point out that the findings of the study illustrate the challenges faced in stress characterization surveys in moderately anisotropic rock; a combination of overcoring, hydro-fracturing, and in-situ AE monitoring were essential at the Grimsel test site to arrive at a conclusive interpretation of all observations. One method alone would have lead to a possible wrong interpretation of the acting stress field. In-situ AE monitoring played the key role in identifying the true fracture plane orientation.

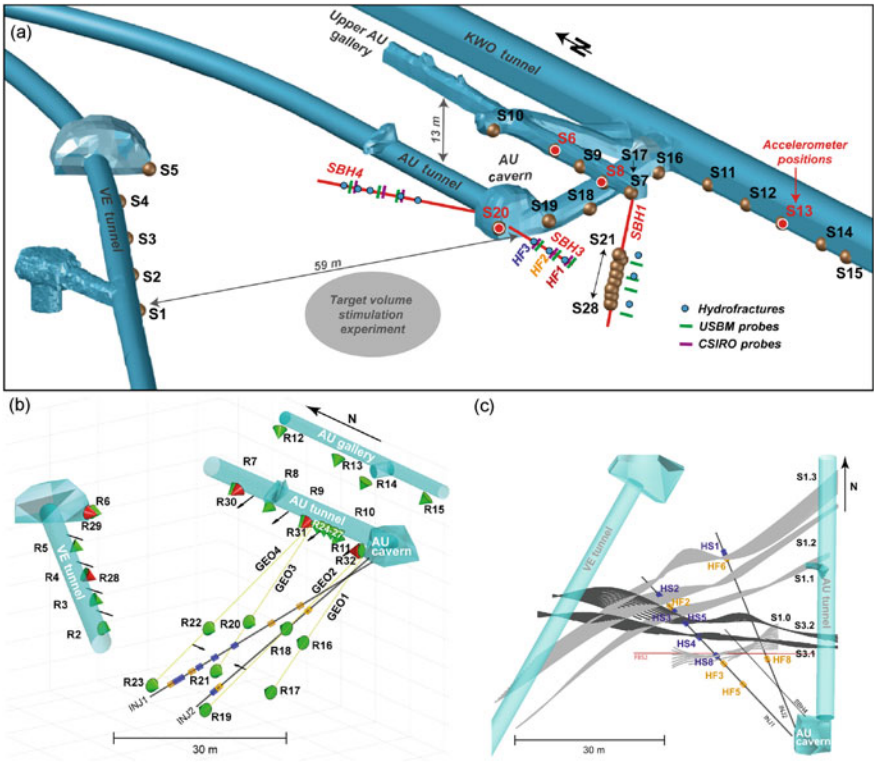

Fig. 26 In-situ AE monitoring networks at Grimsel ISC test side. During stress field characterization in project phase 1 the AE network shown in **a** with AE sensors shown by orange circles was in place (figure reproduced with permission from Gischig et al. [83]). During hydraulic stimulation experiments in project phase 2 the AE network shown in **b** with AE sensors shown as green cones was in place. The sites of injections intervals together with the dominant faults are shown in **c**. Figure **b**, **c** reproduced with permission from Villiger et al. [85]

In the second project phase a series of five hydraulic fracturing (HF2, HF3, HF5, HF6, HF8) and six hydraulic shearing experiments (HS1, HS2, HS3, HS4, HS5, HS8) were conducted with a maximum injected volume of one m^3. For monitoring a seismic network comprising of 8 in-situ AE sensors (type GMuG MA-Blw-7-70), was installed in monitoring boreholes in close vicinity (<10 m) to the two injection boreholes. In addition 18 AE sensors (type GMuG MA-Bls-7-70), five 1C accelerometers (Wilcoxon 736 T) and 115 100 Hz geophones were installed in short boreholes (<0.25 m) at the nearby access tunnels at distances from approximately 20–50 m from the injection points. The seismic monitoring network was accompanied by an extensive hydro-geomechanical monitoring system incorporating 60 FBG-sensors and a fibre optic Brillioun monitoring system to monitor the static and poro-elastic rock deformation, as well as pore-pressure. The experiment aimed at giving insights into the effect of different geological settings on the seismo-hydromechanical

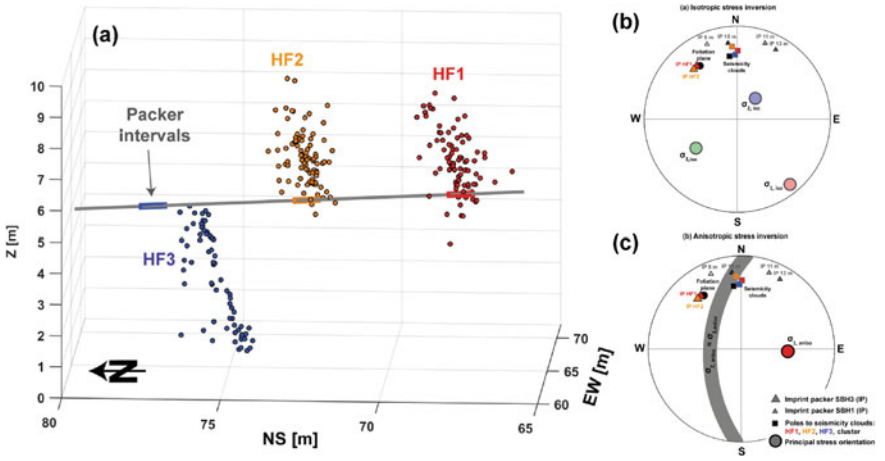

Fig. 27 Stress characterization at the Grimsel ISC test site. The AE activity (circles) outlining the fracture planes as recorded during hydraulic fracturing is shown in **a** [83]. The resulting stress orientations of the various stress determinations as well as the fault plane solution are shown assuming isotropic elastic parameters (**b**) and transversely isotropic elastic parameters (**c**) for the stress inversion from overcoring

response during HS. During hydraulic fracturing experiments, that took place in stimulation intervals in previously unfractured rock, a standardized injection protocol was applied with pressures overcoming the formation breakdown pressure. In hydroshearing experiments pre-existing shear zones were targeted, which allows to initiate HS at pressures below the minimum principl stress. For the latter the experimental volume was chosen in such a way that two types of shear zones could be targeted for the hydroshearing experiments: (i) ductile ones with intense foliation and (ii) brittle–ductile ones associated with a fractured zone. For all stimulations the stimulation interval was 1–2 m only.

The data was recorded with 200 kHz sampling frequency continuously throughout the experiments, i.e. approximately 6 h for each injection site. Overall more than 8,500 seismic events were detected during the 11 experiments, in each interval aligning mostly on a single plane (with some exceptions of clusters in small subparallel seismicity clouds) with magnitudes ranging from –6.2 to –2.5 (Fig. 28a, b). For both hydraulic fracturing and hydraulic shearing experiments the vast majority of events occurred during the pumping phases, 10% respectively 33% of events during shut-in, and <2% respectively 0% during venting. To the same time deformation measurements during the experiments show clearly that deformation occurs pre-dominantly aseismic, as seismic fracturing accounts for less than 2%. Due to standardized injection protocols a detailed comparison of the seismic response in between the different injections sites was possible.

Overall no systematical difference in AE activity was observed between hydrofracturing and hydroshearing experiments, likely because in all experiments the pre-existing fracture network played a key role. However, remarkable variability

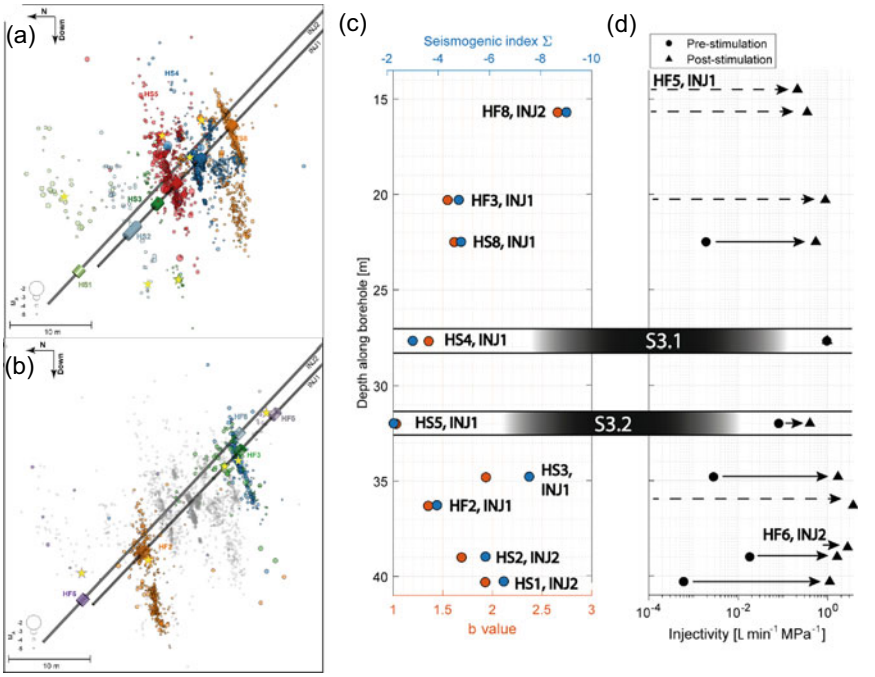

Fig. 28 AE activity as recorded during hydraulic stimulation experiments in Grimsel. The location of AE events recorded for the different stimulation intervalls is shown in sideview for hydraulic fracturing experiments (**a**) and hydraulic shearing experiments (**b**). The observed *b*-values and seismogenic index (**c**) as well as the increase in hydraulic injectivity (**d**) demonstrate the dependency on local geology, i.e. fault zone S3.1 and S3.2. Figure reproduced with permission from Villiger et al. [85]

in seismic response was observed between experiments. Despite of injection sites being located only meters apart, the seismic data corrected for detection limitations show significant variation both in seismic activity (seismogenic indices –9 to –2) and *b*-values (1–2.7) (see Fig. 28c). Injections targeting the highly conductive brittle-ductile shear zone came with comparable low *b*-values and high seismogenic index, whereas experiments in the vicinity of the more ductile shear zone exhibit more intense seismicity at the beginning of the experiment and lower overall seismic responses. A concentric growth of seismicity clouds was rarely observed, indicating that the spatial fracture zone heterogeneity had a substantial impact. Interestingly, despite of the significant differences in seismic response and initial injectivities dependent on the local geology, the final injectivities and transmissivities are very similar [193].

Reiche Zeche mine, Germany. The STIMTEC (STIMulation TEChnologies) experiment was conducted between 2018–2019 at depth of 130 m in the Reiche Zeche underground research laboratory (URL), Freiberg, Germany (Fig. 29). The hydraulic stimulations were designed to investigate the hydro-mechanical processes

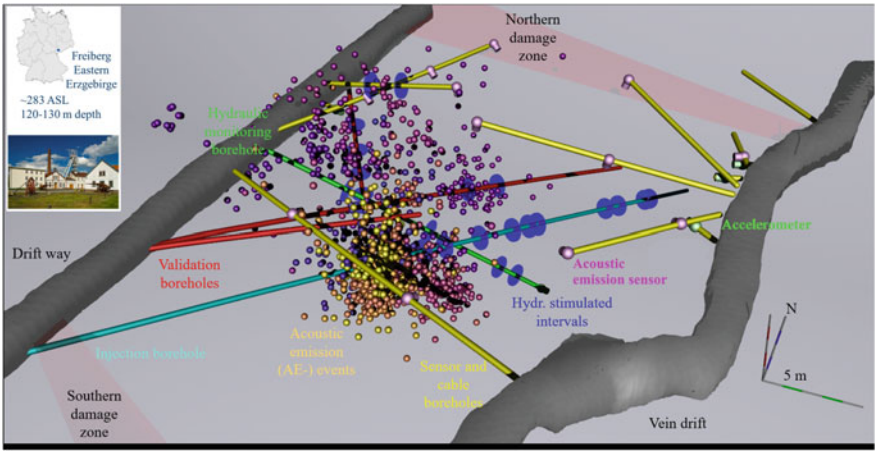

Fig. 29 Schematic 3D view of the borehole layout in STIMTEC project. Color coding for boreholes: light blue—injection borehole, yellow: boreholes with AE sensors, green: hydraulic monitoring borehole, red: mine-back validation boreholes. Damage zones (transparent red) were identified through mapping in the tunnels (grey), borehole logs, and retrieved cores. AE events during the frac and refrac stages of the three shallowest stimulation intervals (dark blue rings around injection borehole) are shown as coloured spheres. The majority of the 11,000 AE events observed for these intervals occurred during the periodic pumping after the frac-cycles. Inset shows location of the Reiche Zeche research mine in Freiberg, Germany

controlling enhancement of hydraulic properties in strongly anisotropic rock mass and their seismic response monitored with a combined network of AE sensors and accelerometers. The integrated analysis of seismic fingerprints and the alterations of the network of hydraulic conduits associated with hydraulic stimulations aims to provide diagnostic criteria for their success, as well as to provide guidelines for reduction of associated seismic hazard. The integrated approach comprises extensive injection operations including fracking-refracking-periodic pumping tests, real-time AE monitoring, active ultrasonic transmission measurements, validation (mine-back) drilling into stimulated volumes, laboratory experiments on samples, 3D-numerical stress modelling, and geomechanical simulations. In 2020 and 2021 new stimulation and AE monitoring campaings were performed within STIMTEC-X project.

The project targeted a volume of about 60 m × 30 m × 30 m of strongly foliated metamorphic gneiss. This volume was crosscut by multiple small-scale open and healed fractures and three major, steeply-dipping, northeast-southwest trending shear zones. The foliation was found to be sub-horizontal and causing significant elastic wave anisotropy (with P-wave velocity of 5,300 m/s perpendicular to 5,900 m/s parallel to foliation direction), as revealed by in-situ ultrasonic transmission measurements. This results were validated by laboratory experiments on rock samples. It was found that the implementation of an anisotropic velocity model significantly improved the quality of absolute locations of AE events.

The first stage of the project included 10 stimulation intervals along the 63 m long injection borehole (Fig. 29). Hydraulic injectivity/interference testing were performed before and after the stimulation, in particular exploiting the three mine-back validation boreholes. The validation stage also comprised further stress measurements and re-stimulation of four intervals. The total injected volume per interval was 15–25 l during the frac and refrac stages and up to 500 l during the subsequent step-rate tests and periodic-pumping (with periods of 60–800 s), amounting to about 10 m^3 of injected fluid volume in total. More than 11,000 high frequency AE events with source sizes on the cm-to-dm scale accompanied the stimulation at the three shallowest injection intervals and less than 10 AE events were observed for each of the three intermediate-depth stimulation intervals. Finally, no AE activity was recorded for the deepest stimulation intervals, where the rock mass was highly fractured. The follow up campaign performed within STIMTEC-X project used spatially re-arranged AE sensors network to improve the detection conditions for deep stimulation intervals. The results show that the observed dramatic differences in AE activity can not be simply explained by reduced capabilities of the network to detect very small events at the deeper intervals, but suggest that even at m-scale the seismic response of he rock mass to injection may be fundamentally different, with strongly varying partitioning of hydraulic strain energy into seismic and aseismic processes.

Whenever the seismicity was observed in the wake of fluid injection, its occurrence exhibited close correlation with pumping activity, in space and time. It was particularly noticeable that even slight periodic variations in injection pressure (or flow rate) led to according periodic variations in seismic activity, suggesting direct hydro-mechanical coupling can be responsible for stress redistribution leading to seismicity, in a similar extent as fluid-pressure diffusion.

In addition, the STIMTEC project attempts to establish a procedure for in-situ calibration of AE sensors to absolute ground motions. Ultrasonic transmission signals from stimulation borehole, and center-punch hits performed along tunnels surrounding the project site were used to assess the sensitivity of AE sensors at different seismic ray incidence angles [63, 194]. The center-punch device was used to calibrate AE sensors to actual ground motions by extending the methodology proposed by McLaskey et al. [87].

Bedretto Underground Laboratory for Geosciences, Switzerland. In 2019 the Bedretto Underground Laboratory for Geoenergies was opened by ETH Zurich, in order to bring stimulation experiments to the next level [89]. The 5 km long tunnel, build during the excavation of the Furka base tunnel, is located in the Bedretto Valley, Tessino/Switzerland in the Rotondo Granite and comes with 1,000 m plus overburden rock mass, for this reason providing a setting that is more similar to typical deep reservoirs than previous stimulation experiments. The tunnel has been retrofitted with a new access road, power supply, ventilation, IT-infrastructure and an external laboratory. In 2020 and 2021 the BULG will host a series of stimulation experiments with a maximum injection volume of 100 m^3 that are located in 400 m long boreholes. At the moment an extensive rock characterization phase is ongoing. A multi-sensor monitoring network, including a 92 channel in-situ AE monitoring system is installed within the reservoir. Different to all previous in-situ AE monitoring

systems the monitoring system designed in Bedretto incorporates a broad diversity of rock monitoring sensors installed within the same borehole as the AE sensors including geophones and accelerometers, fibre-optic bragg grating sensors, fibre optic single mode and multi-mode cables for temperature and strain measurements as well as pore pressure sensors.

Frac Sonde. In order to find the orientation of the minimum principal stress the fracture orientation has to be measured. Usually, for this purpose AE sensors are positioned in separate boreholes around the central borehole where the hydraulic fracturing takes place. A different approach was presented by Manthei et al. [50]. Here a borehole tool was developed which is able to do the same job utilizing only one borehole. The borehole tool was mainly applied in underground waste disposal research projects where knowledge about the stress state in rock was needed to characterize strength, tightness, and deformation behaviour of the host rock which has to isolate hazardous radioactive or chemical wastes from the biosphere for a long time. The borehole tool includes the hydraulic pressurization unit with the AE sensors. Due to the same distance between injection interval and sensor arrays the sensitivity of AE registration is always the same independent of the borehole depth. It is possible to trace back the realistic fracture propagation in distances up to 20 times of the borehole diameter. Other expensive inspection methods are not needed.

Figure 30 (right-hand side at top) schematically shows the borehole tool [50]. It consists of two parts—the hydraulic pressurization unit in the middle and two AE sensor arrays at both ends. It is applicable to borehole diameters between 98 and 104 mm. The overall length of the borehole tool is about 2 m. Each sensor array includes four AE sensors in a cross-section perpendicular to the borehole axis. The distance between the AE arrays is approximately 1.5 m. The AE sensors with integrated preamplifiers are placed in a common housing which is attached to the pressurization unit. The whole tool is pressed pneumatically against the borehole wall.

Figure 30 gives an overview on the hydraulic fracturing tests in the salt mine Bernburg performed in a 15 m long horizontal borehole at depths of 2, 4, 7, and 10.4 m. The location of the sensor arrays and the injection interval is indicated by means of circles and rectangles, respectively. The y-axis is parallel to the injection well. Approximately 15,000 located events are shown in a top view (left-hand side) and in a lateral view (right-hand side at bottom). 11,216 of these events could be localized during the fracturing test in 2 and 4 m borehole depths. In larger borehole depths 3,696 events were located in spite of the fact that the same oil volume was injected. This observation may be explained by larger deviatoric stresses close to the contour of a gallery. The extension of the fractures is nearly independent of borehole depth. In the fracturing test in 4 m borehole depth more than 5,100 AE events could be located outlining a plane fracture. The fracture initiated in the middle of the injection interval and propagated in radial direction transverse to the injection well. Most events are located at the crack tip. This is due to the fact that during fast crack propagation at the beginning of each fracture phase AE events are emitted so frequently that they overlap each other and, therefore, cannot be located, i.e. in this

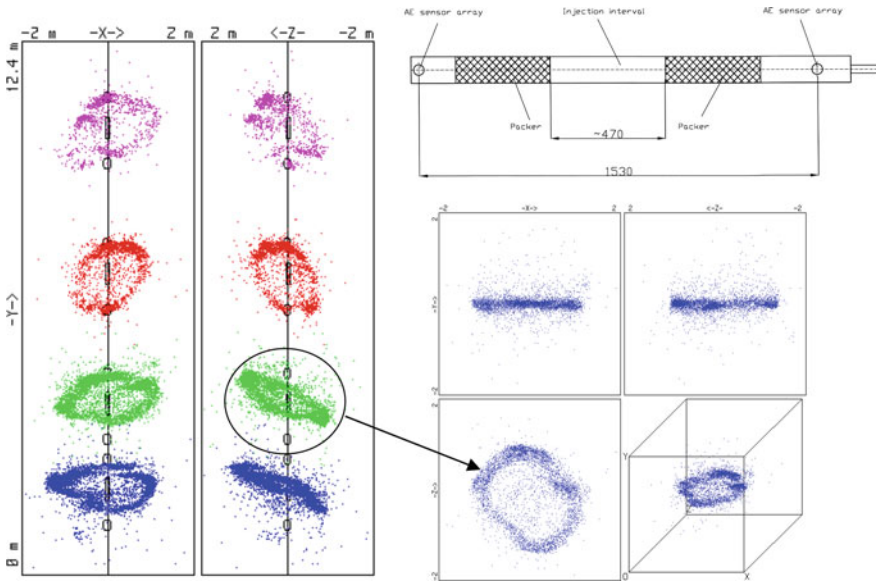

Fig. 30 Right-hand side at top: hydraulic fracturing tool (schematically; Manthei et al. [50]). Left-hand side: located AE events of a hydraulic fracturing series at the 500-m level of the salt mine Bernburg in projection to two coordinate planes. The location of the AE sensor arrays and the injection interval is indicated by means of circles and rectangles, respectively. The y axis is parallel to the injection well [50]. Right-hand side at bottom: Located AE events of a hydraulic fracturing test in 4 m borehole depth (black arrow) in projection to the rotated coordinate planes and perspective view [50]

experiment due to trigger mode recording the catalog is incomplete at frac initiation and a significant number of events is missed.

Generally, the borehole tool is applicable in all rocks which show spontaneous and fast crack formation. Difficulties will occur in layered or multiply jointed rocks, because such rock types show a high attenuation and strong absorption of the elastic waves. On the other hand, hydraulic fracturing measurements deliver valuable data like absolute magnitude and orientation of the minimum principal stress for the validation of structural models which are used to calculate the geomechanical evolution of the long-term stability of mines. Further promising applications relate to tunnel excavation in rock and to the construction of geotechnical barriers like dams.

3.4 In-situ Acoustic Emission Monitoring in Soft Rock

Recording high-frequency seismic waves in soft rock is challenging, because frequencies f > 1 kHz are damped strongly and AE events become non-detectable within meters from their hypocenters. Furthermore, argillaceous rocks are normally

elastically anisotropic, which introduces additional challenges in interpreting the signals. However, monitoring of soft rock is of interest for science and society, as e.g. clay formations are one of the three rock types suitable for the long-term storage of nuclear waste and are studied accordingly extensively. We present in this chapter the study from Le Gonidec et al. [75] studying the formation of the excavation damage zone during gallery drilling in the Clay formation of the Mont Terri Underground Laboratory, because this study demonstrates the potentials and spatial limitations of in-situ AE monitoring in soft rock.

Mont Terri Underground Rock Laboratory, Switzerland. The Mont Terri Underground Rock Laboratory is located in the Mesozoic shale formation (Opalinus Clays) of the Mont Terri asymmetric anticline in the Jura/Switzerland. Le Gonidec et al. [75] report on the results of In-situ AE monitoring within the EZ-G08 experiment that investigated the potential of non-destructive monitoring of the integrity of the rock barrier. The experiment exploits the excavation of the new Gallery Ga08 (horizontal axis 4 m, vertical axis 5 m) in Mont Terri that connects orthogonally to an already existing gallery Ga04, a situation that allows monitoring ahead of the excavation face. The project aims at characterization of the excavation damage zone (EDZ), in terms of extent, fracturing and hydro-mechanical properties, which ultimately is a necessary step in order to assess the self-sealing capacity of a waste disposal vault in a shale formation.

The experiment investigates three different geophysical survey techniques: active seismic surveying using an ultrasonic source (dominant frequency 33 kHz), in-situ AE monitoring and geoelectrics. For the active and passive seismic monitoring two independent monitoring systems are installed in nine (sub) horizontal boreholes drilled from the end-face of Gallery Ga04, as shown in Fig. 31. Passive recording of AE activity was realized by 4 AE sensors manufactured by Physical Acoustics (Type *R0.45UC*, bandwidth 2–60 kHz) placed in four monitoring boreholes at 3.5 to 6.5 m distance to the tunnel excavation. Proper coupling of the sensors was ensured by using an inflatable membrane to push the sensor to the naked borehole side wall. The authors point out that smoothing the borehole wall was important to achieve decent coupling. Data was recorded on a 16-channel monitoring system (500 kHz sampling frequency, 12 bit), recording 4 ms time windows.

The results of the active seismic survey gave in-depth information on the internal rock properties of the rock volume sampled: P-wave velocity ranged between 3,300 m/s along the bedding plane and 2,700 m/s at 70° incidence relative to the bedding. The S wave was measured along one single raypath only and equaled 1,560 m/s at 30° incidence relative to the bedding plane. The results indicate anisotropy correlated to the bedding structures that serve accordingly as a frequency filter.

In-situ AE monitoring recorded in addition to noise and work related transient events a total of 1,880 seismic events in the time period 10 to 12 July, when Gallery Ga08 approached from 11.2 m distance to 8.1 m distance to Gallery Ga04. Afterwards the excavation was stopped, but the seismic activity continued until 16 July (247 located seismic events). Due to the soft rock environment the recording of useful seismic signals was significantly limited. Seismic events were recorded from

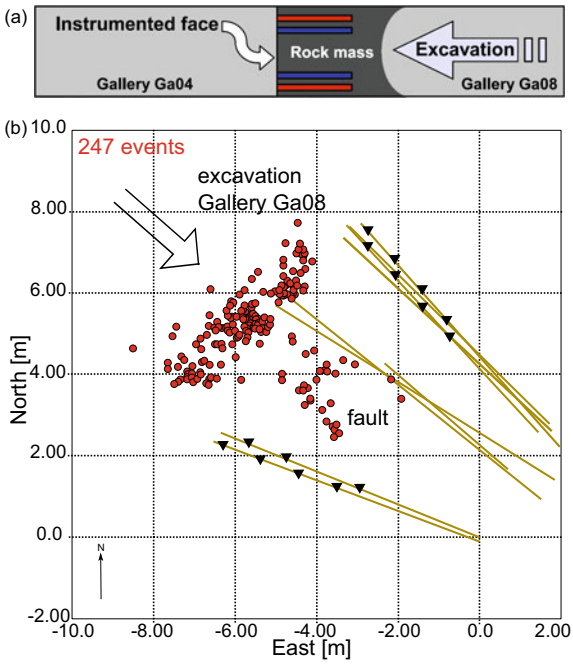

Fig. 31 AE activity observed in Opalinus Clay correlated to tunnel excavation. Seismic events are shown as red dots, far-field AE sensors as black triangles, boreholes as brown lines. The seismic activity of the time period 12 July 2008, 12 a.m. to 21 July 2008, 12 am after excavation stop is shown. The activity concentrates approximately 1.5 m from the excavation face and on a pre-existing fault. Note the short source-receiver distances necessary for the observation, owing to the significant damping in soft rock. Figure modified after Le Gonidec et al. [75]

a maximum distance of 6.5 m, but good signal-to-noise ratios were associated with travel distances of 0.3–1.5 m from source to receiver. During excavation the AE activity clustered near the excavation front outlining the rock disturbance introduced by the excavation and migrating with time according to the excavation progress. This demonstrates that passive AE monitoring can be used as a tool for monitoring the temporal and spatial evolution of the excavation damage zone. However, discrimination between noise events directly due to the excavation works and seismic events due to the shale formation damage remained difficult. The authors speculate that the activity corresponds first to crack initiation in tensile failure mode and involves than by growth and interaction of such micro-cracks towards macroscopic shear failure.

Picoseismic activity after excavation stop concentrated on the one hand side within 1.5 m from the excavation face and on the other hand on a major SE-dipping fault (located approximately 5 m away from Gallery 4 and 3 m away from the final excavation face), that was mapped after Gallery Ga08 was finalized. The author postulate that the fault was reactivated by the excavation process in accommodating the stress changes due to the excavation, an effect which appears to be more important than that of the EDZ formation.

4 Concluding Remarks

In conclusion, this chapter summarizes the capability of in-situ AE monitoring on the results of monitoring projects in mines worldwide. It is shown that the in-situ AE method is capable of detecting microcracking, in high resolution and low magnitude of completeness which is caused by very small deformation processes. The in-situ AE monitoring provides detailed insights into the ongoing deformation processes within the rock volume that is not accessible for geotechnical assessment methods. These measurements provides not only the information on structural health of the rock mass, but helps to understand the physics of rupture nucleation and propagation. The AE in-situ monitoring in mines provides valuable insights into earthquake physics, closing the observational gap between laboratoratory experiments and larger scales.

In contrast to in-situ AE monitoring, microseismic monitoring is used to measure large-scale deformations in mines, which may cause rock bursts or roof falls. Due to limitations in frequency range and sensitivity, microseismic networks are not able to detect microcracks. Compared to microseismic monitoring or active tomography surveys, in-situ AE monitoring is more sensitive; i.e. damage processes are detected in an early stage often before macroscopically visible damage occurs.

The presented case studies demonstrate that monitoring of larger rock volumes with in-situ AE measurements is possible in various rock types. Detections of AE events from distances greater than 100 m is possible in rock with low wave attenuation like salt rock or some hard rocks. In this case, rock volumes far away from the AE network can be monitored Thus in-situ AE monitoring is capable of detecting zones of instability in mines away from structures, which can be important input when designing exploration geometries or understanding damage long before macroscopic damage becomes visible.

Real-time processing gives direct information on the temporal-spatial evolution of AE events, outlining processes such as clustering, migration of AE activity or aftershock sequences of microseismic events. Recent advances in computer storage capacity and speed allow recording of continuous data streams with 1 MHz sampling in addition to trigger mode recording, which makes the application of advanced post-processing techniques possible.

Significant future advancements in AE technology in mines will likely take place through multidisciplinary research efforts that include areas such as structural dynamics, signal processing, sensor characterization and development, computer hardware, data telemetry and automated evaluation methods with pattern recognition, as well as other areas that have yet to be defined. The current topics in the field of self-learning systems which are definitely relevant for in-situ AE monitoring are currently not used enough.

References

1. Hardy HR (1981) Applications of acoustic emission techniques to rock and rock structures: a state-of-the-art review. Acoustic emissions in geotechnical engineering practice. Am Soc Test Mater 4–92
2. Bohnhoff M, Kwiatek G, Dresen G (2016) Von der Gesteinsprobe bis zur Plattengrenze: Skalenübergreifende Analyse von Bruchprozessen. Syst Erde 6:50–55. https://doi.org/10.2312/GFZ.syserde.06.01.8. (in German)
3. Plenkers K, Kwiatek G, Nakatani M, Dresen G, JAGUARS Research Group (2010) Observation of seismic events with frequencies f > 25 kHz at Mponeng Gold Mine, South Africa. Seism Res Lett 81:467–479. https://doi.org/10.1785/gssrl.81.3.467
4. Boettcher MS, McGarr A, Johnston MJS (2009) Extension of Gutenberg-Richter distribution to –1.3, no lower limit in sight. Geophys Res Lett 36:L10307. https://doi.org/10.1029/2009GL038080
5. Kwiatek G, Plenkers K, Nakatani M, Yabe Y, Dresen G, JAGUARS Research Group (2010) Frequency-magnitude characteristics down to magnitude –4.4 for induced seismicity recorded at Mponeng gold mine, South Africa. Bull Seismol Soc Am 100:1167–1173. https://doi.org/10.1785/0120090277
6. Naoi M, Nakatani M, Horiuchi S, Yabe Y, Philipp J, Kgarume T, Morema G, Khambule S, Masakale T, Ribeiro L et al (2013) Frequency-magnitude distribution of $-3.7 \leq M_W \leq 1$ mining-induced earthquakes around a mining front and b-value invariance with post-blast time. Pure Appl Geophys 171:2665–2684. https://doi.org/10.1007/s00024-013-0721-7
7. Boettcher MS, Kane DL, McGarr A, Johnston MJS, Reches Z (2015) Moment tensors and other source parameters of mining-induced earthquakes in TauTona Mine, South Africa. Bull Seismol Soc Am 105(3):1576–1593. https://doi.org/10.1785/0120140300
8. Reid HF (1910) The mechanism of the earthquake, in: The California Earthquake of April 18, 1906. Report of the State Earthquake Investigation Commission, Carnegie Institute of Washington, Washington, DC, vol 2, pp 16–28
9. Obara K (2002) Nonvolcanic deep tremor associated with subduction in southwest Japan. Science 296:1679–1681. https://doi.org/10.1126/science.1070378
10. Nadeau RM, Dolenc D (2005) Nonvolcanic tremors deep beneath the San Andreas fault. Science 307:389. https://doi.org/10.1126/science.1107142
11. Gomberg J, Rubinstein JL, Peng Z, Creager KC, Vidale JE, Bodin P (2008) Widespread triggering of nonvolcanic tremor in California. Science 319:17. https://doi.org/10.1126/science.1149164
12. Beroza GC, Ide S (2011) Slow earthquakes and nonvolcanic tremor. Annu Rev Earth Planet Sci 39:271–296. https://doi.org/10.1146/annurev-earth-040809-152531
13. Blanke A, Kwiatek G, Goebel THW, Bohnhoff M, Dresen G (2020) Stress drop—magnitude—dependence of acoustic emissions during laboratory stick-slip. Geophys J Int. https://doi.org/10.1093/gji/ggaa524
14. Cocco M, Tinti E, Antonella C (2016) On the scale dependence of earthquake stress drop. J Seismol 20(4):1151–1170. https://doi.org/10.1007/s10950-016-9594-4
15. Madariaga R (1976) Dynamics of an expanding circular fault. Bull Seismol Soc Am 66:639–666
16. Kwiatek G, Plenkers K, Martínez-Garzón P, Leonhardt M, Zang A, Dresen G (2017) New insights into fracture process through in-situ acoustic emission monitoring during fatigue hydraulic fracture experiment in Äspö Hard Rock Laboratory. Procedia Eng 191:618–622. https://doi.org/10.1016/j.proeng.2017.05.225
17. Manthei G, Plenkers K (2018) Review on in situ acoustic emission monitoring in the context of structural health monitoring in mines. Appl Sci 8:1595. https://doi.org/10.3390/app8091595
18. Feng X-F, Young RP, Reyes-Montes JM, Aydan Ö, Ishida T, Liu J-P-, Liu H-J (2019) ISRM suggested method for in situ acoustic emission monitoring of the fracturing process in rock masses. Rock Mech Rock Eng 52:1395–1414. https://doi.org/10.1007/s00603-019-01774-z

19. Cheon D-S, Jung Y-B, Park E-S, Song W-K, Jang H-I (2011) Evaluation of damage level for rock slopes using acoustic emission technique with waveguides. Eng Geol 121:75–88. https://doi.org/10.1016/j.enggeo.2011.04.015
20. Byun Y-S, Sagong M, Kim S-C, Chun B-S, Park S-Y, Jung H-S (2012) A study on using acoustic emission in rock slope with difficult ground—focused on rainfall. Geosci J 16:435–445. https://doi.org/10.1007/s12303-012-0035-2
21. Butcher R, Stacey TR, Joughin WC (2005) Mud rushes and methods of combating them. J S Afr Inst Min Metall 105(11):817–824
22. Weber S, Faillettaz J, Meyer M, Beutel J, Vieli A (2018) Acoustic and microseismic characterization in steep bedrock permafrost on Matterhorn (CH). J Geophys Res Earth Surf 123:1363–1385. https://doi.org/10.1029/2018JF004615
23. Sasaki S, Ishida T, Kanagawa T (1987) Source location and focal mechanisms of AE events during the hydraulic fracturing. In: CRIEPI Rep. U86032, Central Research Institute of Electric Power Industry, Abiko, Japan
24. Ohtsu M (1991) Simplified moment tensor analysis and unified decomposition of acoustic emission sources: application to in situ hydrofracturing test. J Geophys Res 96:6211–6221. https://doi.org/10.1029/90JB02689
25. Ishida T, Kanagawa T, Uchita Y (2014) Acoustic emission induced by progressive excavation of an underground powerhouse. Int J Rock Mech Min Sci 71:362–368. https://doi.org/10.1016/j.ijrmms.2014.08.001
26. Butt SD, Mukherjee C, Lebans G (2000) Evaluation of acoustic attenuation as an indicator of roof stability in advancing headings. Int J Rock Mech Min Sci 37:1123–1131
27. Cheng W, Wang W, Huang S, Ma P (2013) Acoustic emission monitoring of rockbursts during TBM-excavated headrace tunneling at Jinping II hydropower station. J Rock Mech Geotechn Eng 5:486–494. https://doi.org/10.1016/j.jrmge.2011.09.001
28. Falls SD, Young RP (1998) Acoustic emission and ultrasonic-velocity methods used to characterise the excavation disturbance associated with deep tunnels in hard rock. Tectonophysics 289:1–15. https://doi.org/10.1016/S0040-1951(97)00303-X
29. Young RP, Collins DS (1999) Monitoring an experimental tunnel seal in granite using acoustic emission and ultrasonic velocity. In: Amadei B, Kranz RL, Scott GA, Smeallie PH (eds) Rock mechanics for industry. Balkema, Leiden, The Netherlands, pp 869–876
30. Young RP, Hazzard JF, Pettitt WS (2000) Seismic and micromechanical studies of rock fracture. Geophys Res Lett 2000:1767–1770. https://doi.org/10.1029/2000GL011547
31. Collins DS, Young RP (2000) Lithological controls on seismicity in granitic rocks. Bull Seismol Soc Am 90:709–723
32. Young RP, Collins DS (2001) Seismic studies of rock fracture at the Underground Research Laboratory, Canada. Int J Rock Mech 38:787–799. https://doi.org/10.1016/S1365-1609(01)00043-0
33. Collins DS, Pettitt WS, Young RP (2002) High-resolution mechanics of a micro-earthquake sequence. Pure Appl Geophys 159:197–219
34. Young RP, Collins DS, Reyes-Montes JM, Baker C (2004) Quantification and interpretation of seismicity. Int J Rock Mech 41:1317–1327. https://doi.org/10.1016/j.ijrmms.2004.09.004
35. Goodfellow SD, Young RP (2014) A laboratory acoustic emission experiment under in situ conditions. Geophys Res Lett 41:3422–3430. https://doi.org/10.1002/2014GL059965
36. Reyes-Montes JM, Flynn W, Huang J (2014) ONKALO POSE experiment—phase 3: acoustic and ultrasonic monitoring: working report 2013-39. Posiva Oy, Finland
37. Pettitt WS, Baker C, Young RP (2002) Using acoustic emission and ultrasonic techniques for assessment of damage around critical engineering structures. In: Proceedings of 5th North American rock mechanics symposium, University of Toronto Press, Toronto, ON, Canada, pp 1161–1170
38. Andersson JC, Martin CD (2009) The Äspö pillar stability experiment: part I-experiment design. Int J Rock Mech Min Sci 46:865–878. https://doi.org/10.1016/j.ijrmms.2009.02.010

39. Zang A, Stephansson O, Stenberg L, Plenkers K, Specht S, Milkereit K, Schill E, Kwiatek G, Dresen G, Zimmermann G et al (2017) Hydraulic fracture monitoring in hard rock at 410 m depth with an advanced fluid-injection protocol and extensive sensor array. Geophys J Int 208:790–813. https://doi.org/10.1093/gji/ggw430
40. López-Comino JA, Heimann S, Cesca S, Milkereit C, Dahm T, Zang A (2017) Automated full waveform detection and location algorithm of acoustic emissions from hydraulic fracturing experiment. Proc Eng 191:697–702. https://doi.org/10.1016/j.proeng.2017.05.234
41. Kwiatek G, Martinez-Garzon P, Plenkers K, Leonhardt M, Zang A, Specht S, Dresen G, Bohnhoff M (2018) Insights into complex sub-decimeter fracturing processes occurring during a water-injection experiment at depth in Äspö Hard Rock Laboratory, Sweden. J Geophys Res Sol Earth https://doi.org/10.1029/2017JB014715
42. Niemz P, Cesca S, Heimann S, Grigoli F, von Specht S, Hammer C, Zang A, Dahm T (2020) Full-waveform-based characterization of acoustic emission activity in a mine-scale experiment: a comparison of conventional and advanced hydraulic fracturing schemes. Geophys J Int 222(1):189–206. https://doi.org/10.1093/gji/ggaa127
43. Ishida T, Fujito W, Yamashita H, Naoi M, Fuji H, Suzuki K, Matsui H (2019) crack expansion and fracturing mode of hydraulic refracturing from acoustic emission monitoring in a small-scale field experiment. Rock Mech Rock Eng 52:543–553. https://doi.org/10.1007/s00603-018-1697-5
44. Eisenblätter J, Manthei G, Meister D (1998) Monitoring of microcrack formation around galleries in salt rock. In: Hardy HR (ed) Proceedings of the sixth conference on acoustic emission/microseismic activity in geologic structures and materials, Pennsylvania State University, University Park, PA, USA, 9–11 June 1998. Trans Tech Publications: Clausthal-Zellerfeld, Germany, pp 227–243
45. Dahm T, Manthei G, Eisenblätter J (1998) Relative moment tensors of thermally induced microcracks in salt rock. Tectonophysics 289:61–74. https://doi.org/10.1016/S0040-1951(97)00307-7
46. Manthei G, Eisenblätter J, Salzer K (1998) Acoustic emission studies on thermally and mechanically induced cracking in salt rock. In: Hardy HR (ed) Proceedings of the sixth conference on acoustic emission/microseismic activity in geologic structures and materials, Pennsylvania State University, University Park, PA, USA, 9–11 June 1998. Trans Tech Publications, Clausthal-Zellerfeld, Germany, pp 245–265
47. Dahm T, Manthei G, Eisenblätter J (1999) Automated moment tensor inversion to estimate source mechanism of hydraulically induced micro-seismicity in salt rock. Tectonophysics 306:1–17. https://doi.org/10.1016/00401S-S951(99)00041-4
48. Manthei G, Eisenblätter J, Dahm T (2001) Moment tensor evaluation of acoustic emission sources in salt rock. Constr Build Mater 15:297–309
49. Manthei G, Eisenblätter J, Kamlot P, Heusermann S (1998) AE measurements during hydraulic fracturing tests in a salt mine using a special borehole probe. In: Progress in acoustic emission IX. Proceedings of international acoustic emission conference, Big Island, Hawaii, USA, pp II60–II69
50. Manthei G, Eisenblätter J, Kamlot P (2003) Stress measurements in salt mines using a special hydraulic fracturing borehole tool. In: Proceedings of the international symposium on geotechnical measurements and modelling, Karlsruhe, Germany, 23–26 Sept 2003, pp 355–360
51. Spies T, Hesser J, Eisenblätter J, Eilers G (2004) Monitoring of the rockmass in the final repository Morsleben: experiences with acoustic emission measurements and conclusions. In: Proceedings of the DisTec 2004, Berlin, Germany, 26–28 Apr 2004, pp 303–311
52. Manthei G, Eisenblätter J, Spies T (2007) Source mechanisms of acoustic emission events between huge underground cavities in rock salt. In: Proceedings of the advances in acoustic emission 2007—proceedings of 6th international conference on acoustic emission, Lake Tahoe, NV, USA, 28 Oct–2 Nov 2007, pp 288–293
53. Spies T, Eisenblätter J (2001) Acoustic emission investigation of microcrack generation at geological boundaries. Eng Geol 61:181–188. https://doi.org/10.1016/S0013-7952(01)00053-9

54. Manthei G, Eisenblätter J, Spies T, Eilers G (2001) Source parameters of acoustic emission events in salt rock. J Acoust Emiss 19:100–108
55. Spies T, Hesser J, Eisenblätter J, Eilers J (2005) Measurements of acoustic emission during backfilling of large excavations. In: Proceedings of the 6th international symposium on rockbursts and seismicity mines (RaSiM6), Perth, Australia, 9–11 Mar 2005, pp 379–384
56. Manthei G, Eisenblätter J, Spies T (2006) Determination of wave attenuation in rock salt in the frequency range 1–100 kHz using located acoustic emission events. J Acoust Emiss 24:179–186
57. Köhler D, Spies T, Dahm T (2009) Seismicity patterns and variation of the frequency-magnitude distribution of microcracks in salt. Geophys J Int 179:489–499. https://doi.org/10.1111/j.1365-246X.2009.04303.x
58. Becker D, Cailleau B, Dahm T, Shapiro S, Kaiser D (2010) Stress triggering and stress memory observed from acoustic emission records in a salt mine. Geophys J Int 182:933–948. https://doi.org/10.1111/j.1365-246X.2010.04642.x
59. Becker D, Cailleau B, Kaiser D, Dahm T (2014) Macroscopic failure processes at mines revealed by acoustic emission (AE) monitoring. Bull Seismol Soc Am 104:1785–1801. https://doi.org/10.1785/0120130286
60. Nakatani M, Yabe Y, Philipp J, Morema G, Stanchits S, Dresen G (2008) Acoustic emission measurements in a deep gold mine in South Africa: project overview and some typical waveforms. Seismol Res Lett 79:311
61. Yabe Y, Philipp J, Nakatani M, Morema G, Naoi M, Kawakata H, Igarashi T, Dresen G, Ogasawara H, JAGUARS Research Group (2009) Observation of numerous aftershocks of an M_W 1.9 earthquake with an AE network installed in a deep gold mine in South Africa. Earth Planets Space 61:e49–e52
62. Plenkers K, Schorlemmer D, Kwiatek G, JAGUARS Research Group (2011) On the probability of detecting picoseismicity. Bull Seismol Soc Am 101:2579–2591. https://doi.org/10.1785/0120110017
63. Kwiatek G, Plenkers K, Dresen G, JAGUARS Research Group (2011) Source parameters of picoseismicity recorded at Mponeng Deep Gold Mine, South Africa: implications for scaling relations. Bull Seismol Soc Am 101:2592–2608. https://doi.org/10.1785/0120110094
64. Naoi M, Nakatani M, Yabe Y, Kwiatek G, Igarashi T, Plenkers K (2011) Twenty thousand aftershocks of a very small (M 2) earthquake and their relation to the mainshock rupture and geological structures. Bull Seismol Soc Am 101:2399–2407. https://doi.org/10.1785/0120100346
65. Davidsen J, Kwiatek G (2013) Earthquake interevent time distribution for induced micro-, nano-, and picoseismicity. Phys Rev Lett 110. https://doi.org/10.1103/PhysRevLett.110.068501
66. Kwiatek G, Ben-Zion Y (2013) Assessment of P and S wave energy radiated from very small shear-tensile seismic events in a deep South African mine. J Geophys Res 118:3630–3641. https://doi.org/10.1002/jgrb.50274
67. Davidsen J, Kwiatek G, Dresen G (2012) No evidence of magnitude clustering in an aftershock sequence of nano- and picoseismicity. Phys Rev Lett 108. https://doi.org/10.1103/PhysRevLett.108.038501
68. Ziegler M, Reiter K, Heidbach O, Zang A, Kwiatek G, Stromeyer D, Dahm T, Dresen G, Hofmann G (2015) Mining-induced stress transfer and its relation to a M_W 1.9 seismic event in an ultra-deep South African Gold Mine. Pure Appl Geophys 172:2557–2570. https://doi.org/10.1007/s00024-015-1033-x
69. Yabe Y, Nakatani M, Naoi M, Philipp J, Janssen C, Watanabe T, Katsura T, Kawakata H, Dresen G, Ogasawara H (2015) Nucleation process of an M2 earthquake in a deep gold mine in South Africa inferred from on-fault foreshock activity. J Geophys Res Sol Earth 120:5574–5594. https://doi.org/10.1002/2014JB011680
70. Kozłowska M, Orlecka-Sikora B, Kwiatek G, Boettcher MS, Dresen G (2015) Nanoseismicity and picoseismicity rate changes from static stress triggering caused by a M_W 2.2 earthquake in Mponeng gold mine, South Africa. J Geophys Res Sol Earth 120:290–307. https://doi.org/10.1002/2014JB011410

71. Dörner D, Philipp J, Manthei G, Popp T (2012) Monitoring of AE activity around a large-diameter borehole in rock salt. In: Progress in acoustic emission XVI. Proceedings of the international acoustic emission conference, Okinawa, Japan, pp 187–192
72. Manthei G, Philipp J, Dörner D (2012) Acoustic emission monitoring around gas-pressure loaded boreholes in rock salt. In: Berest PB, Ghoreychi M, Hadj-Hassen F, Tijani M (eds) Mechanical behavior of salt VII. Taylor & Francis (Balkema), London, UK, pp 185–192. ISBN 9780415621229
73. Popp T, Minkley W, Wiedemann M, Salzer K, Dörner D (2015) Gas pressure effects on salt—the large scale in-situ test Merkers. In: Lance R, Mellegard K, Hansen F (eds) Mechanical behavior of salt VIII. Proceedings of the conference on mechanical behavior of salt, South Dakota School of Mines and Technology, Rapid City, USA, 26–28 May 2015, pp 127–136
74. Plenkers K, Philipp P, Dörner D, Minkley W, Popp T, Wiedemann M (2018) Observation of seismic and aseismic rock behavior during large-scale loading experiment. In: Proceedings of the mechanical behavior of salt IX, Hannover, Germany, 12–14 Sept 2018
75. Le Gonidec Y, Schubnel A, Wassermann J, Gibert D, Nussbaum C, Kergosien B, Sarout J, Maineult A, Guéguen Y (2012) Field-scale acoustic investigation of a damaged anisotropic shale during a gallery excavation. Int J Rock Mech Min 51:136–148. https://doi.org/10.1016/j.ijrmms.2012.01.018
76. Naoi M, Nakatani M, Otsuki K, Yabe Y, Kgarume T, Murakami O, Masakale T, Ribeiro L, Ward A, Moriya H et al (2015) Steady activity of microfractures on geological faults loaded by mining stress. Tectonophysics 100–114. https://doi.org/10.1016/j.tecto.2015.02.025
77. Naoi M, Nakatani M, Kgarume T, Khambule S, Masakale T, Ribeiro L, Philipp J, Horiuchi S, Otsuki K, Miyakawa K et al (2015) Quasi-static slip patch growth to 20 m on a geological fault inferred from acoustic emissions in a South African gold mine. J Geophys Res 120:1692–1707. https://doi.org/10.1002/2014JB011165
78. Naoi M, Nakatani M, Igarashi T, Otsuki K, Yabe Y, Kgarume T, Murakami O, Masakale T, Ribeiro L, Ward A et al (2015) Unexpectedly frequent occurrence of very small repeating earthquakes ($-5.1 \leq M_W \leq -3.6$) in a South African gold mine: implications for monitoring intraplate faults. J Geophys Res Sol Earth 120:8478–8493. https://doi.org/10.1002/2015JB012447
79. Moriya H, Naoi M, Nakatani M, van Aswegen G, Murakami O, Kgarume T, Ward AK, Durrheim RJ, Philipp J, Yabe Y et al (2015) Delineation of large localized damage structures forming ahead of an active mining front by using advanced acoustic emission mapping techniques. Int J Rock Mech Min 79:157–165. https://doi.org/10.1016/j.ijrmms.2015.08.018
80. Yamaguchi J, Naoi M, Nakatani M, Moriya H, Igarashi T, Murakami O, Yabe Y, Durrheim R, Ogasawara H (2018) Emergence and disappearance of very small repeating earthquakes on a geological fault in a gold mine in South Africa. Tectonophysics 747–748:318–326. https://doi.org/10.1016/j.tecto.2018.10.014
81. Philipp J, Plenkers K, Gärtner G, Teichmann L (2015) On the potential of In-Situ Acoustic Emission (AE) technology for the monitoring of dynamic processes in salt mines. In: Lance R, Mellegard K, Hansen F (eds) Mechanical behavior of salt VIII. Proceedings of the conference on mechanical behavior of salt, South Dakota School of Mines and Technology, Rapid City, SD, USA, 26–28 May 2015, pp 89–98. ISBN 9781138028401
82. Pisconti A, Plenkers K, Philipp J, Thomas C (2020) Mapping lithological boundaries in mines with array seismology and in situ acoustic emission monitoring. Geophys J Int 220:59–70. https://doi.org/10.1093/gji/ggz430
83. Gischig VS, Doetsch J, Maurer H, Krietsch H, Amann F, Evans KF, Nejati M, Jalali M, Valley B, Obermann AC et al (2018) On the link between stress field and small-scale hydraulic fracture growth in anisotropic rock derived from microseismicity. Solid Earth 9:39–61. https://doi.org/10.5194/se-9-39-2018
84. Jalali M, Gischig V, Doetsch J, Näf R, Krietsch H, Klepikova M, Amann F, Giardini D (2018) Transmissivity changes and microseismicity induced by small-scale hydraulic fracturing tests in crystalline rock. Geophys Res Lett 45:1–9. https://doi.org/10.1002/2017GL076781

85. Villiger L, Gischig VS, Doetsch J, Krietsch H, Dutler NO, Jalali M, Valley B, Selvadurai PA, Mignan A, Plenkers K, Giardini D, Amann F, Wiemer S (2020) Influence of reservoir geology on seismic response during decameter-scale hydraulic stimulations in crystalline rock. Solid Earth 11:627–655. https://doi.org/10.5194/se-11-627-2020
86. Villiger L, Gischig VS, Kwiatek G, Krietsch H, Doetsch J, Jalali M, Amann F, Giardini D, Wiemer S (2021) Meter-scale stress heterogeneities and stress redistribution drive complex fracture slip and fracture growth during a hydraulic stimulation experiment. Geophys J Int. https://doi.org/10.1093/gji/ggab057
87. McLaskey GC, Glaser SD (2012) *Acoustic* emission sensor calibration for absolute source measurements. J Nondestruct Eval 31:157–168. https://doi.org/10.1007/s10921-012-0131-2
88. Plenkers K (2011) On the characteristics of mining-induced seismicity with magnitudes –5 < M_w < –1. PhD thesis, University of Potsdam, Potsdam, Germany
89. Gischig V, Giardini D, Amann F, Hertrich M, Krietsch H, Loew S, Maurer H, Villiger L, Wiemer S, Bethmann F, Brixel B, Doetsch J, Doonechaly N, Driesner T, Dutler N, Evans KF, Jalali M, Jordan D, Kittilä A, Ma X, Meier P, Nejati M, Obermann A, Plenkers K, Saar MO, Shakas A, Valley B (2020) Hydraulic stimulation and fluid circulation experiments in underground laboratories: stepping up the scale towards engineered geothermal systems. Geomech Energy Environ (in press). https://doi.org/10.1016/j.gete.2019.100175
90. Butcher A, Stork AL, Verdon JP, Kendall JM, Plenkers K, Booth F, Boneham M, Koe A (2021) Evaluating rock mass disturbance within open-pit excavations using seismic methods: a case study from the Hinkley Point C nuclear power station. J Rock Mech Geotech Eng. https://doi.org/10.1016/j.jrmge.2020.12.001
91. Bormann P, Wendt S, DiGiacomo D (2013) Seismic sources and source parameters. In: Bormann P (ed) New manual of seismological observatory practice 2 (NMSOP2). Potsdam, Deutsches GeoForschungsZentrum GFZ, pp 1–259
92. Hanks TC, Kanamori H (1979) A moment magnitude scale. J Geophys Res 84:2348–2350
93. Eisenblätter J, Spies T (2000) Ein Magnitudenmaβ für Schallemissionsanalyse und Mikroakustik. In: Deutsche Gesellschaft für zerstörungsfreie Prüfung, 12. Kolloquium Schallemission, DGZfP Berichtsband: Jena, Germany, pp 29–41 (In German)
94. Gibowicz SJ, Kijko A (1994) An introduction to mining seismology. Academic Press, San Diego
95. Aki K, Richards PG (2009) Quantitative seismology. University Science Books, Sausalito
96. Cotton F, Archuleta R, Causse M (2013) What is sigma of the stress drop? Seismol Res Lett 84–42. https://doi.org/10.1785/0220120087
97. Candela T, Renard F, Bouchon M, Schmittbuhl J, Brodsky EE (2011) Stress drop during earthquakes: effect of fault roughness scaling. Bull Seismol Soc Am 101:2369–2387. https://doi.org/10.1785/0120100298
98. McLaskey GC, Glaser SD (2011) Micromechanics of asperity rupture during laboratory stick slip experiments. Geophys Res Lett 38:L12302. https://doi.org/10.1029/2011GL047507
99. Yoshimitsu N, Kawakata H, Takahashi N (2014) Magnitude –7 level earthquakes: a new lower limit of self-similarity in seismic scaling relationship. Geophys Res Lett 41:4495–4502. https://doi.org/10.1002/2014GL060306
100. Schmittbuhl J, Chambon G, Hansen A, Bouchon M (2006) Are stress distributions along faults the signature of asperity squeeze? Geophys Res Lett 33:L13307. https://doi.org/10.1029/2006GL025952
101. Tomic J, Abercrombie RE, doNascimento AF (2009) Source parameters and rupture velocity of small $M \leq 2.1$ reservoir induced earthquakes. Geophys J Int 179:1013–1023. https://doi.org/10.1111/j.1365-246X.2009.04233.x
102. Goebel THW, Kwiatek G, Becker T, Dresen G (2017) What allows seismic events to grow big?: insights from b-value and fault roughness analysis in laboratory stick-slip experiments. Geology 45(9):815–818. https://doi.org/10.1130/G39147.1
103. Abercrombie RE (2015) Investigating uncertainties in empirical Green's function analysis of earthquake source parameters. J Geophys Res Solid Earth 120:4263–4277. https://doi.org/10.1002/2015JB011984

104. Ide S, Beroza GC (2001) Does apparent stress vary with earthquake size? Geophys Res Lett 28:3349–3352. https://doi.org/10.1029/2001GL013106
105. Ide S, Beroza GC, Prejean SG, Ellsworth WL (2003) Apparent break in earthquake scaling due to path and site effects on deep borehole recordings. J Geophys Res 10(B5):2271. https://doi.org/10.1029/2001JB001617
106. McGarr A, Fletcher JB, Boettcher M, Beeler N, Boatwright J (2010) Laboratory-based maximum slip rates in earthquake rupture zones and radiated energy. Bull Seismol Soc Am 100(6):3250–3260. https://doi.org/10.1785/0120100043
107. Mayeda K, Gök R, Walter WR, Hofstetter A (2005) Evidence for non-constant energy/moment scaling from coda-derived source spectra. Geophys Res Lett 32:L10306. https://doi.org/10.1029/2005GL022405
108. Kanamori H, Brodsky E (2004) The physics of earthquakes. Rep Prog Phys 67:1429–1496. https://doi.org/10.1088/0034-4885/67/8/R03
109. Davidsen J, Stanchits S, Dresen G (2007) Scaling and universality in rock fracture. Phys Rev Lett 98:125502
110. Kwiatek G, Goebel THW, Dresen G (2014) Seismic moment tensor and *b* value variations over successive seismic cycles in laboratory stick-slip experiments. Geophys Res Lett 41:5838–5846. https://doi.org/10.1002/2014GL060159
111. Goebel THW, Sammis CG, Becker TW, Dresen G, Schorlemmer D (2015) A comparison of seismicity characteristics and fault structure between stick-slip experiments and nature. Pure Appl Geophys 172:2247–2264. https://doi.org/10.1007/s00024-013-0713-7
112. Deschanel S, Vanel L, Vigier G, Godin N, Ciliberto S (2006) Statistical properties of microcracking in polyurethane foams under tensile test, influence of temperature and density. Int J Fract 140:87–98
113. Åström J, Di Stefano PCF, Pröbst F, Stodolsky L, Timonen J, Bucci C, Cooper S, Cozzini C, Feilitzsch FV, Kraus H, Marchese J, Meier O, Nagel U, Ramachers Y, Seidel W, Sisti M, Uchaikin S, Zerle L (2006) Fracture processes observed with a cryogenic detector. Phys Lett A 356(4–5):262–266. https://doi.org/10.1016/j.physleta.2006.03.059
114. Milev AM, Spottiswoode SM (2002) Effect of the rock properties on mining induced seismicity around the Ventersdorp Contact Reef, Witwatersrand Basin, South Africa. Pure Appl Geophys 159:165–177
115. Gibowicz S (2009) Chapter 1—seismicity induced by mining: recent research. Adv Geophys 51:1–53. https://doi.org/10.1016/S0065-2687(09)05106-1
116. Julia J, Nyblade A, Durrheim R, Linzer L, Gök R, Dirks P, Walter W (2009) Source mechanisms of mine-related seismicity, Savuka Mine, South Africa. Bull Seismol Soc Am 99:2801–2814. https://doi.org/10.1785/0120080334
117. Bischoff M, Cete A, Fritschen R, Meier T (2010) Coal mining induced seismicity in the Ruhr Area, Germany. Pure Appl Geophys 167:63–75. https://doi.org/10.1007/s00024-009-0001-8
118. Wuestefeld A, Kendall JM, Verdon J, van As A (2011) In situ monitoring of rock fracturing using shear wave splitting analysis: an example from a mining setting. Geophys J Int 187:848–860. https://doi.org/10.1111/j.1365-246X.2011.05171.x
119. Kühn D, Vavrycuk V (2013) Determination of full moment tensors of microseismic events in a very heterogeneous mining environment. Tectonophysics 589:33–43. https://doi.org/10.1016/j.tecto.2012.12.035
120. Dresen G, Kwiatek G, Goebel THW, Ben-Zion Y (2020) Seismic and aseismic preparatory processes before large stick–slip failure. Pure Appl Geophys. https://doi.org/10.1007/s00024-020-02605-x
121. Baker C, Young RP (1997) Evidence for extensile crack initiation in point source time-dependent moment tensor solutions. Bull Seismol Soc Am 87:1442–1453
122. Carlson SR, Young RP (1993) Acoustic emission and ultrasonic velocity study of excavation-induced microcrack damage at the underground research laboratory. Int J Rock Mech Mining Sci Geomech Abstr 30:901–907. https://doi.org/10.1016/0148-9062(93)90042-C
123. Young RP, Martin CD (1993) Potential role of acoustic emission/microseismicity investigations in the site characterization and performance monitoring of nuclear waste repositories.

Int J Rock Mech Mining Sci Geomech Abstr 30:797–803. https://doi.org/10.1016/0148-9062(93)90025-9
124. Cai M, Kaiser PK, Martin CD (1998) A tensile model for the interpretation of microseismic events near underground openings. Pure Appl Geophys 153:67–92
125. Pettitt W (1997) The evaluation of a transducers azimuthal response using an aluminium half-cylinder, Keele University
126. Pettitt WS (1998) Acoustic emission source studies of microcracking in rock. PhD thesis, Keele University
127. Urbancic TI, Trifu C-I, Mercer RA, Feustel AJ, Alexander JAG (1996) Automatic time-domain calculation of source parameters for the analysis of induced seismicity. Bull Seismol Soc Am 86:1627–1633
128. Varnes DJ (1989) Predicting earthquakes by analyzing accelerating precursory seismic activity. Pure Appl Geophys 130:661–686
129. Das S, Scholz CH (1981) Theory of time-dependent rupture in the earth. J Geophys Res Solid Earth 86:6039–6051
130. Ben-Zion Y, Sammis CG (2003) Characterization of fault zones. Pure Appl Geophys 160:677–715
131. Naoi M, Nakatani M, Yabe Y, Philipp J, JAGUARS (2008) Very high frequency AE (up to 200 kHz) and microseismicity obser- vation in a deep South African gold mine-evaluation of the acoustic properties of the site by in-situ transmission test. Seismol Res Lett 79(2):330
132. Stanchits S, Dresen G, JAGUARS Research Group (2010), Formation of faults in diorite and quartzite samples extracted from a deep gold mine (South Africa). Geophys Res Abstr 12. EGU2010-5605
133. Dieterich JH (1994) A constitutive law for rate of earthquake production and its application to earthquake clustering. J Geophys Res Solid Earth 99:2601–2618
134. Dieterich JH (1979) Modeling of rock friction: experimental results and constitutive equations. J Geophys Res Solid Earth 84:2161–2168
135. Aki K (1987) Magnitude-frequency relation for small earthquakes: a clue to the origin of f_{max} of large earthquakes. J Geophys Res Solid Earth 92:1349–1355. https://doi.org/10.1029/JB092iB02p01349
136. Ogata Y (1999) Seismicity analysis through point-process modeling: a review. Pure Appl Geophys 155:471–507. https://doi.org/10.1007/978-3-0348-8677-2_14
137. Lippiello E, Godano C, de Arcangelis L (2007) Dynamical scaling in branching models for seismicity. Phys Rev Lett 98:098501. https://doi.org/10.1103/PhysRevLett.98.098501
138. Corral Á (2004) Long-term clustering, scaling, and universality in the temporal occurrence of earthquakes. Phys Rev Lett 92:108501
139. Corral Á (2009) Statistical tests for scaling in the inter-event times of earthquakes. Int J Mod Phys B 23:5570–5582
140. Jost ML, Busselberg T, Jost O, Harjes H-P (1998) Source parameters of injection-induced microearthquakes at the KTB deep drilling site, Germany. Bull Seismol Soc Am 88:815–832
141. Baisch S, Harjes H-P (2003) A model for fluid-injection-induced seismicity at the KTB, Germany. Bull Seismol Soc Am 152:160–170. https://doi.org/10.1046/j.1365-246X.2003.01837.x
142. Schorlemmer D, Woessner J (2008) Probability of detecting an earthquake. Bull Seismol Soc Am 98:2103–2117. https://doi.org/10.1785/0120070105
143. Kwiatek G, Martínez-Garzón P, Dresen G, Bohnhoff M, Sone H, Hartline C (2015) Effects of long-term fluid injection on induced seismicity parameters and maximum magnitude in northwestern part of The Geysers geothermal field. J Geophys Res Solid Earth 7085–7101. https://doi.org/10.1002/2015JB012362
144. McGarr A (1994) Some comparisons between mining-induced and laboratory earthquakes. Pure Appl Geophys 142:467–489
145. Richardson E, Jordan TH (2002) Seismicity in deep gold mines of South Africa: implications for tectonic earthquakes. Bull Seismol Soc Am 92:1766–1782

146. Yamada T, Mori JJ, Ide S, Abercrombie RE, Kawakata H, Nakatani M, Iio Y, Ogasawara H (2007) Stress drops and radiated seismic energies of microearthquakes in a South African gold mine. J Geophys Res 112:B03305. https://doi.org/10.1029/2006JB004553
147. Naoi M, Nakatani M, Horiuchi S et al (2014) Frequenc-magnitude distribution of $-3.7 \leq M_W \leq 1$ Mining-induced earthquakes around a mining front and *b* value invariance with post-blast time. Pure Appl Geophys 171:2665–2684. https://doi.org/10.1007/s00024-013-0721-7
148. Waldhauser F, Ellsworth WL (2000) A Double-Difference earthquake location algorithm: method and application to the Northern Hayward Fault, California. Bull Seismol Soc Am 90:1353–1368
149. van Aswegen G (2008) Ortlepp shears–dynamic brittle shears of South African gold mines. In: Potvin Y, Carter J, Dyskin A, Jeffrey R (eds) Proceedings of the first southern hemisphere international rock mechanics symposium, Australian Centre for Geomechanics, Perth, pp 111–119. https://doi.org/10.36487/ACG_repo/808_160
150. Adams GR, Jager AJ, Roering C (1981) Investigations of rock fractures around deep level gold mine stopes. In: Rock mechanics from research to application, 22nd U.S. symposium on rock mechanics (USRMS), 29 June–2 July, Cambridge, Massachusetts
151. Kato A, Obara K, Igarashi T, Tsuruoka H, Nakagawa S, Hirata N (2012) Propagation of slow slip leading up to the 2011 M_W 9.0 Tohoku-Oki Earthquake. Science 335:705–705. https://doi.org/10.1126/science.1215141
152. Ohnaka M (1993) critical size of the nucleation zone of earthquake rupture inferred from immediate foreshock activity. J Phys Earth 41:45–56. https://doi.org/10.4294/jpe1952.41.45
153. Nadeau RM, Johnson LR (1998) Seismological studies at Parkfield VI: moment release rates and estimates of source parameters for small repeating earthquakes. Bull Seismol Soc Am 88:790–814
154. McLaskey GC, Lockner DA (2014) Preslip and cascade processes initiating laboratory stick slip. J Geophys Res Solid Earth 119:6323–6336. https://doi.org/10.1002/2014JB011220
155. Igarashi T, Matsuzawa T, Hasegawa A (2003) Repeating earthquakes and interplate aseismic slip in the northeastern Japan subduction zone. J Geophys Res Solid Earth 108(B5):2249. https://doi.org/10.1029/2002JB001920
156. Igarashi T (2010) Spatial changes of inter-plate coupling inferred from sequences of small repeating earthquakes in Japan. Geophys Res Lett 37:L20304. https://doi.org/10.1029/2010GL044609
157. Uchida N, Matsuzawa T, Ellsworth WL, Imanishi K, Shimamura K, Hasegawa A (2012) Source parameters of microearthquakes on an interplate asperity off Kamaishi NE Japan over two earthquake cycles. Geophys J Int 189:999–1014. https://doi.org/10.1111/j.1365-246X.2012.05377.x
158. Scholz CH (1968) The frequency-magnitude relation of microfracturing in rock and its relation to earthquakes. Bull Seismol Soc Am 58:399–415
159. Schorlemmer D, Wiemer S, Wyss M (2005) Variations in earthquake-size distribution across different stress regimes. Nature 437:437–539. https://doi.org/10.1038/nature04094
160. Hammer C, Beyreuther M, Ohrnberger M (2012) A seismic-event spotting system for volcano fast-response systems. Bull Seism Soc Am 102(3):948–960. https://doi.org/10.1785/0120110167
161. Kaiser D, Spies T, Schmitz H (2013) Mikroakustisches monitoring in bergwerken zur Bewertung aktueller Rissprozesse. In: Sörgel U, Schack L (eds) Proceedings of the geomonitoring 2013, Hannover, Germany, 14–15 March 2013, pp 39–55 (In German)
162. Gundelach V, Furche M, Schuster K, Kaiser D, Schennen S, Beilecke T (2020) Beispiele untertägiger Erkundung durch Geophysik im Ton, Kristallin und Salz, Mitteilungen der Deutschen Geophysikalischen Gesellschaft, Sonderband I/2020, pp 37–54 (in German)
163. Maghsoudi S, Hainzl S, Cesca S, Dahm T, Kaiser D (2014) Identification and characterization of growing large-scale en-echelon fractures in a salt mine. Geophys J Int 196(2):1092–1105. https://doi.org/10.1093/gji/ggt443
164. Kamlot P, Günther R-M, Stockmann N, Gärtner G (2012) Modeling of strain softening and dilatancy in the mining system of the southern flank of the Asse II mine. In: Berest PB,

Ghoreychi M, Hadj-Hassen F, Tijani M (eds) Mechanical behavior of salt VII. Taylor & Francis (Balkema), London, UK, pp 327–336
165. Kamlot P, Weise D, Gärtner G, Teichmann L (2012) Drift sealing in the Asse II mine as a component of the emergency concept–Assessment of the hydro-mechanical functionality. In: Berest PB, Ghoreychi M, Hadj-Hassen F, Tijani M (eds) Mechanical behavior of salt VII. Taylor & Francis (Balkema), London, UK, pp 479–489
166. Stacey TR, Wesseloo J (1998) In situ stresses in mining areas in South Africa. J S Afr Inst Min Metall 365–368
167. Haimson BC, Cornet FH (2003) ISRM suggested methods for rock stress estimation–part 3: hydraulic fracturing (HF) and/or hydraulic testing of pre-existing fractures (HTPF). Int J Rock Mech Min 40:1011–1020. https://doi.org/10.1016/j.ijrmms.2003.08.002
168. Kaiser PK, Valley B, Dusseault MB, Duff D (2013) Hydraulic fracturing mine back trials–design rationale and project status. In: Proceedings ISRM international conference for effective and sustainable hydraulic fracturing. International Society for Rock Mechanics, IntechOpen Limited, London. https://doi.org/10.5772/56260
169. Warpinski NR, Mayerhofer M, Agarwal K, Du J (1992) Hydraulic-fracture geomechanics and microseismic-source mechanisms. SPE J 18:766–780
170. Economides MJ, Nolte KG, Ahmed U, Schlumberger D (2000) Reservoir stimulation. Wiley, Chichester, UK
171. Häring MO, Schanz U, Ladner F, Dyer BC (2008) Characterisation of the Basel 1 enhanced geothermal system. Geothermics 37:469–495
172. Schindler M, Nami P, Schellschmidt R, Teza D, Tischner T (2008) Summary of hydraulic stimulation operations in the 5 km deep crystalline HDR/EGS reservoir at Soultz-sous-Forêts. In: Proceedings of the 33rd workshop on geothermal reservoir engineering, Stanford, CA, USA, 28–30 Jan 2008, pp 325–333
173. Jeffrey RG (2000) Hydraulic fracturing of ore bodies. US Patent No. 6,123,394
174. Niitsuma H, Nagano K, Hisamatsu K (1993) Analysis of acoustic emission from hydraulically induced tensile fracture of rock. J Acoust Emiss 11:S1–S18
175. Guglielmi Y, Cappa F, Avouac JP, Henry P, Elsworth D (2015) Seismicity triggered by fluid injection-induced aseismic slip. Science 348:1224–1226
176. Amann F, Gischig V, Evans K, Doetsch J, Jalali R, Valley B, Krietsch H, Dutler N, Villiger L, Brixel B, Klepikova M, Kittilä A, Madonna C, Wiemer S, Saar MO, Loew S, Driesner T, Maurer H, Giardini D (2018) The seismo-hydro-mechanical behaviour during deep geothermal reservoir stimulations: Open questions tackled in a decameterscale in-situ stimulation experiment. Solid Earth 9:115–137. https://doi.org/10.5194/se-2017-79
177. Evans KF, Zappone A, Kraft T, Deichmann N, Moia F (2012) A survey of the induced seismic responses to fluid injection in geothermal and CO2 reservoirs in Europe. Geothermics 41:30–54. https://doi.org/10.1016/j.geothermics.2011.08.002
178. McGarr A (2014) Maximum magnitude earthquakes induced by fluid injection. J Geophys Res Sol Ea. 119:1008–1019. https://doi.org/10.1002/2013jb010597
179. Atkinson GM, Eaton DW, Ghofrani H, Walker D, Cheadle B, Schultz R, Shcherbakov R, Tiampo K, Gu J, Harrington RM (2016) Hydraulic fracturing and seismicity in the Western Canada Sedimentary Basin. Seismol Res Lett 87:631–647. https://doi.org/10.1785/0220150263
180. Obermann A, Kraft T, Larose E, Wiemer S (2015) Potential of ambient seismic noise techniques to monitor the St. Gallen geothermal site (Switzerland). J Geophys Res Sol Earth 120:4301–4316. https://doi.org/10.1002/2014JB011817
181. Grigoli F, Cesca S, Rinaldi A, Manconi A, López-Comino J, Clinton J, Westaway R, Cauzzi C, Dahm T, Wiemer S (2017) M_w 5.5 Pohang earthquake (2018), a possible case of induced seismicity in South Korea. Science 360:1003–1006. https://doi.org/10.1126/science.aat2010
182. Kwiatek G, Saarno T, Ader T, Bluemle F, Bohnhoff M, Chendorain M, Dresen G, Heikkinen P, Kukkonen I, Leary P (2019) Controlling fluid-induced seismicity during a 6.1-km-deep geothermal stimulation in Finland. Sci Adv 5:eaav7224. https://doi.org/10.1126/sciadv.aav7224

183. Zang A, Yoon JS, Stephansson O, Heidbach O (2013) Fatigue hydraulic fracturing by cyclic reservoir treatment enhances permeability and reduces induced seismicity. Geophys J Int 195(2):1282–1287. https://doi.org/10.1093/gji/ggt301
184. Kwiatek G, Martínez-Garzón P, Bohnhoff M (2016) HybridMT: a MATLAB/shell environment package for seismic moment tensor inversion and refinement. Seismol Res Lett 87:964–976. https://doi.org/10.1785/0220150251
185. Zang A, Wagner FC, Stanchits S, Dresen G, Andresen R, Haidekker MA (1998) Source analysis of acoustic emission in Aue granite cores under symmetric and asymmetric compressive loads. Geophys J Int 135:1113–1130
186. Shapiro SA, Rothert E, Rath V, Rindschwentner J (2002) Characterization of fluid transport properties of reservoirs using induced microseismicity. Geophysics 67:212–220. https://doi.org/10.1190/1.1451597
187. Vavryčuk V (2014) Iterative joint inversion for stress and fault orientations from focal mechanisms. Geophys J Int 199(1):69–77. https://doi.org/10.1093/gji/ggu224
188. Maxwell SC, Waltmann C, Warpinski NR, Mayerhofer MJ, Boroumand N (2009) imaging seismic deformation induced by hydraulic fracture complexity. Reservoir Eval Eng 12:1. https://doi.org/10.2118/102801-PA
189. Bentz S, Kwiatek G, Durand V, Wollin C, Bohnhoff M, Martínez-Garzón P (2020) Earthquake catalog derived from template matching related to "A two-scale preparation phase preceded a 5.8 earthquake in the Sea of Marmara offshore Istanbul, Turkey". https://doi.org/10.5880/GFZ.4.2.2020.006.
190. Krietsch H, Doetsch J, Dutler N, Jalali M, Gischig V, Loew S, Amann F (2018) Comprehensive geological dataset describing a crystalline rock mass for hydraulic stimulation experiments. Sci Data 5:1–12. https://doi.org/10.1038/sdata.2018.269
191. Dutler N, Valley B, Gischig V, Villiger L, Krietsch H, Doetsch J, Brixel B, Jalali M, Amann F (2019) Hydraulic fracture propagation in a heterogeneous stress field in a crystalline rock mass. Solid Earth 10:1877–1904. https://doi.org/10.5194/se-10-1877-2019
192. Kittilä A, Jalali MR, Evans KF, Willmann M, Saar MO, Kong X-Z (2019) Field comparison of DNA-labeled nanoparticl and solute tracer transport in a fractured crystalline rock. Water Resour Res 55:6577–6595. https://doi.org/10.1029/2019WR025021
193. Brixel B, Klepikova M, Jalali MR, Lei Q, Roques C, Kriestch H, Loew S (2020) Tracking fluid flow in shallow crustal fault zones: 1. Insights from single-hole permeability estimates. J Geophys Res Sol Earth 125:4. https://doi.org/10.1029/2019JB018200
194. Manthei G (2005) Characterization of acoustic emission sources in a rock salt specimen under triaxial compression. Bull Seismol Soc Am 95(5):1674–1700. https://doi.org/10.1785/0120040076